



# LUND UNIVERSITY

## Unravelling the structure and dynamics of lipid nanoparticles for biomolecule delivery

Gilbert, Jennifer

2023

[Link to publication](#)

*Citation for published version (APA):*

Gilbert, J. (2023). *Unravelling the structure and dynamics of lipid nanoparticles for biomolecule delivery*. Lund University.

*Total number of authors:*

1

### General rights

Unless other specific re-use rights are stated the following general rights apply:

Copyright and moral rights for the publications made accessible in the public portal are retained by the authors and/or other copyright owners and it is a condition of accessing publications that users recognise and abide by the legal requirements associated with these rights.

- Users may download and print one copy of any publication from the public portal for the purpose of private study or research.
- You may not further distribute the material or use it for any profit-making activity or commercial gain
- You may freely distribute the URL identifying the publication in the public portal

Read more about Creative commons licenses: <https://creativecommons.org/licenses/>

### Take down policy

If you believe that this document breaches copyright please contact us providing details, and we will remove access to the work immediately and investigate your claim.

LUND UNIVERSITY

PO Box 117  
221 00 Lund  
+46 46-222 00 00

# Unravelling the structure and dynamics of lipid nanoparticles for biomolecule delivery

JENNIFER GILBERT

FACULTY OF SCIENCE | DEPARTMENT OF CHEMISTRY | LUND UNIVERSITY





# Unravelling the structure and dynamics of lipid nanoparticles for biomolecule delivery





# Unravelling the structure and dynamics of lipid nanoparticles for biomolecule delivery

by Jennifer Gilbert



**LUND**  
UNIVERSITY

DOCTORAL DISSERTATION

by due permission of the Faculty of Science, Lund University, Sweden.  
To be defended on Friday, the 27th of October 2023 at 13:00 in Lecture hall A at the  
Department of Chemistry, Lund University.

*Faculty opponent*

Prof. Jayne Lawrence  
University of Manchester, Manchester, UK

Organization <b>LUND UNIVERSITY</b> Department of Chemistry Box 124 SE-221 00 LUND Sweden		Document name <b>DOCTORAL DISSERTATION</b>	
		Date of disputation <b>2023-10-27</b>	
Author(s) <b>Jennifer Gilbert</b>		Sponsoring organization NanoLund, Swedish Research Council (2017-06716)	
Title and subtitle <b>Unravelling the structure and dynamics of lipid nanoparticles for biomolecule delivery</b>			
Abstract <p>Encapsulation in self-assembled lipid structures has been shown to increase the stability of large biomolecules, including proteins and nucleic acids (NAs), which has many potential applications in the food and pharmaceutical industries. In order to fully optimise the encapsulation system for a certain application, however, it is important to understand the effect of the encapsulated biomolecule on the lipid structure and vice versa.</p> <p>In the first part of my thesis, the encapsulation of different proteins in a lipid sponge phase (L<sub>3</sub>) system composed of food grade lipids was studied. Comparison between the effect on the L<sub>3</sub> phase of encapsulated beta-galactosidase (238 kDa), aspartic protease (34 kDa), myoglobin (17.6 kDa) and phytoalbumin BvPgb 1.2 (38.4 kDa) demonstrated the importance of specific lipid-protein interactions on the L<sub>3</sub> structure both in bulk and dispersions, as well as the stability of the encapsulated proteins. Systematic variation of the buffer and pH used to prepare and disperse the bulk L<sub>3</sub> phase highlighted pH and specific buffer effects on the L<sub>3</sub> structure.</p> <p>In the second part of my thesis, the structure of lipid nanoparticles (LNPs) for NA delivery was investigated using scattering methods and cryogenic transmission electron microscopy (cryoTEM). mRNA adsorption with pH and proportion of the cationic ionisable lipid (CIL) DLin-MC3-DMA was first studied in a model system for two model mRNAs and human erythropoietin mRNA. Effect of nucleic acid type and concentration was characterised in LNPs formulated with a benchmark LNP composition and four different NAs (polyadenylic acid, polyuridylic acid, double stranded and single stranded DNA). Using a combination of small angle x-ray and neutron scattering (SAX/NS), dynamic light scattering (DLS) and cryoTEM, the colloidal stability, LNP morphology, lipid composition of the LNP core-shell structure and structure of the core were determined.</p>			
Key words lipid nanoparticles, neutron scattering, SAXS, protein encapsulation, nucleic acid delivery, lipid self-assembly			
Classification system and/or index terms (if any)			
Supplementary bibliographical information		Language English	
ISSN and key title		ISBN 978-91-7422-986-8 (print) 978-91-7422-987-5 (pdf)	
Recipient's notes		Number of pages 357	Price
		Security classification	

I, the undersigned, being the copyright owner of the abstract of the above-mentioned dissertation, hereby grant to all reference sources the permission to publish and disseminate the abstract of the above-mentioned dissertation.

Signature

Date 2023-09-11

# Unravelling the structure and dynamics of lipid nanoparticles for biomolecule delivery

by Jennifer Gilbert



**LUND**  
UNIVERSITY

This doctoral thesis is constructed as a summary of research papers and consists of two parts. An introductory text puts the research work into context and summarises the main conclusions of the papers. Then, the research publications themselves are reproduced. The research papers may either have been already published or are manuscripts at various stages.

**Cover photo front:** A LEGO scientist with her sponge (not so) nanoparticles.

© Jennifer Gilbert 2023

Division of Physical Chemistry,  
Department of Chemistry,  
Lund University

ISBN: 978-91-7422-986-8 (print)

ISBN: 978-91-7422-987-5 (pdf)

Printed in Sweden by Media-Tryck, Lund University, Lund 2023



Media-Tryck is a Nordic Swan Ecolabel  
certified provider of printed material.  
Read more about our environmental  
work at [www.mediatryck.lu.se](http://www.mediatryck.lu.se)

**MADE IN SWEDEN** 



*To my mother*





# Table of Contents

Acknowledgments . . . . .	iv
Popular Science Summary . . . . .	vi
List of Publications . . . . .	viii
Author Contributions . . . . .	xi
Abbreviations . . . . .	xii
<b>1 Introduction</b>	<b>1</b>
1.1 What is a lipid and why do we care? . . . . .	2
1.2 What is a protein and why do we care? . . . . .	12
1.3 What is a nucleic acid and why do we care? . . . . .	16
<b>2 Methods</b>	<b>21</b>
2.1 Bulk scattering techniques . . . . .	22
2.2 Surface techniques . . . . .	29
2.3 Cryogenic transmission electron microscopy (cryoTEM) . . . . .	33
2.4 Ultraviolet-Visible spectroscopy (UV-Vis) . . . . .	34
2.5 Fluorescence . . . . .	34
<b>3 Results</b>	<b>35</b>
3.1 System 1: Sponge phase ( $L_3$ ) for protein encapsulation . . . . .	36
3.2 System 2: Lipid nanoparticles for nucleic acid delivery . . . . .	50
<b>4 Conclusions</b>	<b>71</b>
<b>Scientific Publications</b>	<b>83</b>

## Acknowledgments

*Tommy.* Thank you for your unwavering support and belief in me as my main supervisor throughout these 4 years. I have been able to travel the world, be involved in so many interesting projects and meet many amazing and inspiring people. You have taught me a lot; most importantly that no problem is unsolvable and the most important part of any beamtime experimental plan is dinner.

*Ann.* Thank you for how you have taken me under your wing and listened to my fears, frustrations and research problems with a sympathetic ear. You have been such a wonderful role model to me and I can only aspire to be as calm as you in the face of 2 am beamtime chaos.

*Justas and Jan.* Thank you *Justas* for the interesting conversations and industrial perspective and *Jan* for providing an insight into the world of simulations.

*Coauthors and collaborators.* This thesis would never have been possible without the work of so many other people and their expertise. *Marianna*, thank you for introducing me to the 'joys' of lipid nanoparticles and to *Maria* for teaching me everything I know about sponge phase. *Federica*, thank you for sharing your knowledge and the critical discussions of scattering data. *Simon*, thank you for the opportunity to work with such interesting proteins and *Inna*, for the molecular level insight into my samples.

*Instrument scientists.* During my PhD, I've had the opportunity to join several neutron and x-ray beamtimes. I am incredibly grateful to all of the instrument scientists who took part in these experiments and for all your help before, during and after the experiments. Thank you *Susana*, *Michi* and *Giovanna* for your patience in explaining everything and for answering calls at ridiculous times whenever something happened. An extra thank you to *Max*, *Jit* and *Najet* for performing remote experiments during the pandemic and all of the time and energy that took.

*Maria L., Maria S., Chris and Peter.* Without you keeping everything running in the background, I'm sure Fkem would fall apart! Thank you for your help with all of the practical and administrative problems I encountered.

*Nylander group (past and present).* Thank you to *Maria*, *Polina*, *Johan* and *Karolina* for welcoming me to Lund during my Masters project and then again when I started my PhD. *Ben*, thank you for always letting me

bother you with NR and ellipsometry questions even though you had no time for either. *Sebastian*, thanks for your encouraging feedback about NR data fitting, it was always so constructive.

*The Office™*. Thank you for all the support, chaos and nonsense - we always kept things interesting...

*My friends and colleagues at Physical Chemistry*. Thank you to everyone at Fkem for the fikas, lunches and afterworks that made this a wonderful place to work! A special thanks to the KC running crew - I never would have even thought about long distance running but here we are somehow... Thank you *Erika* for the great company on our unexpectedly eventful trip to Bombannes, *Justin*, *Iria* and *Dora* for our hiking adventures and dinners, *Dora* and *Marta* for our dancing escapades, *Sophie* for putting up with my never ending questions about NR data fitting, *Niamh* for keeping me sane (especially towards the end), *Marija* and *Noemi* for your amazing hugs, *Lucrezia* for letting me test the wording of sentences for papers on you at least five times a day and *Davide* for your random culture lessons. *Marco*, thank you for being the best nonna ever, for your science, life and Italian lessons and for the constant supply of lasagne.

*Friends and family*. *Becca*, *Tom* and *Tufa*, I am so glad we ended up in the same group in Swedish lessons - such a small world! *Sorina* and *Lucie*, it has been so fun to explore Lund and the rest of Sweden with you! And finally, thank you to my family. Thank you to Mum and Dad for always believing in me and supporting me in whatever I chose to do and to Cath for always getting it. I've always been bad with words, but I hope you know how much you all mean to me.



## Popular Science Summary

One of the first things you are taught in chemistry at school is that water and oil don't mix. Some molecules, however, have parts that like water (hydrophilic) and parts that like oil (hydrophobic or 'water hating'), such as the lipids which make up cell membranes in your body. These lipids are called amphiphilic lipids and are composed of a hydrophilic head group and a hydrophobic hydrocarbon tail.

When you mix amphiphilic lipids with water, they form a structure that hides the hydrophobic part away, so that only the hydrophilic part is in contact with the water. These lipids can form a wide variety of structures, from simple spheres to a 2D sheet (bilayer) and complicated 3D channel networks, depending on the lipid shape and its environment (e.g. temperature and pH). By changing the lipid (or lipid mixture) used, we can tune the structures formed and their properties for different applications. One common application in both the food and pharmaceutical industries for these lipid structures is the encapsulation of biomolecules, such as proteins and nucleic acids (like DNA and RNA). As these biomolecules can be quite sensitive, encapsulation can help to keep them more stable.

In this thesis, we have looked at two different lipid systems. The first lipid system was used to encapsulate proteins intended for use in the food industry, so all of the lipids were similar to those found in olive oil and were safe to be eaten. These lipids assemble into a structure called 'sponge phase', which (as you can probably guess) looks similar to a sponge with the structure of a disordered water channel network and the 'sponge' part made up by the lipid membrane. We looked at the effect of encapsulating four proteins with different sizes, structures, and functions on the structure of the sponge phase and how encapsulation affected the protein function. Two of these proteins were enzymes, which are responsible for speeding up biological reactions.  $\beta$ -galactosidase is used to make lactose free dairy products, and aspartic protease is used in cheese ripening. The other two are oxygen binding proteins with iron bound to a haeme group. Phyto-globin, a plant haemoglobin, from sugar beet has been proposed as an alternative iron supplement to treat anaemia, and myoglobin was used as a model protein for comparison, as it has a similar structure. We saw very different effects on the sponge phase structure; with some proteins interacting strongly with the lipids and others only weakly, and some stabilising the sponge phase structure and others destroying it.

The second lipid system we looked at was very similar to those used in the Pfizer/BioNTech and Moderna COVID-19 vaccines. This is made up of a complicated mixture of different lipids, but the main component was an ionisable lipid which changes its charge from positive to neutral with increasing pH. When mixed in the right conditions these lipids form lipid nanoparticles (particles with a size on the nanometre scale), which can be used for nucleic acid delivery to cells. We used two types of model messenger RNA, which contains the instructions the cell uses to make proteins, and two types of DNA, single stranded and double stranded (which is the one you've probably seen before). We looked at how these different nucleic acids affected the structure and stability of the lipid nanoparticles. As these lipid nanoparticles are now being tested to target a range of different diseases, therefore to encapsulate a range of different nucleic acids, understanding changes in structure and how it relates to their function is key for their successful application.

In summary, it's always more complicated than you think!

# List of Publications

This thesis is based on the following publications, referred to by their Roman numerals:

- I **Immobilisation of beta-galactosidase within a lipid sponge phase: structure, stability and kinetics characterisation**  
**J. Gilbert**, M. Valldeperas, S. K. Dhayal, J. Barauskas, C. Dicko, and T. Nylander  
*Nanoscale*, vol. 11, no. 44, pp. 21291–21301, 2019
- II **Effect of encapsulated protein on the dynamics of lipid sponge phase: a neutron spin echo and molecular dynamics simulation study**  
**J. Gilbert**, I. Ermilova, M. Nagao, J. Swenson, and T. Nylander  
*Nanoscale*, vol. 14, no. 18, pp. 6990–7002, 2022
- III **Encapsulation of sugar beet phytooglobin BvPgb 1.2 and myoglobin in a lipid sponge phase system**  
**J. Gilbert**, S. Christensen, T. Nylander, and L. Bülow  
*Frontiers in Soft Matter*, vol. 3, 2023
- IV **On the interactions between RNA and titrateable lipid layers: Implications for RNA delivery with lipid nanoparticles**  
**J. Gilbert**, I. Ermilova, M. Fornasier, M. Skoda, G. Fragneto, J. Swenson and T. Nylander  
*In review*
- V **Evolution of the structure of lipid nanoparticles for nucleic acid delivery: From *in situ* studies of formulation to colloidal stability**  
**J. Gilbert**, F. Sebastiani, M. Yanez-Arteta, A. Terry, A. Fornell, N. Mahmoudi and T. Nylander  
*Manuscript*
- VI **Effect of DNA base pairing and loading on the structure and internal ordering of lipid nanoparticles for nucleic acid delivery**  
**J. Gilbert**, M. Yanez-Arteta, F. Sebastiani, S. Teixeira, J. Mata, T. Cleveland, R. Lai and T. Nylander  
*Manuscript*

All papers are reproduced with permission from their respective copyright holders.

Publications not included in this thesis:

- **Cation and buffer specific effects on the DNA-lipid interaction**  
M. Mura, B. Humphreys, **J. Gilbert**, A. Salis, and T. Nylander  
Colloids and Surfaces B: Biointerfaces, vol. 223, article 113187, 2023
- **Structural Insights on Ionizable Dlin-MC3-DMA Lipids in DOPC Layers by Combining Accurate Atomistic Force Fields, Molecular Dynamics Simulations and Neutron Reflectivity**  
M. Ibrahim, **J. Gilbert**, M. Heinz, T. Nylander, and N. Schwier  
Nanoscale, vol. 15, no. 27, pp.11647-11656, 2023.



## Author Contributions

**Paper I: Immobilisation of beta-galactosidase within a lipid sponge phase: structure, stability and kinetics characterisation**

J.G. prepared the samples, performed the SAXS, DLS, CD and activity measurements, interpreted the data and was the main author of the manuscript.

**Paper II: Effect of encapsulated protein on the dynamics of lipid sponge phase: a neutron spin echo and molecular dynamics simulation study**

J. G. prepared the samples and led the NSE measurements, analysed and interpreted the NSE data and was the main author of the manuscript.

**Paper III: Encapsulation of sugar beet phytoalbumin BvPgb 1.2 and myoglobin in a lipid sponge phase system**

J.G. prepared the samples, performed the SAXS and DLS measurements, interpreted the data and co-wrote the manuscript.

**Paper IV: On the interactions between RNA and titrateable lipid layers: Implications for RNA delivery with lipid nanoparticles**

J.G. prepared the samples, designed both and led one of the NR experiments, performed the QCM-D experiments, analysed and interpreted all of the experimental data and co-wrote the manuscript.

**Paper V: Evolution of the structure of lipid nanoparticles for nucleic acid delivery: From *in situ* studies of formulation to colloidal stability**

J.G. prepared the samples, designed and led the *in situ* SAXS experiments, performed the SAXS and DLS experiments, designed the SANS experiment, analysed and interpreted all of the data and wrote the manuscript.

**Paper VI: Effect of DNA base pairing and loading on the structure and internal ordering of lipid nanoparticles for nucleic acid delivery**

J.G. conducted the NIST SANS beamtime with the instrument scientist, co-designed the ANSTO SANS experiment, performed the SAXS measurements, analysed and interpreted all of the data and wrote the manuscript.

## Abbreviations

<b>Asp</b>	aspartic protease
<b>β-gal</b>	β-galactosidase
<b>BvPgb 1.2</b>	phytoglobin from sugar beet ( <i>Beta vulgaris</i> ssp. <i>vulgaris</i> )
<b>CD</b>	circular dichroism
<b>Chol</b>	cholesterol
<b>CMSi</b>	contrast match silicon
<b>cryoTEM</b>	cryogenic transmission electron microscopy
<b>DGMO</b>	diglycerol monooleate
<b>DLS</b>	dynamic light scattering
<b>DMPE-PEG2000</b>	1,2-dimyristoyl-snglycero-3-phosphoethanolamine-N-[methoxy(polyethylene glycol)-2000]
<b>dsDNA</b>	double stranded DNA
<b>D<sub>2</sub>O</b>	deuterated water/heavy water
<b>DOPC</b>	1,2-dioleoyl-sn-glycero-3-phosphocholine
<b>DSPC</b>	1,2-distearoyl-sn-glycero-3-phosphocholine
<b>GMO-50</b>	Capmul GMO-50. Commercial product which is a mixture composed of mono-, di- and triglycerides, with glycerol monooleate as the main component.
<b>H<sub>2</sub></b>	inverse hexagonal phase
<b>H<sub>2</sub>O</b>	Protonated water/light water
<b>L<sub>α</sub></b>	Lamellar phase
<b>L<sub>2</sub></b>	Inverse micellar phase
<b>L<sub>3</sub></b>	Sponge phase
<b>L<sub>3</sub>NPs</b>	Sponge phase nanoparticles
<b>LLC</b>	Lipid liquid crystalline

<b>Mb</b>	myoglobin
<b>MC3</b>	DLin-MC3-DMA or (6Z,9Z,28Z,31Z)-heptatriacont-6,9,28,31-tetraene-19-yl 4-(dimethylamino)butanoate
<b>NA</b>	nucleic acid
<b>NPs</b>	nanoparticles
<b>NR</b>	neutron reflectometry
<b>NSE</b>	neutron spin echo spectroscopy
<b>ONPG</b>	o-nitrophenyl- $\beta$ -D-galactopyranoside
<b>POPC</b>	1-palmitoyl-2-oleoyl-sn-glycero-3-phosphocholine
<b>P80</b>	polysorbate 80
<b>PC</b>	phosphatidylcholine
<b>PEG</b>	polyethylene glycol
<b>polyA</b>	polyadenylic acid
<b>polyU</b>	polyuridylic acid
<b>P(q)</b>	form factor
<b>Q<sub>2</sub></b>	inverse bicontinuous cubic phase
<b>Q<sub>224</sub></b>	inverse bicontinuous cubic phase with Pn3m space group
<b>Q<sub>230</sub></b>	inverse bicontinuous cubic phase with Ia3d space group
<b>QCM-D</b>	quartz crystal microbalance with dissipation
<b>SANS</b>	small-angle neutron scattering
<b>SAXS</b>	small-angle X-ray scattering
<b>SLD</b>	scattering length density
<b>ssDNA</b>	single stranded DNA
<b>S(q)</b>	Structure factor
<b>UV</b>	ultra violet



1

# Introduction



The purpose of this chapter is to introduce the systems studied. In this thesis, I studied the interactions between three of the four biological building blocks of life: lipids, proteins and nucleic acids (the fourth is carbohydrates if anyone was wondering).

## 1.1 What is a lipid and why do we care?

Lipids, the main player we will discuss in this work, can be defined as "any of a class of organic compounds that are fatty acids or their derivatives and are insoluble or have low solubility in water."<sup>1</sup>, which is a general definition. Lipids play a vital role in most biological processes, including making up the cell membrane of living organisms.

### 1.1.1 Structure and self-assembly

In this thesis, we will consider specifically polar lipids, which are made up of a hydrophilic head group and a hydrophobic hydrocarbon chain (Figure 1.1a). Due to their amphiphilic nature, these lipids will self-assemble in an aqueous environment into different structures in order to minimise the contact between the non-polar part of the lipid and the solvent.

A rich variety of structures can form depending on the balance between the forces of the system: the hydrophobic effect, driving the self-assembly, and the hydrophilic, ionic or steric repulsion of the head groups, opposing the close contact between the lipid molecules. The packing or geometry of these structures can be generally described in terms of the packing parameter, or their interfacial curvatures, respectively<sup>2,3</sup>.

A simple approach to describing the effective shape of the lipid molecule is the critical packing parameter, also known as the surfactant number  $N_s$ , which considers the ratio between the volumes of the polar and non-polar parts of the molecule:

$$N_s = \frac{v}{a_0 l_c} \quad (1.1)$$

where  $v$  is the volume of the hydrocarbon chain(s),  $a_0$  is the effective head group area and  $l_c$  is the critical hydrocarbon chain length. For  $N_s > 1$  (Figure 1.1b), 'inverse' structures are formed, where the head group-tail interface curves towards the head groups; for  $N_s \approx 1$  (Figure 1.1c), more planar structures are formed, such as extended bilayers; and for  $N_s < 1$

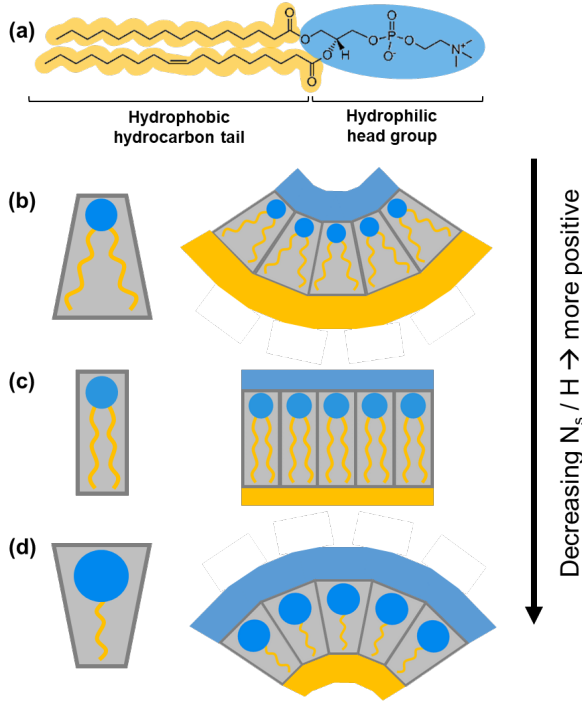


**Figure 1.1** (a) Example of how the hydrophilic head group and hydrophobic hydrocarbon tail are defined in a polar lipid using POPC as a model. A simplified representation for a lipid with (b)  $N_s > 1$ , (c)  $N_s \approx 1$  and (d)  $N_s < 1$ , showing how the lipid shape affects the molecular packing into different structures.

(Figure 1.1d), 'normal' structures are formed, where the head group-tail interface curves towards the tails<sup>2-4</sup>.

The structure can similarly be described by the curvature of the interfacial plane; the (imaginary) plane that lies close to the neutral surface, where the area per molecule does not change upon bending<sup>5</sup>. The interfacial plane can be described in terms of its mean,  $H$ , and Gaussian,  $K$ , curvatures, which are defined as:

$$H = \frac{c_1 + c_2}{2} \quad (1.2)$$

$$K = c_1 c_2 \quad (1.3)$$

where  $c_1$  and  $c_2$  are the principal curvatures at point  $P$  on the interfacial plane and  $c_1 = 1/r_1$ . Conventionally, for a lipid monolayer,  $H > 0$  when the plane curves towards the chain region of the lipid and these structures are termed 'normal' phase, whereas when  $H < 0$ , the plane curves towards the head group (or polar) region and these are called 'inverse' phases. The

Gaussian curvature is more abstract, as it describes the continuity of the structure in different dimensions. For  $K > 0$ , elliptical structures form, which are discontinuous and have closed shells; e.g. micelles. For  $K = 0$  (i.e. when either  $c_1$  or  $c_2$  is zero), parabolic structures form, which are continuous in one direction; e.g. lamellar or hexagonal phases. For  $K < 0$  (i.e. when  $c_1$  and  $c_2$  have opposite signs), the structure is hyperbolic and continuous in all three dimensions; e.g. bicontinuous cubic phases<sup>5</sup>.

## Lipid bulk phases

Figure 1.2 shows the normal and inverse versions of some of the common lipid liquid crystalline (LLC) phases.

A micelle is the simplest structure into which surfactants can self-assemble. In a normal micelle with  $N_s < 1$  (Figure 1.2:  $L_1$ ), the surfactant head group forms a closed sphere at the surface with the aqueous solvent and the tail points inwards, forming a hydrophobic core. For some systems, extended 'wormlike' micelles can also form, which have the shape of an extended cylinder with a hemisphere capping each end<sup>6</sup>.

The normal hexagonal phase (Figure 1.2:  $H_1$ ) is formed of extended cylinders with the head group at the aqueous interface and the tails pointing inwards. These cylinders are closely packed on a hexagonal lattice and have a continuous aqueous phase<sup>5</sup>.

When the respective polar and non-polar volumes of the lipid have approximately the same size (i.e.  $N_s \approx 1$ ), the lipids self-assemble into planar sheets. A single planar sheet, is known as a bilayer with the two layers of lipids referred to as its outer and inner leaflet. The bilayer is the basic structural unit for most biological membranes and some other LLC phases. When multiple bilayers, or lamellae, form stacks, this is referred to as lamellar phase (Figure 1.2,  $L_\alpha$ )<sup>4,5</sup>.

Bicontinuous cubic phases are based on a bilayer draped over an infinite periodic minimal surface (IPMS), forming a network of two distinct interwoven water channels separated by a continuous bilayer, in the inverse case (Figure 1.2:  $Q_2$ ). The three inverse bicontinuous cubic phases Ia3d ( $Q^{230}$ ), Pn3m ( $Q^{224}$ ) and Im3m ( $Q^{229}$ ) are based on the G (gyroid), F (double diamond) and P (primitive) IPMSs, respectively. Due to its distinct and continuous hydrophilic and hydrophobic compartments and large surface area to volume ratio, the  $Q_2$  phase has been extensively investigated for

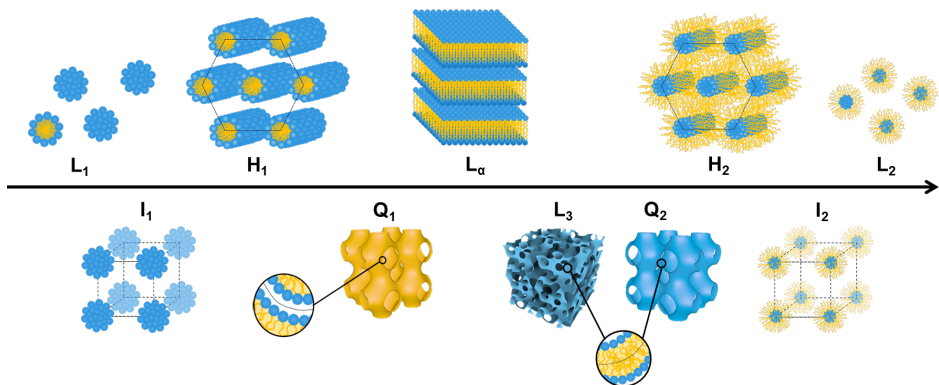


**Figure 1.2** The structural units for different self-assembled lipid structures are presented. From left to right: micellar ( $L_1$ ), micellar cubic ( $I_1$ ), hexagonal ( $H_1$ ), bicontinuous cubic ( $Q_1$ ), lamellar ( $L_\alpha$ ), sponge ( $L_3$ ), inverse bicontinuous cubic ( $Q_2$ ), inverse hexagonal ( $H_2$ ), inverse micellar cubic ( $I_2$ ) and inverse micellar ( $L_2$ ).

delivery and controlled release of small molecule drugs, encapsulation of biomolecules and for membrane protein crystallisation (<sup>7</sup> and ref.s within).

The sponge phase (Figure 1.2:  $L_3$ ) is often referred to as a 'melted cubic phase', in that it has the same short range structure of a network of interwoven water channels separated by a continuous bilayer, but without the same well-defined periodicity and long range order of the cubic phase<sup>5,8</sup>. Typically the sponge phase has larger water pores and a less rigid nanostructure than the cubic phase, making it well-suited to encapsulate large biomolecules<sup>9</sup>.

## Lipid dispersions

The bulk self-assembled lipid structures can often be dispersed into excess water to form nanoparticles with the internal structure retained from the bulk structure, which makes them attractive for use as nanomedicines. For the bulk structures listed above, the corresponding dispersions would be; inverse hexagonal phase to hexosomes, inverse bicontinuous cubic phase to cubosomes, lamellar to vesicles and sponge phase to spongosomes or sponge phase nanoparticles ( $L_3$ NPs). Additional surfactants or surface stabilisers are often required in order to improve the colloidal stability and decrease the polydispersity of the dispersion, but these can have an effect on the internal structure<sup>10</sup>.

### 1.1.2 Dynamics

Often self-assembled lipid structures are presented as static and only their time averaged structures are discussed, like the ones shown in Figure 1.2. In reality, however, at physiological temperatures, they are highly dynamic and undergo significant fluctuations in shape and structure. This is very important in nature, as most systems exist out of equilibrium and are constantly changing to react to changes in the environment.

The dynamics of a lipid bilayer are very hierarchical, meaning that there are many different motions occurring simultaneously over a wide range of length and time scales<sup>11,12</sup>.

**Nanostructure:** On the mesophase scale, membrane remodelling and topological changes occur, such as the making and breaking of water channels in the sponge phase.

**Bilayer:** Collective motions of the bilayer are observed, such as thickness fluctuations and membrane undulations. By measuring these motions, mechanical properties such as bending rigidity can be determined.

**Individual molecule:** Motions of the individual molecule can vary greatly in time scale; protrusion from the bilayer is typically short-lived but the characteristic times for lipid diffusion within the plane of the bilayer and flip flop between bilayer leaflets depend greatly on the system.

**Within the lipid molecule:** The number of degrees of freedom within a molecule vary depending on its structure, which dictate intramolecular motions, such as rotation of terminal methyl groups.

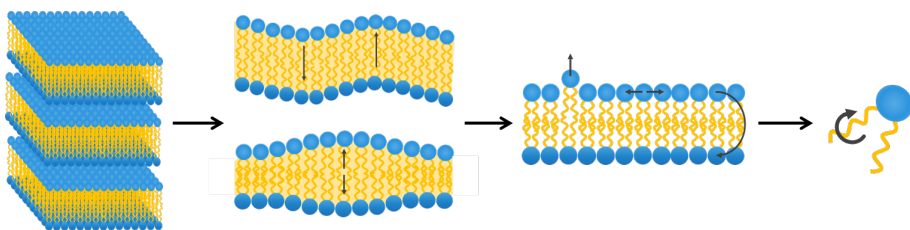


**Figure 1.3** Possible motions occurring within a bilayer stack from the length scale of the periodic repeat unit of the structure to individual groups within the molecule.

### 1.1.3 Factors affecting lipid self-assembly

The self-assembly of lipids, and therefore the formation of these different structures and their dynamics, can be affected by several factors, including the lipids themselves and their surrounding environment<sup>4</sup>.

#### **Lipid composition**

Both the head group and hydrocarbon tail can have a large effect on the  $N_s$ , in terms of their size and their interactions. For the hydrophobic tail, increasing the chain length will increase the effective tail volume, the chain melting temperature and hydrophobicity. The presence of double bonds or bulky groups in the tail can both decrease the chain melting temperature and increase the tail volume. Different head groups will have different sterics, charge/polarity and possibilities for head group-head group or head group-water bonding.

When you start adding other lipids, things become even more complicated. If two lipids with similar biophysical characteristics are mixed, it is likely that there won't be such a big change in the self-assembled structure. If, however, you start mixing lipids with different characteristics, the system becomes more complicated. In a simple scenario, the weighted average of the  $N_s$  can predict the structure. However, with increasing complexity, it becomes increasingly likely that the lipids will not be homogeneously distributed, potentially resulting in effects such as phase separation or asymmetric distribution across lipid bilayer leaflets<sup>5</sup>.

#### **Temperature**

In LLC phases, the lipid tails are, as the name suggests, in a disordered, liquid like state and can adopt a range of conformations. As the temperature increases, the tails can move through a larger volume with increasing trans-gauche isomerisation, increasing their effective volume and  $N_s$ <sup>13</sup>.

#### **Hydration**

The effective area of the head group considers not only the size of the actual lipid head group, but also the molecules and ions associated with it. Addition of hydration water will, therefore, increase the effective cross sectional area of the head group<sup>5</sup>. Water also plays a stabilising role by forming water bridges between lipid head groups, thereby reducing head group mobility<sup>14,15</sup>.

#### **Solution conditions:**

Buffer ions: Typically polar solutes, such as buffer ions, dehydrate the lipid

head groups by competing with the lipid to interact with water molecules or even binding to the lipid head group itself, displacing water molecules. For specific strongly hydrophilic ions, however, this binding can actually enhance the hydration. For charged lipids, ions will additionally screen the head group charges, reducing electrostatic repulsion.

pH: The effect of pH strongly depends on the pKa of any ionisable groups in the system, which can change extensively depending on their environment. Changing the pH can affect the polar head group-head group interactions, even to the extent of head group (de)protonation, thereby possibly strengthening or weakening electrostatic interactions in the systems or changing them e.g. from attractive to repulsive.

### Additives

Introducing an 'additive' to a system could range from introducing a simple co-surfactant like ethanol to a bacterial membrane in the form of hand sanitiser to the presence of complex biomolecules like nucleic acids and proteins in the cell membrane. As there is a massive range of possible additives, there is an equally massive range of possible effects depending on the extent to which they interact with the lipids and with which part of the structure they interact.

#### 1.1.4 System 1: Sponge phase ( $L_3$ ) for protein encapsulation

The first system investigated in this thesis was made up of Capmul GMO-50, diglycerol monooleate and polysorbate 80, which formed a swollen lipid sponge phase ( $L_3$ ).

Capmul GMO-50 (GMO-50) is a commercially available mixture of monoglycerides (53.8%), diglycerides (15-35%) and triglycerides (2-10%). The main fatty acid chain is oleic (18:1, 86.6%), with others including linoleic (18:2, 4.9%), palmitic (16:0, 4.1%) and stearic (18:0, 3.3%). The main component of GMO-50 is glycerol monooleate (GMO), which has a rich binary phase diagram with water and typically forms structures with  $H \leq 0$  ( $N_s \geq 1$ ), due to the large volume occupied by the tail as a result of the double bond between C9 and C10<sup>16</sup>. The additional di- and triglycerides present in GMO-50 increase this curvature even further, due to the additional acyl chains. As a result, GMO-50/water forms an inverse hexagonal ( $H_2$ ) phase compared to the lamellar ( $L_\alpha$ ) and inverse bicontinuous cubic phases ( $Q_2$ ) formed by GMO/water at low and high water content, respectively<sup>9,16-19</sup>.

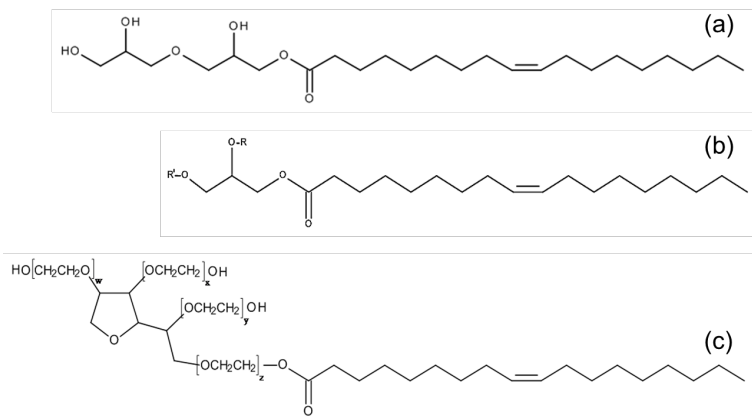


**Figure 1.4** L<sub>3</sub> lipids. (a) DGMO, (b) GMO-50 where R(′)=H or 18:1, (c) P80 where x+y+z=20.

Diglycerol monooleate (DGMO) has an additional glycerol in the head group, therefore has a lower curvature and DGMO/water mixtures instead form lamellar phase<sup>9</sup>. Consequently the DGMO/GMO-50/water ternary phase diagram, has larger regions of L<sub>α</sub> and Q<sub>2</sub> and an additional sponge (L<sub>3</sub>) phase region compared to the binary systems<sup>9,20</sup>.

Polysorbate 80 (P80) is a non-ionic polymeric surfactant commonly used as a solubilising agent and surface stabiliser. It has the same oleic acid chain as GMO and DGMO, but with a very large branched head group. This gives it a low N<sub>s</sub>, and it forms micelles at room temperature (RT) when dispersed in water<sup>21,22</sup>. The effect of adding P80 to the DGMO/GMO-50/water system is two-fold<sup>9,21,22</sup>:

- (i) the addition of a component with a very large head group reduces the overall curvature, shifting the system towards forming structures with lower curvature,
- (ii) when the bulk phase is dispersed into nanoparticles, enrichment of P80 at the particle surface helps to stabilise the particle.

These components were chosen due to their approval by the Food and Drug Administration (FDA) for use in food products, alongside their ability to form L<sub>3</sub> phases, making them compatible with the potential applications for the encapsulated proteins investigated in this thesis<sup>23</sup>.

An additional key feature of the system is the ability to prepare and disperse the bulk phase into nanoparticles by shaking, i.e. without high energy



input, such as ultrasonication, or organic solvents, which have traditionally been used. This is vital for the encapsulation of fragile biomolecules, like proteins which would be denatured by these harsh methods<sup>9,21,24,25</sup>.

In Papers I-III, the L<sub>3</sub> phase formed of GMO-50/DGMO/P80 was studied for the encapsulation of proteins with different sizes and structures. Both the bulk phase and the dispersions were studied in order to understand how the encapsulation of the protein affected both the lipid structure and dynamics, as well as the protein structure and functionality. Additionally the effect of common buffers used with these proteins (phosphate, acetate and Tris) on the L<sub>3</sub> structure was studied at different pHs.

### 1.1.5 System 2: Lipid nanoparticles for nucleic acid delivery

The second system investigated in this thesis is based on a common lipid composition successfully used in mRNA delivery in *in vitro* cell studies and is closely related to the composition of the mRNA LNP based SARS-Cov-2 vaccines mRNA-1273<sup>26</sup> and BNT162b<sup>27</sup>. The general formulation for the cationic ionisable lipid-containing lipid nanoparticles contains a cationic ionisable lipid (CIL), cholesterol, a neutral helper lipid and a PEG-lipid.

CILs were developed to address some of the challenges associated with encapsulation of nucleic acids (NAs) in lipid nanoparticles (LNPs) for NA based drug delivery<sup>28</sup>. The most successful CILs, including DLin-MC3-DMA (MC3), ALC-0315 (BioNTech/Pfizer SARS-Cov-2 vaccine) and SM-102 (Moderna SARS-Cov-2 vaccine), are positively charged at the low pH used during the initial LNP formulation step and neutral at physiological pH. This improves the encapsulation efficiency for the NA cargo during formulation while avoiding the degree of toxicity associated with cationic lipid formulations<sup>26,27,29-32</sup>. Subsequent optimisation of CIL structure, including unsaturation in the lipid tails and pKa of the ionisable group, have shown that a pKa between 6 and 7 is optimal with respect to delivery and transfection efficacy<sup>33-36</sup>. It should be noted, however, that this optimal pKa between 6 and 7 is the apparent pKa of the CIL in the interior of the LNP. The pKa of the free monomer in water of each previously mentioned lipid is higher (MC3: 9.47<sup>35</sup>, ALC-0315: 7.8<sup>37</sup>, SM-102: 8.0<sup>37</sup>) and that this optimal pKa value has mostly been discussed with respect to siRNA delivery. Additionally, these lipids all have high N<sub>s</sub> and a strong preference for forming inverse structures<sup>34,37</sup>. Here, we used the CIL MC3, one of the most effective and widely used CILs in research, which has two *cis*-double

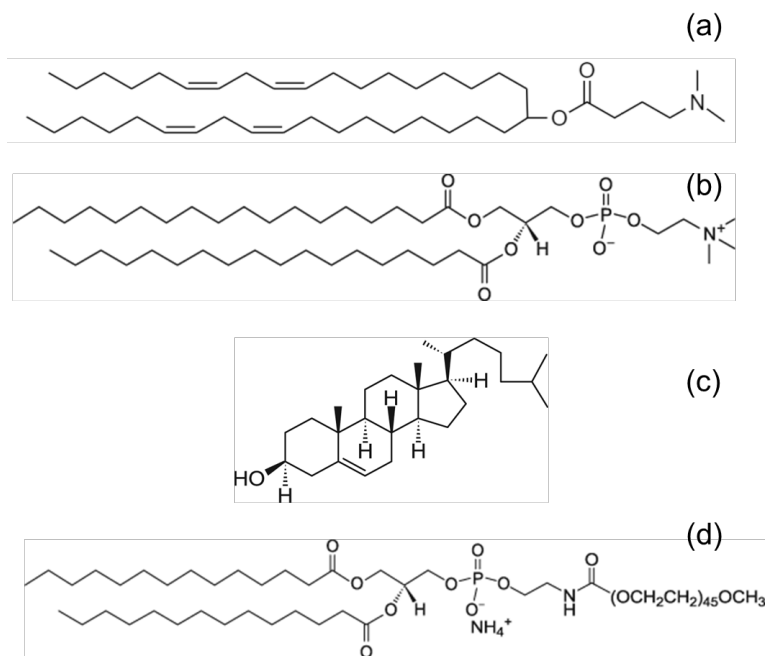


**Figure 1.5** LNP lipids. (a) MC3, (b) DSPC, (c) Cholesterol, (d) DMPE-PEG<sub>2000</sub>.

bonds in each tail and an amino head group (Figure 1.5) with an apparent pKa of 6.44 in the interior of an LNP<sup>34</sup>.

The remaining lipid components forming this system are cholesterol, DSPC and DMPE-PEG2000. Cholesterol is present in both the core and shell, whereas DSPC is present only in the shell. DMPE-PEG2000 is at the LNP surface, providing steric stabilisation for the particle and controlling its size.

Nanoparticles for this system are prepared via microfluidic mixing of the lipid mixture in ethanol with the nucleic acid cargo in a low pH aqueous solution. The mixture is then dialysed, to remove the ethanol and bring the pH and salt concentration to physiological conditions, and finally concentrated via centrifugation to the final formulation.

Although this type of formulation has often been discussed as a 'delivery platform', assuming that the cargo has no effect on the structure, it is becoming increasingly clear that this is not the case. In Paper IV, we have studied a model lipid system composed of DOPC and MC3 in different ratios and its interactions with different mRNAs in a cell relevant pH range.

In Papers V and VI, we apply these findings to discuss the effect of different NA cargos and cargo concentrations with a benchmark NA LNP lipid formulation on the LNP colloidal stability, the lipid composition in different compartments of the LNP and the structure of the LNP core.

## 1.2 What is a protein and why do we care?

The second type of biological building block relevant to this thesis are proteins. Proteins are the most multi-functional group of biomolecules, which are involved in almost all biological processes. Unsurprisingly, there is massive variation in protein structure to address this abundance of functions; from integral membrane proteins, like ion channels which allow selective uptake of ions across a membrane at a rate of  $1 \times 10^8 \text{ s}^{-1}$ <sup>38</sup>, to structural proteins, like collagen which forms the major structural element of the body's connective tissues<sup>39</sup>, and enzymes, like lipases which break down triglycerides during digestion<sup>40</sup>. Typically proteins are described as having a strongly hierarchical structure with several layers of self-assembly:

**Primary structure:** Amino acid sequence

Proteins are composed of a linear chain of amino acid units linked by amide bonds. There are 20 different amino acids which consist of a central carbon connected to an amino group, a hydrogen atom and a side chain. It is this side chain that differs between each amino acid and allows them to be roughly grouped into the following categories: hydrophobic, polar, positively charged and negatively charged.

**Secondary structure:** Local spatial arrangement

Flexibility of the amino acid backbone, steric exclusion of the side chains and optimisation of H-bonding between the amino acids limit the possible local conformations the polypeptide chain can adopt. As a result, proteins tend to fold into a few well-defined local structures;  $\alpha$  helices,  $\beta$  sheets and  $\Omega$  loops.

**Tertiary structure:** Protein folding

Most proteins further fold these local structures into an even more complex structure based on its surroundings. For a protein in solution, this is typically driven by the removal and sequestration of the hydrophobic and/or fully H-bonded residues from the aqueous medium and the presence of amino acids at the surface which are charged, polar and/or available for H-bonding<sup>41</sup>.

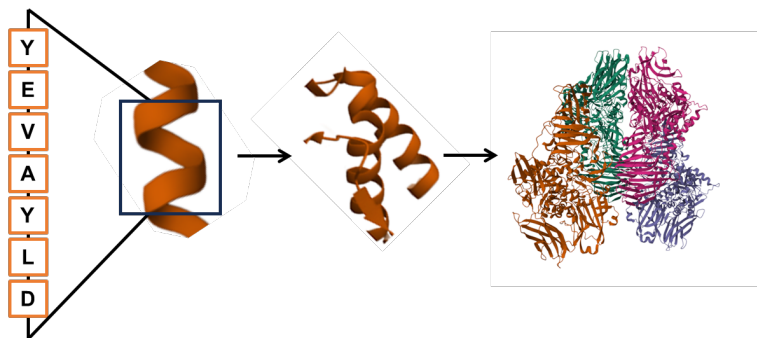


**Figure 1.6** Levels of protein structure demonstrated using  $\beta$ -galactosidase (PDB: 3OBA<sup>42,43</sup>) from the amino acid sequence (primary), to the local  $\alpha$  helix (secondary), to protein folding (tertiary) and tetramer formation (quaternary).

### Quaternary structure: Multi sub unit proteins

If a protein is made up of multiple sub-units, there can be an additional fourth level of structure, which describes the arrangement of and interactions between sub-units in a protein<sup>41</sup>.

Each level of protein structure is often key for its function. The active site of an enzyme, for example, is usually formed by groups that come from far apart in the protein chain and has a very specific microenvironment. The specific folding required to bring them into close contact is vital to the enzyme function.

Most of the interactions dictating the secondary, tertiary and quaternary protein structure are non-covalent, therefore are relatively weak and require little energy to disrupt<sup>41</sup>. As a result, proteins are typically easily denatured by heat, high concentrations of salt, shaking, excessive dilution or concentration, etc.

In the following section, the proteins studied in Papers I-III of this thesis are introduced, including key physicochemical properties presented in Table 1.1 and their 3D structure in Figure 1.8.

#### 1.2.1 $\beta$ -galactosidase

$\beta$ -galactosidase (from *Kluyveromyces Lactis*) is one of the most important enzymes in the food industry. It is used to cleave lactose into glucose and galactose, most commonly to make lactose free dairy products<sup>44</sup>.

$\beta$ -galactosidase is a tetramer (4128 residues, 476 kDa) made up of four

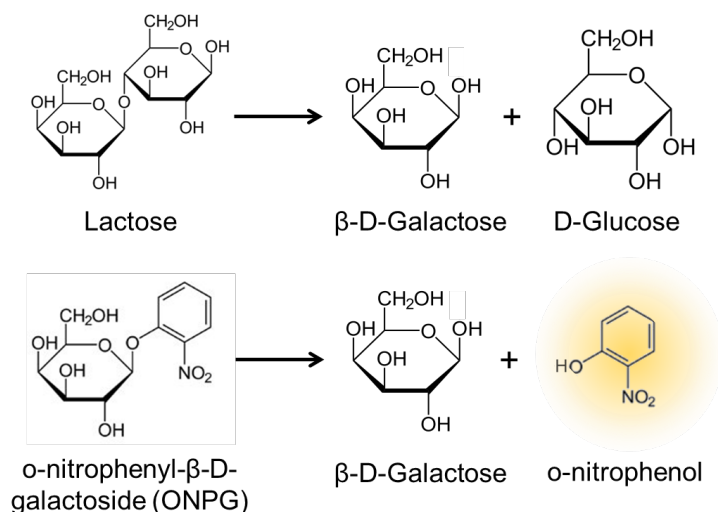


**Figure 1.7**  $\beta$ -galactosidase catalysed reactions. (Top) Lactose hydrolysis, (Bottom) ONPG hydrolysis

identical monomeric subunits (119 kDa), which associate initially into dimers, which in turn associate to form the tetramer<sup>43,45</sup>. Both the tetrameric and dimeric forms are enzymatically active, but the monomeric is not (<sup>45</sup> and refs within), as the catalytic pocket is formed at the interface between two dimerised monomers<sup>43</sup>. As the dissociation energy of the tetramer to dimers is low (6 kcal/mol) compared to that of the dimer to monomers (20 kcal/mol), the different forms of  $\beta$ -galactosidase likely exist in equilibrium with each other<sup>43</sup>. The  $\beta$ -galactosidase used in this work came from Ha-Lactase 5200, composed of 50% glycerol (E422), water and neutral  $\beta$ -galactosidase<sup>46</sup>. After dialysis of Ha-Lactase 5200 to remove the glycerol, the enzyme is mostly in its dimeric form<sup>25</sup>.

The biological function of  $\beta$ -galactosidase is the catalysis of the hydrolysis of lactose into D-glucose and D-galactose (Figure 1.7). In order to measure the activity of  $\beta$ -galactosidase, however, it is more convenient to use the synthetic substrate o-nitrophenyl- $\beta$ -D-galactoside (ONPG), as this is cleaved by  $\beta$ -galactosidase into D-galactose and o-nitrophenol (Figure 1.7), which can be measured spectrophotometrically at  $\lambda = 420 \text{ nm}$ <sup>47</sup>.

### 1.2.2 Aspartic protease

Aspartic proteases are another type of protein relevant for food industry applications, as they are used in the cheese ripening process. By cleaving  $\kappa$ -casein, a protein found in milk, at a specific site, endothiapepsin accelerates the coagulation of milk into curd, which is then dehydrated, compressed and matured to produce the desired cheese<sup>48,49</sup>.

The aspartic protease (from *Cryphonectria parasitica*) used here is a monomer (329 residues, 34 kDa) and came from Thermolase 625, composed of glycerol, water and endothiapepsin<sup>50,51</sup>. Thermolase 625 was dialysed before use to remove the glycerol.

### 1.2.3 Phytoglobin BvPgb 1.2

Recently phytoglobins, haemoglobins from plants, have been shown to have the same globin fold as human haemoglobin, but with a higher oxygen affinity and thermal and oxidative stability, generating interest for their use in biotechnical applications<sup>52-54</sup>. In particular, BvPgb 1.2, a phytoglobin isolated from sugar beet (*Beta vulgaris* ssp. *vulgaris*) demonstrated high thermal stability and no haeme loss, making it an attractive candidate for use in dietary supplements with haeme bound iron or meat analogues.

BvPgb 1.2 exists as a homodimer (342 residues, 38.4 kDa) containing the typical globin fold, made up of 8 right handed  $\alpha$ -helices joined by random coils, and a hexacoordinated haeme group<sup>55</sup>.

### 1.2.4 Myoglobin

Myoglobin is an oxygen binding protein found primarily in muscle. Here the main interest in myoglobin was as a structurally similar comparison for BvPgb 1.2, as myoglobin contains a pentacoordinated haeme group and has a higher affinity for oxygen than haemoglobin<sup>56</sup>.

The horse skeletal myoglobin used here is a monomer (153 residues, 17.6 kDa) with the haeme group buried between helices 5 and 6 of the globin fold<sup>56,57</sup>.

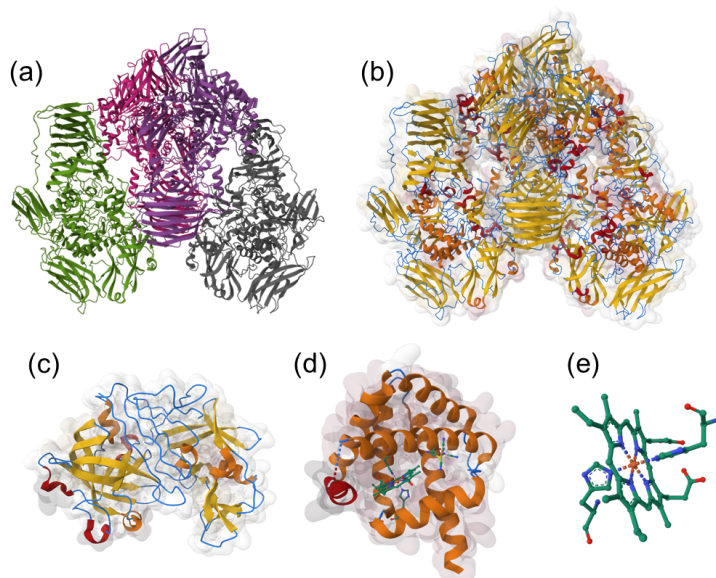


**Figure 1.8** 3D structures of the proteins discussed in this thesis. (a) shows  $\beta$ -galactosidase with the each monomeric subunit in a different colour. The secondary structures of (b)  $\beta$ -galactosidase (3OBA), (c) aspartic protease (1OEW) and (d) BvPgb1.2 monomeric subunit (7ZOS) are shown with three-ten helices in red,  $\alpha$  helices in orange, beta strands in yellow and coils in blue<sup>43,50,55</sup>. In (e), the haeme sub-unit shown in (d) is highlighted, with the two distal histidine residues complexed with the central Fe atom, with Fe in orange, C in green, N in blue and O in red. These images were generated using Mol\*<sup>42</sup>.

**Table 1.1** Table containing key physicochemical properties of the proteins investigated in this thesis.

Protein	PDB code	MW/kDa	$R_h/\text{\AA}$	pI
$\beta$ -galactosidase ( <i>K. lactis</i> )	3OBA	476 (tetramer) <sup>43</sup>	-	5.41/5.58 <sup>23</sup>
		238 (dimer)	59 <sup>25</sup>	5.34 <sup>25</sup>
Aspartic protease ( <i>C. parasitica</i> )	1OEW	34 <sup>50</sup>	30 <sup>24</sup>	4.14/4.40 <sup>23</sup>
Phytoglobin ( <i>Beta vulgaris</i> )	7ZOS	38.4 (dimer) <sup>55</sup>	34 <sup>58</sup>	8.32 <sup>58</sup>
		19.2 (monomer)	-	7.35 <sup>58</sup>
Myoglobin	-	17.6 <sup>57</sup>	22 <sup>58</sup>	7.3/6.8 <sup>59</sup>

### 1.3 What is a nucleic acid and why do we care?

The final type of building block included in this thesis are nucleic acids (NAs). Nucleic acids are responsible for information storage and transfer in the cell; the sequence of the bases in deoxyribonucleic acid (DNA) defines

your genes. These are transcribed to ribonucleic acid (RNA), which serves as a template for protein synthesis.

Single strands of both DNA and RNA are composed of a linear chain of nucleotides, which are made up of a phosphate, a sugar and a base. The nucleotides are linked by phosphodiester bonds between the OH on the 3' carbon of the sugar to the phosphate and between the phosphate and the OH on the 5' carbon of the following sugar. This forms a negatively charged phosphate-sugar backbone with the bases bonded to the 1' carbon and extending to the side of the backbone.

The difference between the backbones of DNA and RNA lie in the sugar group: DNA has deoxyribose sugar units, which have an H on the 2' carbon, whereas RNA has ribose units, which have an OH group on the 2' carbon. This makes the DNA backbone less vulnerable to nucleophilic attack, therefore more stable to hydrolysis than RNA.

Both DNA and RNA have four possible bases, shown in Figure 1.9. For both NAs; adenine (A), guanine (G) and cytosine (C); for DNA only, thymine (T); and for RNA only, uracil (U). These are derivatives of two different structures; purine in the case of A and G, and pyrimidine for C, T and U.

DNA typically exists as a right handed double helix (Figure 1.10a), with the backbone on the outside and the bases paired with those in the opposite strand. The main driving force for this base pairing comes from the hydrophobic effect, as the more hydrophobic bases cluster inside the helix and the negatively charged backbone is in contact with the surrounding aqueous environment. The strand is additionally stabilised by specific hydrogen bonds between the A-T and C-G bases and van der Waals forces between the stacked base pairs. By heating above its melting temperature or adding strong acid/alkali, the DNA double helix can reversibly dissociate into single strands, which reform when the change is reversed<sup>41</sup>.

RNA, however, is usually present as a single strand, therefore is more flexible and base pairing between short sections of the strand ( $\geq 3$  base pairs) can result in a wide variety of complex structures. Both canonical (A-U and G-C) and non-canonical base pairing, the most common of which is the 'G-U wobble', and hydrogen bonding can contribute to the formation of structures such as hairpin stems and loops (Figure 1.10 (b)), bulges, internal loops and 3 way junctions<sup>60,61</sup>. These structures can then fold into tertiary structures, analogously to protein folding. The structure also tends to be highly dynamic and responsive to environmental conditions, resulting



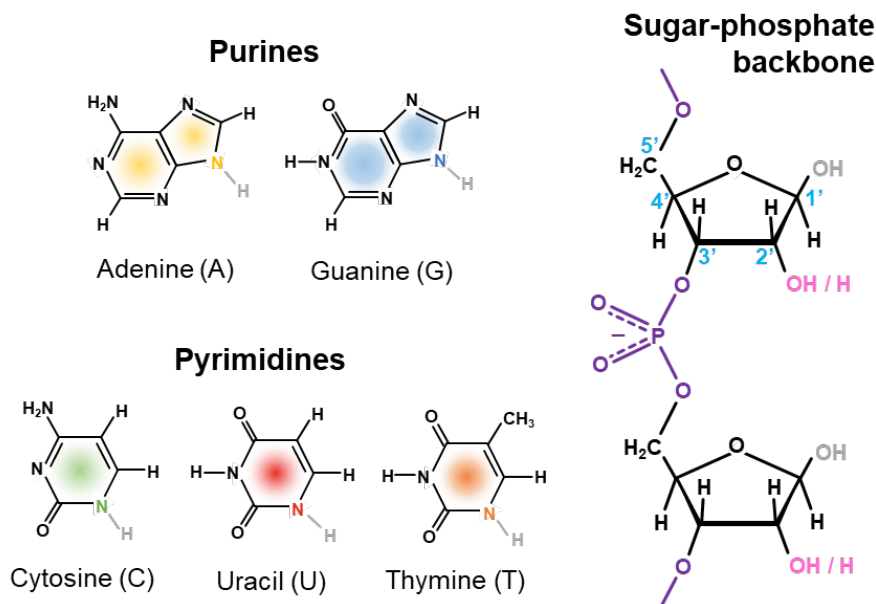


**Figure 1.9** The bases of DNA and RNA are shown to the left and the structure of the sugar (black) - phosphate (purple) backbone is shown to the right. The base is linked to the sugar via a glycosidic linkage between the coloured nitrogen in the base structure and the 1' carbon on the sugar, labelled in blue. When this bond is formed, the H on the base and the OH on the sugar, labelled in grey, are lost as water. On the 2' carbon, DNA has an H and RNA has an OH group, highlighted in pink.

in multiple coexisting states for the same RNA sequence<sup>61</sup>.

In the following section, the nucleic acids used in Papers IV - VI are introduced, where we focus specifically on the difference in the interaction between the formulation lipids with; (i) single stranded DNA (ssDNA) and double stranded DNA (dsDNA) and (ii) coding and model messenger RNA (mRNA).

### 1.3.1 Calf thymus DNA

Commercially available sonicated DNA from calf thymus was used as a model DNA source. The length of the DNA fragments was 587 - 831 base pairs and the sequence was unknown, but assumed to contain an equal proportion of A, G, C and T bases.

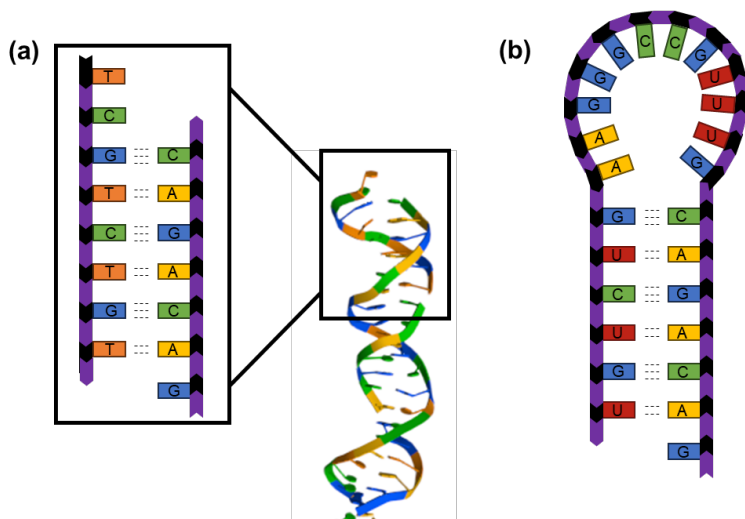


**Figure 1.10** (a) Example of base pairing between two strands of DNA to form a double helix. The double strand image in (a) was generated using Mol\*<sup>42</sup> from PDB entry 3NAO<sup>62</sup>. (b) Example of a hairpin stem-loop, which can be formed by single strands of NAs, using a single RNA strand.

### 1.3.2 Erythropoietin mRNA

Erythropoietin (EPO) mRNA was used as a representative mRNA molecule. The EPO mRNA used here codes for the human EPO protein, which controls red blood cell production<sup>63</sup>. The sequence is 858 nucleotides (nt) and contains 15.8 % A, 35.4 % G, 35.7 % C and 13.1 % U in the main sequence with a polyadenylated tail<sup>64</sup>.

### 1.3.3 Model mRNA

Typically optimisation of LNP systems and structural studies require relatively large quantities of NA material, such that the cost of the NA can become a limiting factor in such studies<sup>65,66</sup>. 'Model mRNAs' present a more accessible option, as they are both cheaper, commercially available in larger quantities and well characterised.

In this thesis, we have used two model mRNAs; polyadenylic acid (polyA) and polyuridylic acid (polyU), which are synthetic homopolymers of the RNA nucleotides adenosine and uracil respectively. Despite the fact that in this context, NAs are often treated as negatively charged polyelectrolytes, over the pH range investigated in this thesis and relevant to RNA-LNP

formulation, polyA undergoes several structural transitions (<sup>67</sup> and ref.s within). In physiological pH ( $\geq 7.3$ ), polyA exists as a single stranded, right handed helix containing coil domains<sup>67</sup>. Decreasing the pH to  $\approx 6.5$  (pH 6.2 - 6.5), these single strands start to form double stranded structures. Initially the intermediate 'basic' (B) structure dominates, coexisting with the tightly packed 'acidic' (A) form at  $\approx$ pH 6, which becomes gel-like in appearance at lower pH ( $\leq 4$ )<sup>68,69</sup>. polyU, on the other hand, exists as a random coil in the conditions investigated here (<sup>70</sup> and ref.s within).

Both model mRNAs have are polydisperse and have a wide distribution of chain lengths: for polyA,  $\approx 2200 - 11,100$  nt (700 - 3500 kDa) and for polyU,  $\approx 350 - 3500$  nt (100 - 1000 kDa)<sup>37,71</sup>.

## 2

# Methods

In this chapter, the experimental techniques used throughout this thesis are introduced.

Three types of samples were characterised in this work: bulk LLC phases, lipid nanoparticle dispersions and supported lipid layers. A summary of the different techniques used to characterise the structure, dynamics, interactions, composition and size of the samples are summarised in Figure 2.1.

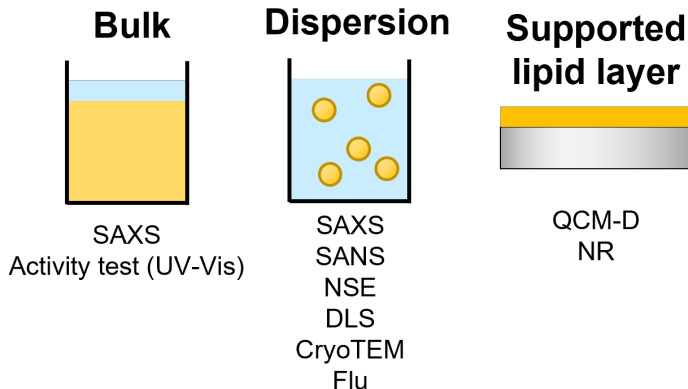


**Figure 2.1** Summary of the experimental techniques used in this thesis to characterise lipid bulk phases, dispersions and deposited layers, including small angle x-ray/neutron scattering (SAX/NS), activity test using ultraviolet-visible spectroscopy (Activity test(UV-Vis)), neutron spin echo spectroscopy (NSE), dynamic light scattering (DLS), cryogenic transmission electron microscopy (cryoTEM), fluorescence spectroscopy (Flu), quartz crystal microbalance with dissipation monitoring (QCM-D) and neutron reflectometry (NR).

## 2.1 Bulk scattering techniques

Many of the techniques used in this thesis are based on the interaction between radiation and matter. Depending on the energy, therefore wavelength, of radiation used, different length scales can be interrogated. Here, we have used x-rays and neutrons to investigate the length scales 1 - 600 nm, corresponding to particle size and structure, and visible light to monitor larger sizes, including particle aggregation<sup>72</sup>.

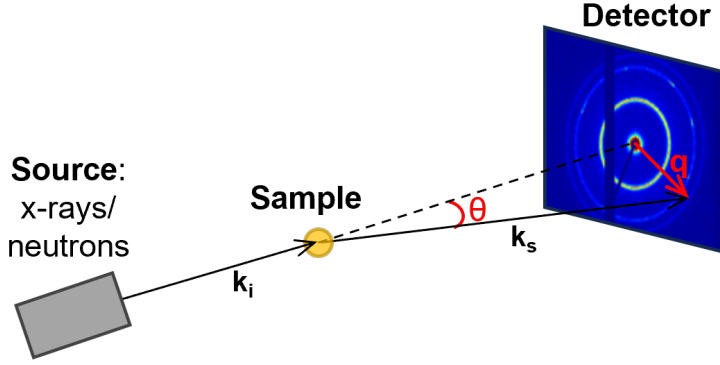


Figure 2.2 Schematic representation of a small angle scattering experiment.

### 2.1.1 Small angle scattering (SAS)

In small angle scattering, the elastic scattering of radiation by the sample is measured, which provides information about the time averaged structure of the system.

In a typical SAS experiment (Figure 2.2), the incident beam with a well defined energy and direction is scattered elastically by the sample (i.e. it undergoes a change in direction, but not energy) and the intensity of the scattered beam is recorded on a 2D detector<sup>72</sup>. If the sample is isotropic (i.e. the sample is randomly oriented), like a micellar dispersion, the scattering pattern will appear as concentric circles (like the inner rings in Figure 2.3). If the sample is anisotropic (i.e. the sample is at least partially oriented), like an aligned multilamellar stack, the scattering pattern will have modulations in intensity in these rings (like the outer ring in Figure 2.3). The difference between the wave vector of the incident beam ( $\mathbf{k}_i$ ) and the scattered beam ( $\mathbf{k}_s$ ) is known as the scattering vector  $\mathbf{q}$ , defined as:

$$\mathbf{q} = \frac{4\pi}{\lambda} \sin\left(\frac{\theta}{2}\right) \quad (2.1)$$

For elastic scattering, the amplitude of the scattered wave  $A(\mathbf{q})$  from  $N$  atoms in vacuum is:

$$A(\mathbf{q}) = \sum_{j=1}^N b_j e^{-i\mathbf{q} \cdot \mathbf{r}_j} \quad (2.2)$$

where  $e^{-i\mathbf{q} \cdot \mathbf{r}_j}$  describes a complex wave and  $b_j$  is the scattering length of atom  $j$ .  $b_j$  is a measure of how strongly an atom interacts with the incident

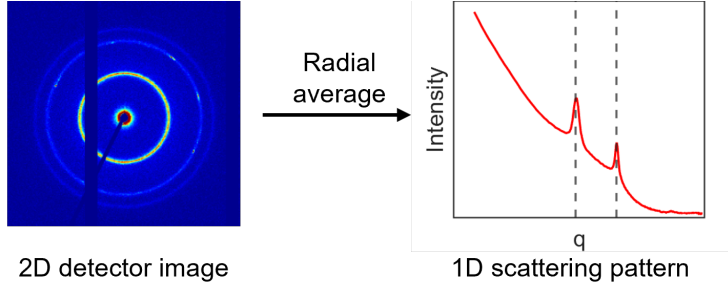


**Figure 2.3** Radial averaging of a 2D detector image to a 1D scattering pattern. The peak positions in the 1D scattering pattern have a ratio of 1:2 indicating that this sample is lamellar.

radiation and varies with atom and radiation type. In a real SAS sample, it is often a particle or molecule that acts as the scattering centre, and it is instead more useful to use the scattering length density, SLD,  $\rho = \sum_j b_j/V_p$  (i.e. the sum of all the scattering lengths of the atoms in a molecule or particle divided by its volume). The scattering can then be defined using a continuum description as follows:

$$A(\mathbf{q}) = \int_V \rho(\mathbf{r}) e^{-i\mathbf{q} \cdot \mathbf{r}_j} d\mathbf{r} \quad (2.3)$$

where  $\rho(\mathbf{r})$  is the distribution of SLD in space. In a scattering experiment, the intensity  $I(q)$  of the scattered beam is measured. As  $I(q) = |A(\mathbf{q})|^2$ , the phase information contained in the complex term is lost, which is known as "the phase problem". Consequently it is not possible to obtain the scattering length density distribution by inverse Fourier transform and we must instead use alternative methods of data analysis<sup>72</sup>.

For the purpose of SAS data analysis, the intensity measured from a 2D detector image is commonly radially averaged, scaled to absolute intensity and presented as a 1D scattering pattern (Figure 2.3). This can generally be expressed as:

$$I(q) = \phi_p V_p \Delta\rho^2 P(q) S(q) + B \quad (2.4)$$

where  $\phi_p$  is the volume fraction of particles in the sample,  $V_p$  is the particle volume,  $\Delta\rho$  is the difference in SLD between the particles and the solvent,  $P(q)$  is the form factor,  $S(q)$  is the structure factor and  $B$  is the background, which usually comes from incoherent scattering.  $P(q)$  describes the intraparticle interference, i.e. the size and shape of the scattering particle.  $S(q)$  describes the interparticle interactions, i.e. the periodic arrangement of the scattering particles. At very low particle concentrations (i.e. dilute systems),  $S(q) \rightarrow 1$  and interparticle interactions can be ignored.

**Table 2.1** Table of the ratio of the Bragg peak positions of different bicontinuous cubic phases.

Phase	Ratio of peak positions
Q <sub>2</sub> with Pn3m space group	$\sqrt{2}, \sqrt{3}, \sqrt{4}, \sqrt{6}, \sqrt{8}...$
Q <sub>2</sub> with Im3m space group	$\sqrt{2}, \sqrt{4}, \sqrt{6}, \sqrt{8}, \sqrt{10}...$

If the scattering objects have a highly periodic arrangement (i.e. a well defined repeat distance), such as in lipid liquid crystals, interference between scattered waves is constructive, resulting in sharp, intense peaks. These are known as Bragg peaks, as they are observed when Bragg’s law is satisfied:

$$n\lambda = 2d_{hkl}\sin(\frac{\theta_{hkl}}{2}) \quad (2.5)$$

where  $n$  is an integer,  $\lambda$  is the wavelength of the scattered radiation,  $d_{hkl}$  is the spacing between the crystal planes with Miller indices  $h,k,l$  and  $\theta$  is the scattering angle, as defined in Figure 2.2. Depending on the structure, reflections with different values of  $h,k,l$  are allowed or forbidden, therefore the positions of the peaks observed in the SAXS data can be used to determine the structure of the sample<sup>5</sup>. In this thesis, this approach was used for the determination of different bicontinuous cubic phase structures (see Table 2.1)<sup>73</sup>.

For more disordered systems, however, the data is much more ambiguous and it is incredibly important to have sufficient complementary data and prior knowledge of the system<sup>72</sup>. In the case of the lipid L<sub>3</sub> phase, for example, in the scattering pattern for the bulk phase, there are two characteristic broad peaks present. The lower  $q$  peak ( $\approx 0.05 \text{ \AA}^{-1}$ ) corresponds to the cell-cell correlation distance and the high  $q$  peak ( $\approx 0.11 \text{ \AA}^{-1}$ ) can be attributed to the bilayer form factor. These peaks could only be confidently assigned, however, by looking at neighbouring phases in the phase diagram and complementary microscopy images<sup>9</sup>.

Data can also be fitted with mathematical models in order to extract additional information about the sample. When fitting scattering data, the choice of model is key. SAS data is often quite featureless and could be fit very well with multiple, very different models, therefore it is very important to know your system well. This is especially the case for many soft matter systems, where the models can be complex and have a large number of fitting parameters. In order to have an overdetermined system, the number of fitting parameters in the model should be lower than the number of datasets for the sample. It is therefore vital to (a) use as simple



a model as possible, in order to minimise the number of fitting parameters, (b) estimate and constrain the fitting parameters and range as much as possible from prior knowledge of the system and complementary data, and (c) measure the sample in different conditions (e.g. in different solvent contrasts), in order to constrain unknown but constant fitting parameters in the model<sup>72</sup>.

## Small angle x-ray scattering (SAXS)

In small angle x-ray scattering, an x-ray beam interacts with the electron clouds of the atoms in the sample. The contrast between different materials therefore depends on the electron density of the sample atoms, with  $b_{x\text{-ray}}$  increasing with proton number. In soft matter, however, a sample is typically composed of H, C, N and O, which have similarly low proton numbers. There is, therefore, very low contrast between different parts of the lipid (head group vs tail), but sufficient contrast between (e.g.) a lipid bilayer and water. Along with the accessibility of lab based x-ray sources, this makes SAXS well suited for LLC phase assignment. For more complex experiments, such as time resolved measurements or very weakly scattering samples, the higher flux and resolution of a synchrotron source are required<sup>72</sup>.

SAXS measurements were used in Papers I and III to study the effect of encapsulated protein and dispersing medium on the structure of sponge phase in bulk and dispersions. In Papers V and VI, *in situ* SAXS during microfluidic mixing and static SAXS of the final formulation was used to study the effect of different cargos and cargo loadings on the internal structure of LNPs for NA delivery. These SAXS measurements were performed on the CoSAXS beamline at MAX IV Laboratory (Lund, Sweden), as well as using the inhouse instrument SAXSLab Ganesha 300XL (SAXSLab ApS, Denmark).

## Small angle neutron scattering (SANS)

In small angle neutron scattering, neutrons interact with the nuclei in the sample. The contrast between different materials, therefore, depends on the composition of the nucleus and the scattering length differs for isotopes of the same element. Unlike  $b_{x\text{-ray}}$ , neutron scattering lengths  $b_{\text{neutron}}$  do not appear to follow a trend and vary randomly between elements and

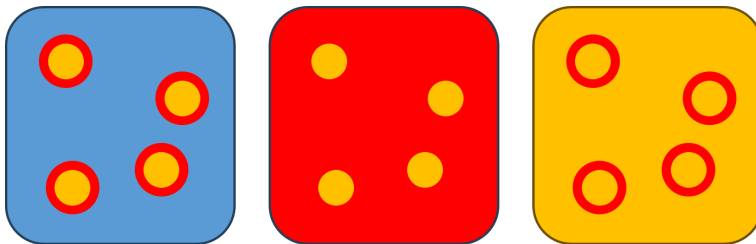


**Figure 2.4** An example of using solvent contrast variation to highlight different parts of a core shell structure. (Left) The core (yellow) shell (red) particles in a solvent (blue) which is not matched to any part of the particle. (Middle) Particles in a solvent matched to the shell SLD, highlighting the core. (Right) Particles in a solvent matched to the core SLD, highlighting the shell.

isotopes. This is incredibly useful in soft matter, as there is natural contrast between different (parts of) biomolecules (e.g. SLD of RNA  $\geq 3 \times 10^{-6} \text{ \AA}^{-2}$  vs SLD of lipid  $\approx 0.2 \times 10^{-6} \text{ \AA}^{-2}$ ) and isotopic substitution can be used to tune the SLD of a system to highlight or match out parts of a sample, as shown in Figure 2.4.

One simple way to do this is to change the SLD of the solvent by varying the ratio of  $\text{H}_2\text{O}$  (SLD =  $-0.56 \times 10^{-6} \text{ \AA}^{-2}$ ) and  $\text{D}_2\text{O}$  (SLD =  $6.36 \times 10^{-6} \text{ \AA}^{-2}$ ) used to make a buffer. Alternatively, the lipid components themselves can be exchanged for their partially or fully deuterated analogues. This enables us to obtain different information about a sample with minimal perturbation to the structure, therefore providing different information for the same sample for simultaneous model fitting<sup>72</sup>.

SANS was used in Papers V and VI to determine the structure of NA LNPs and contrast variation allowed us to highlight different parts of the core shell structure of NA LNPs in order to determine the lipid composition of each part. SANS measurements were performed on NG7 30 m SANS at the NIST Center for Neutron Research (NCNR) at the National Institute of Standards and Technology (NIST) (Gaithersburg, MD, USA), QUOKKA at the Australian Nuclear Science and Technology Organisation (ANSTO) (Lucas Heights, NSW, Australia) and SANS2D at the ISIS Neutron and Muon Source (STFC Rutherford Appleton Laboratory, Didcot, UK).

### 2.1.2 Neutron spin echo spectroscopy (NSE)

Neutron spin echo spectroscopy is an inelastic neutron scattering technique, which can be used to measure the collective dynamics of systems occurring

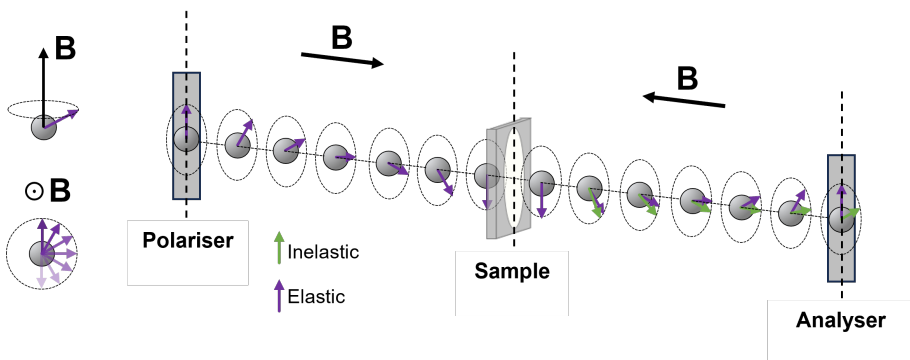


**Figure 2.5** Illustration of how the spin of a neutron is used to measure changes in energy after scattering.

over the nanosecond to hundreds of nanoseconds time scale with a similar length scale to SANS. It is most commonly used to study the dynamics of polymers, glasses and lipid membranes<sup>74</sup>.

NSE works by using the change in neutron spin polarisation to measure the change in energy of the neutron after it is scattered by the sample. The neutron beam is first polarised, so that the neutron spins are all in the same direction. A magnetic field is then applied at  $90^\circ$  to the spin direction, causing the neutron to undergo Larmor precession. The neutron beam is then scattered by the sample, either elastically so that the neutron energy is the same as before scattering, or inelastically, therefore the neutron gains or loses energy. After the sample, a magnetic field is applied which is identical to that before the sample except the field direction is flipped by  $180^\circ$ . This will cause the neutron spins to precess in the opposite direction. If the neutron was scattered elastically, the spin will precess back to its starting point, whereas, if the neutron gained or lost energy, its polarisation will be different from its starting orientation. This change in polarisation is then measured as a change in neutron energy<sup>74</sup>.

NSE measures the intermediate structure factor (ISF,  $I(q,t)$ ), which is the Fourier transform of the dynamic structure factor  $S(q,\omega)$  and can be fitted with a decay function to derive characteristic relaxation times of the motion.

In Paper II, the dynamics of the sponge phase with encapsulated protein were characterised by NSE on the NGA NSE spectrometer at the NIST Center for Neutron Research (NCNR) at the National Institute of Standards and Technology (NIST) (Gaithersburg, MD, USA). The data was fitted using a modified Zilman-Granek model over a suitable  $q$  range to describe

membrane undulation and calculate the bending rigidity of the membrane.

### 2.1.3 Dynamic light scattering (DLS)

Dynamic light scattering can be used to measure the size distribution of particles.

During the measurement, a laser is directed through the sample and elastically scattered by the particles as a function of their size and shape (here the contrast is refractive index). As the particles undergo Brownian motion, the intensity of the scattered light fluctuates. These intensity fluctuations are recorded and plotted against time. As the size of the particles affects the speed of fluctuations, the decay rate of the autocorrelation function (i.e. the correlation of the scattering data at time  $t = 0$  and after a time lag) can be fitted and used to determine the particle diffusion constant  $D$ <sup>75</sup>. The autocorrelation function is typically fit using either 'cumulant analysis' or CONTIN method, which uses the Laplace transform<sup>75</sup>. In cumulant analysis<sup>76</sup>, it is assumed that the size distribution is monomodal and is used to calculate the polydispersity index (PDI). CONTIN<sup>77,78</sup>, however, does not assume a monomodal sized distribution.

The hydrodynamic radius ( $R_h$ ) of the particles can then be calculated using the Stokes-Einstein equation:

$$D = \frac{k_b T}{6\pi\eta R_h} \quad (2.6)$$

where  $k_b$  is the Boltzmann constant ( $1.380 \times 10^{-23} \text{kg m}^2 \text{s}^{-2} \text{K}^{-1}$ ),  $T$  is the temperature (K) and  $\eta$  is the solvent viscosity ( $\text{m}^2 \text{s}^{-1}$ )<sup>75</sup>. The hydrodynamic size of the particle is defined as 'the size of the corresponding sphere that diffuses at the same rate as the particles in the sample' and includes the solvent shell around the particles, which is affected by the charge of the particle, the ions in solution and anything adsorbed to the surface.

DLS was used in Papers I, III, V, VI to determine the size distribution of lipid nanoparticle dispersions and to monitor sample aggregation.

## 2.2 Surface techniques

Up to this point, the experimental techniques have been used for bulk or dispersed systems. It can, however, be challenging to understand and

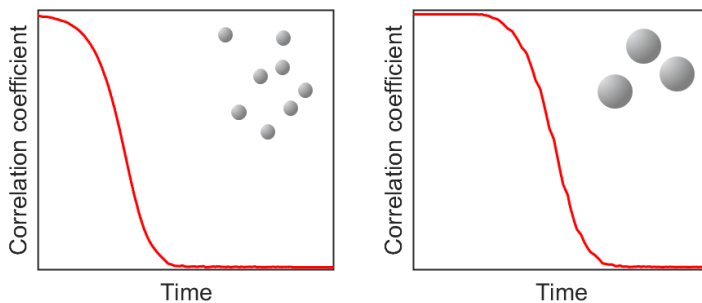


**Figure 2.6** Example correlation functions from a DLS measurement of small (left) and large (right) particles.

quantify interactions between the lipids and added biomolecules (proteins and NAs) in such samples. Using a supported lipid layer to investigate the interactions allowed us to reduce the complexity of the system and focus in more detail on the changes induced by biomolecule adsorption.

### 2.2.1 Neutron reflectometry (NR)

In specular neutron reflectometry, the reflection of the neutron beam from a surface is measured as a function of  $q$ , which provides information on the structure of the sample in the direction perpendicular to the surface<sup>79</sup>.

A neutron beam, which is highly collimated in the  $z$  direction, passes through the substrate, is incident at a low angle on the sample and is reflected off the interface at the same angle. The neutron beam will be reflected from any interface in the sample, i.e. where there is sufficient difference in SLD between two layers, therefore NR can be used to interrogate buried layers in a sample<sup>80,81</sup>. The detector measures the intensity of the reflected neutron beam and from that the reflectivity,  $R$ , can be calculated<sup>79</sup>.

NR data is most commonly modelled using Abeles matrix method<sup>82</sup> for a stratified interface, which splits the sample into a series of slabs described by an SLD, volume fraction of solvent, thickness and roughness. For example, a lipid bilayer can be described with three slabs (Figure 2.7); inner head groups, hydrophobic tail region and outer head groups, as the SLD of the head groups (e.g. PC head  $\approx 1.9 \times 10^{-6} \text{ \AA}^{-2}$ ) is higher than the tail SLD ( $\leq -0.1 \times 10^{-6} \text{ \AA}^{-2}$ ) for most common lipids.

As with SANS and NSE, changing the deuteration of the system can provide

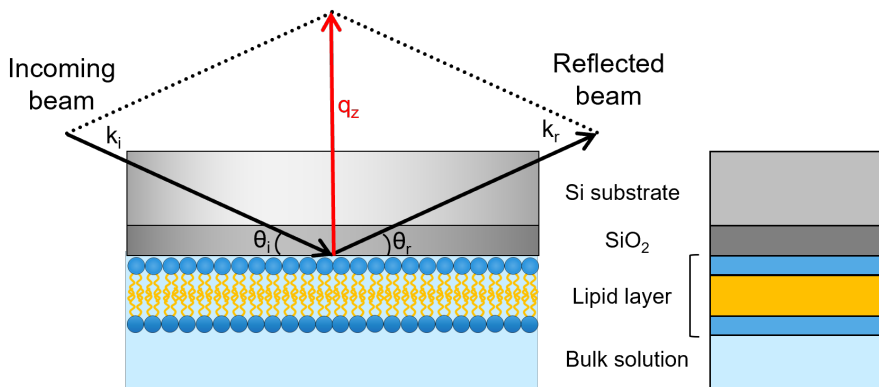


**Figure 2.7** Illustration of a typical neutron reflectometry experiment on a silicon substrate with a lipid bilayer (left) compared to a slab model which can be used to fit the data (right). For specular reflection,  $\theta_i = \theta_r$

extra information. For NR measurements, multiple solution contrasts are usually used (i.e. the isotopic contrast of the bulk solution is changed)<sup>79</sup>.

In Paper IV, the structure of a supported lipid layer containing MC3 and DOPC was investigated in different pHs before and after interaction with different NAs. For each step of the experiment (bare substrate, deposited lipid layer, after incubation with NA), the sample was characterised in at least three isotropic contrasts: buffer prepared with D<sub>2</sub>O, H<sub>2</sub>O and water contrast matched to silicon (38 % D<sub>2</sub>O/62 % H<sub>2</sub>O). These NR measurements were performed on POLREF at the ISIS Neutron and Muon Source (STFC Rutherford Appleton Laboratory, Didcot, UK) and D17 at the Institut Laue-Langevin (Grenoble, France).

### 2.2.2 Quartz crystal microbalance with dissipation (QCM-D)

Quartz crystal microbalance with dissipation monitoring (QCM-D) is a surface technique, which can be used to characterise the mass of an adsorbed layer, including interfacial and trapped water. QCM-D works using a quartz crystal as a sensor, which can be induced to oscillate in an alternating electric field (Figure 2.8a). The natural resonant frequency of the crystal (Figure 2.8b) and its (odd) overtones, can be used to characterise layers adsorbed to the crystal surface. Adding mass to the crystal surface will result in a decrease in the resonant frequency ( $\Delta f < 0$ , Figure 2.8c),

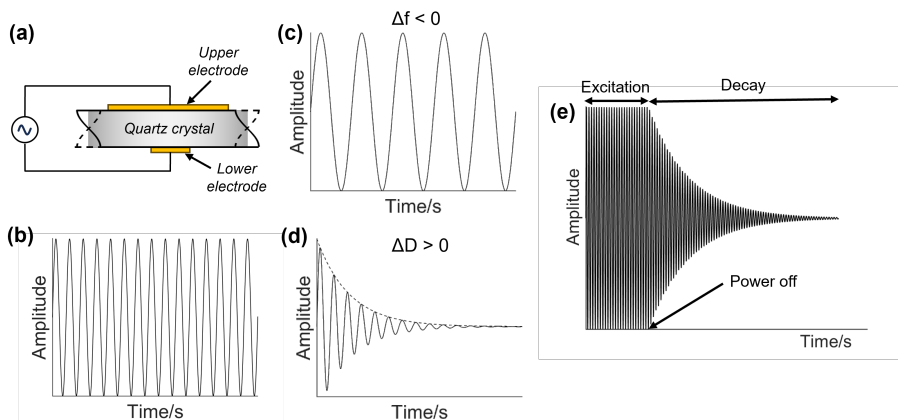


**Figure 2.8** Illustration of the effect on the (b) natural resonance of the quartz crystal if (c) mass is added to the surface causing a decrease in frequency or (d) a viscoelastic layer is added causing an increase in dissipation. (e) shows how the dissipation is measured by first exciting the crystal to resonance, then switching off the power and following the decay.

whereas an increase in frequency ( $\Delta f > 0$ ) generally indicates that the mass of the crystal has decreased, therefore that something has desorbed from the surface.

Another vital aspect of the film can be characterised using dissipation monitoring. As the crystal undergoes frictional or viscous losses in the film and to the environment, its oscillation will be damped (Figure 2.8d,e). Dissipation can be used to understand how rigid the layer is. A high dissipation indicates that the adsorbed entities are not rigid and/or couple to the surrounding solution, giving the formed layer viscoelastic properties (e.g. intact vesicles). A low dissipation indicates the adsorption of a rigid layer (e.g. lipid bilayer). It should be noted that  $\Delta f$  and  $\Delta D$  are changes relative to the baseline, therefore if the environment changes (e.g. liquid to air, density of liquid, temperature), this will also affect these values<sup>53</sup>.

For a rigid, uniformly adsorbed film with low  $\Delta D$  ( $\Delta D < 10^{-6}$ , no/low overtone spreading) and small mass relative to the mass of the crystal, the relationship between  $\Delta f$  and change in mass ( $\Delta m$ ) is linear and can be described by the Sauerbrey equation<sup>83</sup>:

$$\Delta m = \frac{C\Delta f}{n} \quad (2.7)$$

where  $\Delta m$  is adsorbed mass per area ( $\text{ng}/\text{cm}^2$ ),  $C$  is the crystal constant ( $-17.7 \text{ ng Hz}^{-1} \text{ cm}^{-2}$  for a 5 MHz crystal that is used here),  $n$  is the overtone number,  $\Delta f$  is the change in frequency (Hz). For films with higher

dissipation, this linear relationship breaks down and, in liquid, the Sauerbrey equation will tend to underestimate the adsorbed mass. Instead, more complex models considering the viscoelastic nature of the film must be employed, such as the Voigt model.

In Paper IV, the adsorbed mass of the lipid layer before and after addition of different mRNAs was measured for the DOPC/MC3 model system in a range of pHs.

## 2.3 Cryogenic transmission electron microscopy (cryoTEM)

CryoTEM is a microscopy technique that allows high resolution imaging of nanometre scale samples in their solution state.

The sample is prepared for imaging by pipetting a small volume (few  $\mu\text{L}$ ) of sample in solution onto a holey carbon grid, shortly blotting the sample from the other side of the grid and rapidly freezing by plunging the grid into liquid ethane ( $-183^\circ\text{C}$ ). Such rapid freezing prevents formation of ice crystals, trapping the sample in a thin, glassy ice layer, ideally with a thickness of 50 to hundreds of nm<sup>84-86</sup>. The sample is then imaged using a highly focussed beam of electrons ( $\lambda \approx 0.02 \text{ \AA}$  at 300kV), with sample electron density providing the contrast, while the temperature is maintained at  $\approx -175^\circ\text{C}$  with liquid nitrogen or helium<sup>84,85</sup>.

CryoTEM is incredibly useful to study particle morphology, especially as a complement to SAS data. It provides a useful guide for the choice of SAS model, shows local structural details and inhomogeneities which would not be visible in SAS data and it is possible to see different populations of which SAS would provide an average. On the other hand, as cryoTEM images typically show individual particles, they are rarely representative of the whole sample, especially if the sample is heterogeneous. This is exacerbated by the preparation artefacts inherent to the technique, such as shear from the blotting process causing distortion of particles and compression of particles larger than the ice thickness<sup>84</sup>.

CryoTEM was used in Papers I, III, V and VI to study the particle morphology. In Paper III, it was used to discuss the ambiguity in the SAXS data for a sample with mixed populations of vesicles and L<sub>3</sub>NPs. In Papers V and VI, cryoEM images of LNPs containing different cargos informed the



choice of model for fitting of SANS data and were used to inform the discussion of the internal structure of the LNPs and the different populations present in the aggregated LNP samples with polyU.

## 2.4 Ultraviolet-Visible spectroscopy (UV-Vis)

Activity tests for encapsulated  $\beta$ -galactosidase were used as a proxy to determine the effect of encapsulation on the kinetics and thermal stability of the enzyme. As previously described in Section 1.2.1, the activity of  $\beta$ -galactosidase can be measured spectrophotometrically by following the hydrolysis of the synthetic substrate *o*-nitrophenyl- $\beta$ -D-galactoside (ONPG), which is colourless, into D-galactose and *o*-nitrophenol (ONP), which is yellow ( $\lambda = 420$  nm)<sup>47</sup>. The change in concentration of ONP in the solution can be detected by following the absorption of light at 420 nm using a ultraviolet-visible (UV-Vis) spectrophotometer. The change in absorption could be converted to a concentration using the Beer-Lambert Law<sup>87</sup> and used to calculate the  $\beta$ -galactosidase activity, expressed as Neutral Lactase Units per g (NLU/g).

This activity test was used in Paper I to study the effect of encapsulation on  $\beta$ -galactosidase and its kinetic characteristics, as compared to the free enzyme and the commercial enzyme product Ha-Lactase 5200.

## 2.5 Fluorescence

Fluorescence based encapsulation efficiency (EE) assays were performed for LNPs containing NA to ensure that sufficiently high NA encapsulation was achieved during formulation. In general, the binding of a fluorescent dye to the LNP with and without the presence of Triton X-100, a surfactant which destroys the LNP structure, was compared to a standard curve and used to calculate the encapsulation efficiency of the LNP<sup>88</sup>. Two NA binding fluorescent dyes were compared; Ribogreen, which binds to polymeric NAs, and Picogreen, which binds specifically to dsDNA<sup>89,90</sup>.

The Ribogreen EE assay was used to determine the encapsulation efficiency of LNPs with different NA cargos in Paper V and the results from the Ribogreen and Picogreen EE assays were compared in Paper VI to estimate the extent of base pairing of DNA inside LNPs.

# 3

## Results

*"Started making it... Had a breakdown... Bon appetit!"*  
*-James Acaster, The Great British Bake Off*

In this chapter we will discuss the results summarised in the 6 papers included in this thesis. The discussion can be divided in 2 parts. In section 1, we discuss results regarding the sponge phase system and interactions with proteins with respect to structure and dynamics. In section 2, we discuss results regarding the interaction between the ionisable lipid DLin-MC3-DMA with different nucleic acids in both a model system and a pharmaceutically relevant lipid formulation.

### 3.1 System 1: Sponge phase ( $L_3$ ) for protein encapsulation

The lipid sponge,  $L_3$ , phase composed of GMO-50/DGMO/P80 has previously been proposed as an encapsulation matrix for large biomolecules relevant to the food industry due to its large water channel size, structural flexibility and food-safe components<sup>9</sup>. The aim of this section of the thesis was to characterise the effect of encapsulation on the stability and function of four proteins with applications in the food industry. It is well-known, however, that LLCs are very sensitive to additives, therefore the effect of the added proteins on the structure and dynamics of the lipid phase were studied. The effect of beta-galactosidase (Paper I), myoglobin (Paper III) and BvPgb 1.2 (Paper III) on the structure of the  $L_3$  phase was studied in bulk and dispersions. In Paper I, the thermal stability and kinetic characteristics of free and encapsulated  $\beta$ -galactosidase were compared, in order to determine the effect of encapsulation on the enzyme function. In Paper II, the effect of encapsulated  $\beta$ -galactosidase and aspartic protease on the dynamics of  $L_3$  phase were investigated.

Although the phase behaviour of the GMO-50/DGMO/P80 system has been well-studied with water in bulk and dispersions<sup>9,22</sup>, the choice of pH and buffer was shown to be important in the protein encapsulation studies. The effect of buffer and pH on the structure of the  $L_3$  phase in bulk and dispersions, was therefore systematically investigated and the preliminary results are presented here.

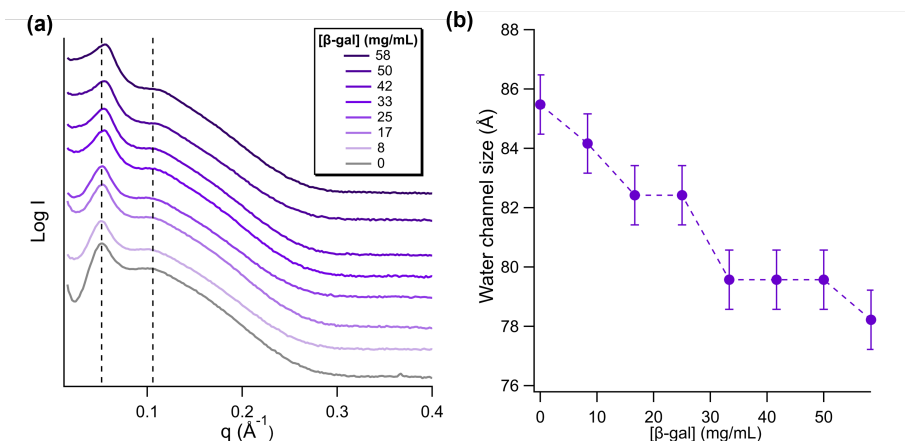


**Figure 3.1** SAXS of bulk phases with varying concentrations of  $\beta$ -gal (a, the data are offset for clarity) and the calculated change in water channel diameter with concentration of  $\beta$ -gal (b).

### 3.1.1 Enzymes: $\beta$ -galactosidase and aspartic protease

#### Bulk structure

A stock  $\beta$ -galactosidase solution was prepared by dialysis of the commercial product Ha-Lactase 5200 against 50 mM phosphate buffer pH 7.2, in order to remove the glycerol as glycerol has been shown to induce structural changes of the LLC phase<sup>24</sup>. After concentration of the dialysed protein via centrifugation, a concentration series of  $\beta$ -galactosidase solutions were prepared via dilution with the same buffer.

Bulk phases with a lipid composition of DGM0/GMO-50/P80 28/42/30 (by mass) and varying concentrations of  $\beta$ -galactosidase were prepared and measured with SAXS (Figure 3.1(a)). For the full concentration range, the characteristic broad peaks of the  $L_3$  phase are present, although both peaks also shift to higher  $q$  with increasing concentration. The water channel size, estimated by comparison to the preceding cubic phase in the dilution series, decreases with increasing protein concentration (Figure 3.1(b)). Considering its size, the protein is likely partially in the water channel and the bilayer, thereby dehydrating the head groups.

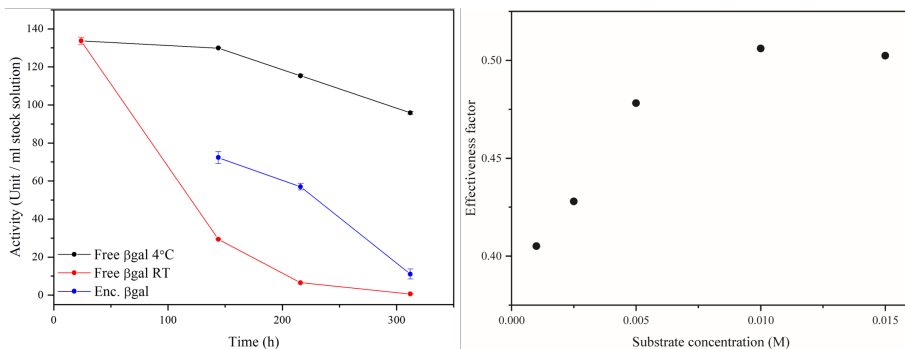


**Figure 3.2** (Left) Activity change over time of free  $\beta$ -gal at 4 °C (black) and RT (red) and encapsulated  $\beta$ -gal (blue) measured using 15 mM ONPG at 24 °C and absorbance measured at 420 nm. The results were normalised to Ha-lactase activity and a concentration of 1 mg/ml. (Right) The effectiveness factor,  $\eta$ , plotted as function of substrate concentration, where  $\eta$  is initial rate of the encapsulated  $\beta$ -gal divided by the initial rate of free  $\beta$ -gal.

## Enzyme activity and kinetics

In order to evaluate the suitability of the  $L_3$  phase as an encapsulation matrix to improve the stability of  $\beta$ -galactosidase ( $\beta$ -gal), the change in activity was compared between encapsulated  $\beta$ -gal and free  $\beta$ -gal stored at room temperature and free  $\beta$ -gal stored at 4°C over 2 weeks using the activity test described in Section 2.4 (Figure 3.2: Left). From the activity profiles, assuming first order deactivation kinetics, the rate of deactivation was estimated as  $k_{enc} = 3.4 \times 10^{-7} s^{-1}$ ,  $k_{free,4^\circ C} = 3.2 \times 10^{-7} s^{-1}$  and  $k_{free,RT} = 5.1 \times 10^{-6} s^{-1}$ . Encapsulation in  $L_3$  slowed the rate of deactivation compared to the free  $\beta$ -gal stored at the same temperature, but still decreased in activity faster than the free  $\beta$ -gal stored at 4°C. From visual inspection of the free  $\beta$ -gal stored at RT, the loss of activity appears to be associated with degree of protein aggregation, which was not observed for the encapsulated  $\beta$ -gal or the free  $\beta$ -gal stored at 4°C.

**Table 3.1** Table summarising key parameters from the Michaelis-Menten kinetic model for Ha-Lactase 5200, the free  $\beta$ -gal after dialysis and encapsulated  $\beta$ -gal.

Sample	$K_M$ (mM)	$V_{max}$ ( $\Delta A/min$ )
Ha-Lactase 5200	$1.9 \pm 0.1$	$0.244 \pm 0.006$
Free $\beta$ -gal (4°C)	$1.9 \pm 0.1$	$0.193 \pm 0.003$
$L_3$ + $\beta$ -gal	$2.9 \pm 0.1$	$0.104 \pm 0.002$

The kinetic characteristics of Ha-Lactase 5200, free  $\beta$ -gal after dialysis and encapsulated  $\beta$ -gal were evaluated according to the Michaelis–Menten kin-

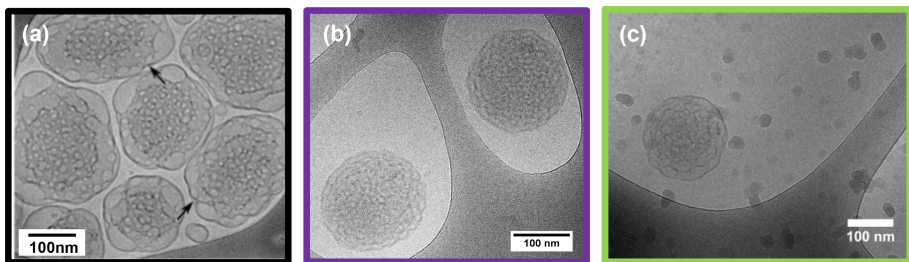


**Figure 3.3** CryoTEM images of (a) empty L<sub>3</sub>NPs (reproduced from<sup>9</sup>), (b) L<sub>3</sub>NPs containing  $\beta$ -gal and (c) L<sub>3</sub>NPs containing aspartic protease.

etic model<sup>91</sup>. The key parameters are  $V_{\max}$ , the maximum rate, and  $K_M$ , the concentration of substrate at which  $\frac{1}{2} V_{\max}$  is achieved and indicates enzyme-substrate affinity. The lower  $V_{\max}$  and higher  $K_M$  of the encapsulated  $\beta$ -gal are likely a combination of (i) diffusion limitations, as shown by the plateau at higher concentration of the effectiveness factor (Figure 3.2: Right), and (ii) limited access to the active site/damage to the  $\beta$ -gal due to the encapsulation. This is discussed in more detail in Paper I.

## Dispersions

The bulk phases containing encapsulated  $\beta$ -gal were dispersed into Milli Q and formed nanoparticles, which retained the internal sponge phase structure and had a well-defined size distribution. Notably, inclusion of  $\beta$ -gal appears to increase the homogeneity across the particle, as the highly swollen surface layer visible in the empty L<sub>3</sub>NPs (Figure 3.3(a)) is not present with the encapsulated  $\beta$ -gal (Figure 3.3(b)). The same effect can be observed to a lesser extent for L<sub>3</sub>NPs containing aspartic protease, prepared in an analogous manner.

The mean hydrodynamic size and PDI of the dispersions were similar for the L<sub>3</sub>NPs containing no enzyme (empty)<sup>9,25</sup>, aspartic protease<sup>24</sup> and  $\beta$ -gal, although a lower PDI was observed in the case of both enzymes (Table 3.2).

**Table 3.2** Table summarising DLS results for L<sub>3</sub>NPs containing no enzyme (empty), aspartic protease and  $\beta$ -gal.

Sample	< Z > diameter/nm	PDI
Empty L <sub>3</sub> NPs	152 $\pm$ 12	0.17 $\pm$ 0.04
L <sub>3</sub> NPs + $\beta$ -gal	163 $\pm$ 1	0.10 $\pm$ 0.01
L <sub>3</sub> NPs + asp	155 $\pm$ 1	0.12 $\pm$ 0.03

## Dynamics

In order to understand the effect of encapsulating  $\beta$ -gal and aspartic protease (asp) on the dynamics of the lipid membrane, NSE measurements were carried out for empty  $L_3$ NPs,  $L_3$ NPs containing a high and low concentration of  $\beta$ -gal and  $L_3$ NPs containing a high and low concentration of asp.

As discussed in Section 1.1.2, the lipid bilayer undergoes different motions simultaneously and the dominant motion depends strongly on the length and time scale measured. Considering previous SANS measurements of the empty  $L_3$ NPs<sup>22</sup> and SAXS measurements of the bulk phase<sup>24,25</sup>, the NSE data was divided into three  $q$  ranges (indicated in Figure 3.4(a,b) by the vertical dashed lines); (i) low  $q$  ( $q \leq 0.07 \text{ \AA}^{-1}$ ), where topological membrane changes dominate, (ii) intermediate  $q$  ( $0.07 \text{ \AA}^{-1} \leq q \leq 0.13 \text{ \AA}^{-1}$ ), the Zilman-Granek (Z-G) model range where membrane undulations dominate, and (iii) high  $q$  ( $q > 0.13 \text{ \AA}^{-1}$ ), where bilayer thickness fluctuations dominate. For all  $q$  ranges (Figure 3.4(a,b)), a decrease in dynamics was observed with increasing protein concentration, with a larger effect for  $\beta$ -gal than asp.

A modified version of the Z-G model including diffusion (for the full description, see Paper II) was fit to the data in the intermediate  $q$  range (Figure 3.4(c,d)), in order to calculate the membrane bending modulus,  $\kappa$  for each sample. The relative membrane bending moduli  $\kappa_{\text{rel}}$  were calculated by normalising the  $\kappa$  extracted from the fit to the bending modulus for the empty sponge phase ( $\kappa_{\text{empty}} = 10.8 \pm 0.3 k_B T$ ) and are shown plotted against the final enzyme concentration in the  $L_3$ NPs in Figure 3.4(e). For both proteins, the membrane bending modulus increased (i.e. the membrane became stiffer) with increasing [protein], with a larger effect for  $\beta$ -gal than asp.

This trend can be discussed in terms of the interactions between the  $L_3$  lipid membrane and the different proteins and the structural changes they induce. Aspartic protease has been shown with NR and Raman spectroscopy<sup>23,24</sup> to penetrate into the hydrophobic region of the bilayer and dehydrate the lipid groups. This eventually triggered the transition from the  $L_3$  to  $Pn3m$  cubic phase, which has a more ordered structure with less mobile acyl chains. Similar NR measurements have shown that  $\beta$ -galactosidase can also spontaneously penetrate into lipid bilayer, but causes large structural rearrangement and thickening of the layer<sup>23</sup>. The SAXS data in Figure 3.1 shows that increasing [ $\beta$ -gal] results in a decrease in unit cell size,

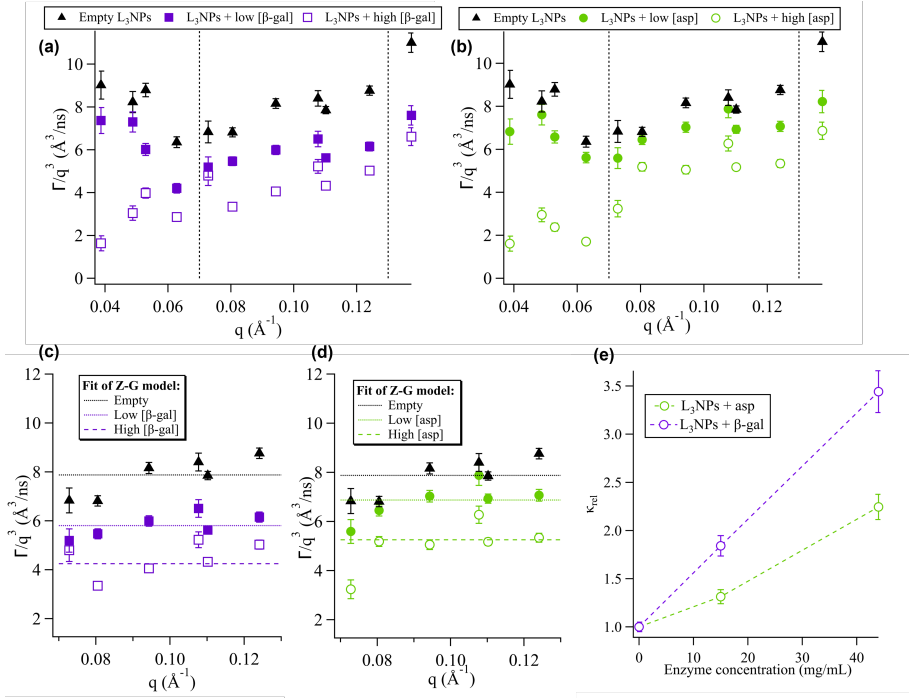


**Figure 3.4** Summary of the results from NSE measurements of L<sub>3</sub>NPs with (a) β-gal and (b) asp. The fit of Z-G model to the intermediate  $q$  range of NSE data for L<sub>3</sub>NPs with (c) β-gal and (d) asp was used to calculate the relative membrane bending modulus (e).

most likely due to head group dehydration, but no phase transition. The activity test data, measured with a water soluble substrate, shows that the active site is exposed to the water channel, therefore there is a part of the β-gal present in the water channel, which would act to limit the available volume in the channel free for the membrane bending motion. Considering its larger size in combination with the membrane perturbation and thickening and head group dehydration, it is unsurprising that β-gal has a larger effect on the membrane rigidity.



### 3.1.2 Haeme-containing proteins: BvPgb and Mb

#### Bulk structure

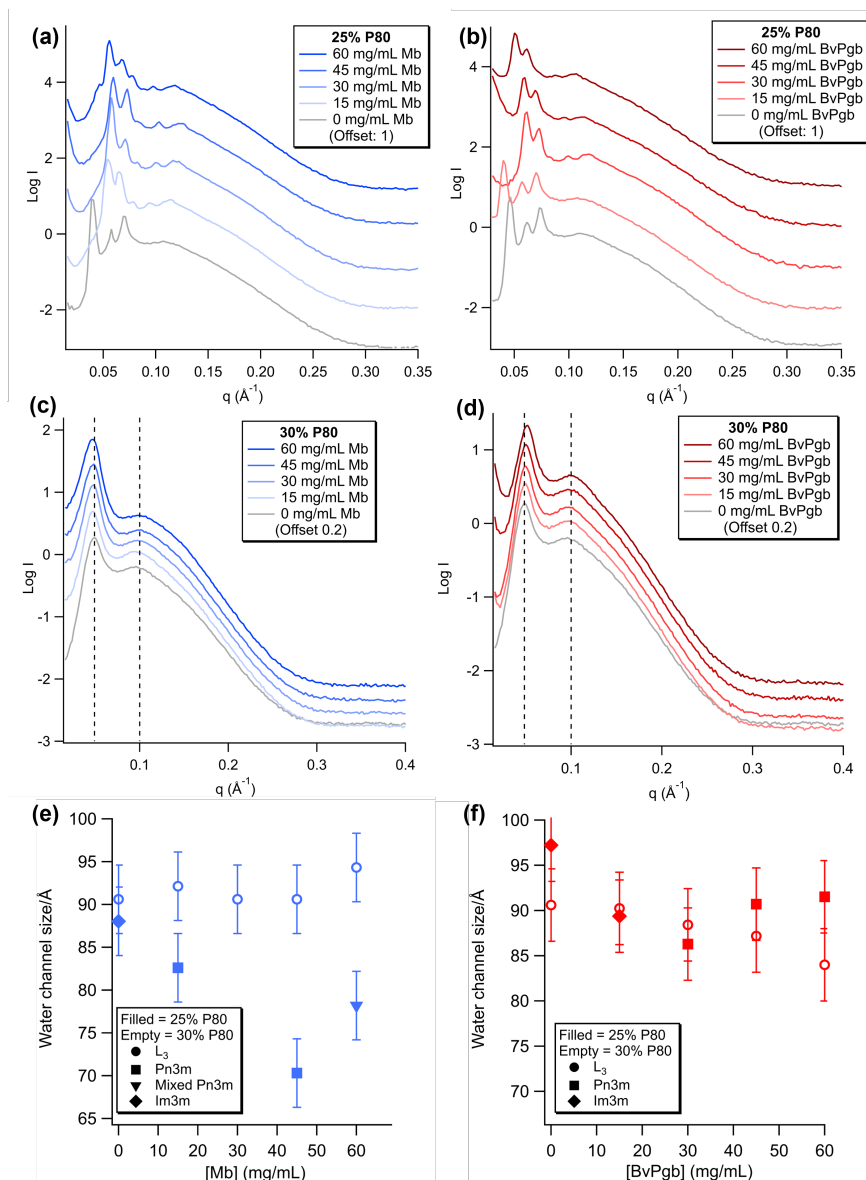


**Figure 3.5** SAXS of bulk phases with varying concentrations of Mb (a,c) and BvPgb1.2 (b,d) and % P80. The data are offset for clarity. Change in water channel diameter with concentration of Mb (e) and BvPgb (f). The filled symbols refer to the lipid composition with 25 % P80 and the empty symbols with 30 %P80. The symbols refer to the following structures: sponge phase,  $L_3$  (circle), Pn3m cubic (square), mixed phase including Pn3m cubic (inverted triangle) and Im3m cubic (diamond).

A stock myoglobin (Mb) solution was prepared from a commercially available freeze dried powder and a stock phytoalbumin BvPgb 1.2 (BvPgb) solution was prepared by expression in *E. coli* and purification as summarised in Paper III. Both stock solutions were prepared in 50 mM Tris-HCl buffer pH 8.5 and the same buffer was used to dilute them to the concentrations used to prepare the bulk phase samples.

Two lipid compositions were investigated for both proteins in which the DGM0/GMO-50 ratio was kept constant at 40/60 and the ratio of P80 was varied: DGM0/GMO-50/P80 28/42/30 (30 % P80, as for the  $\beta$ -gal samples) and 30/45/25 (25 % P80). Bulk phase samples with a range of Mb and BvPgb concentrations were prepared and measured with SAXS (Figure 3.5(a-d)). For both 25 % P80 series (Figure 3.5(a,b)), the bulk phase transitioned from Im3m to Pn3m cubic phase with increasing protein concentration, which is associated with a decrease in hydration. For Mb, the calculated water channel diameter decreased in size, whereas for BvPgb, it remained constant over the whole concentration range (Figure 3.5(e)). For both 30 % P80 series (Figure 3.5(c,d)), the L<sub>3</sub> was observed for all samples with almost no change in water channel diameter for either protein (Figure 3.5(f)). In the SAXS curves for 30 % P80 series with BvPgb (Figure 3.5(d)), a concentration dependent low q upturn was observed, indicating possible BvPgb aggregation. For the highest [BvPgb], reversible gravity induced phase separation into a protein rich and protein poor phase was observed.

## Dispersions

The bulk phases containing Mb and BvPgb were dispersed into Milli Q, however in all cases, the resulting dispersion had a very high PDI and the size distribution from DLS was multimodal.

Broad peaks in the SAXS data were observed for all samples (Figure 3.6), although the peak was flatter and broader for both 30 % P80 series (Figure 3.6(c,d)). For the BvPgb samples, a low q [BvPgb] dependent upturn indicating aggregation was observed for both %P80 (Figure 3.6(b,d)), with visible red-orange aggregates for the 25 % P80 series. For Mb, however, a low q [Mb] independent upturn was only observed for the 25 % P80 series (Figure 3.6(a)). The bilayer form factor peak tends to dominate the SAXS curves for L<sub>3</sub>NPs, as the cell-cell correlation peak becomes weaker due to the limited size of the particles and surface effects of the particle

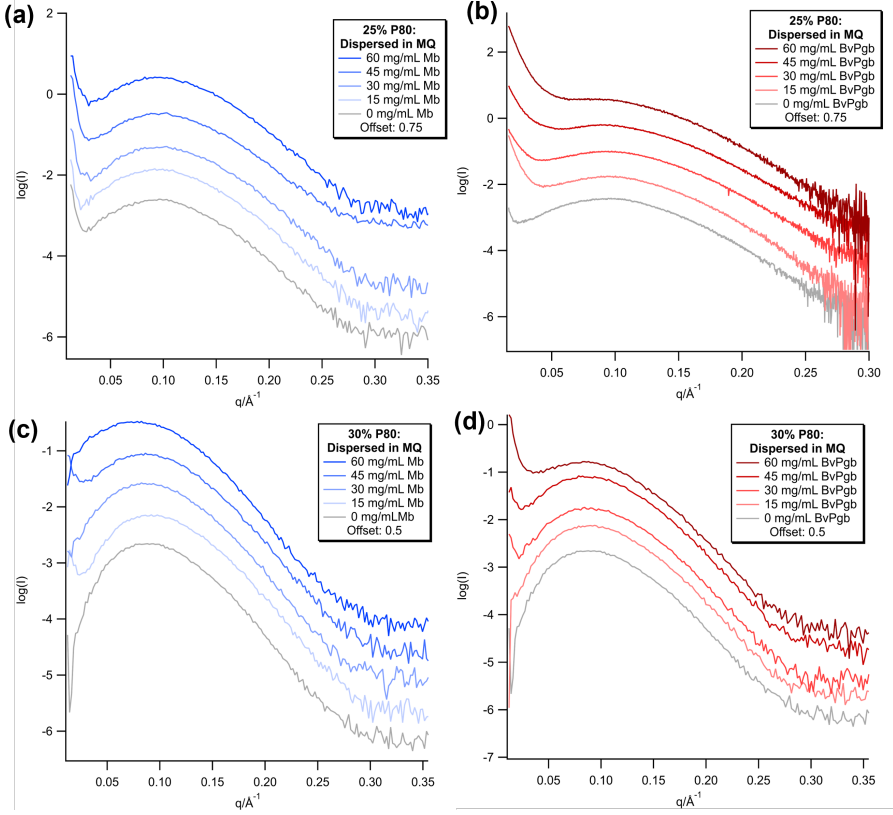


**Figure 3.6** SAXS of dispersions in MQ with varying concentrations (0–60 mg/mL) of Mb (a,c) and BvPgb (b,d). The data are offset for clarity.

morphology. As the bilayer form factor peak is present in both the SAXS pattern of L<sub>3</sub>NPs and unilamellar vesicles, it is difficult to determine the relative proportions of the populations. In cryoTEM images of the 30 % P80 samples containing 60 mg/mL of BvPgb (Figure 3.7: left) and Mb (Figure 3.7: right), there is a large vesicle population present. It should be noted, however, that high shear during the blotting can cause a transition from L<sub>3</sub>NPs to vesicles.

In the 25 % P80 dispersions, aggregation of the proteins is apparent from the low  $q$  upturn observed with the Mb samples (Figure 3.6(a)) and the visible aggregates observed in the BvPgb samples. As the stability of proteins is highly dependent on the environment, multiple factors could affect the stability of the encapsulated protein, including the protein-lipid interactions and the solution conditions. As the dispersing solvent easily diffuses in and out of the water channels in the bicontinuous phases, the overall con-

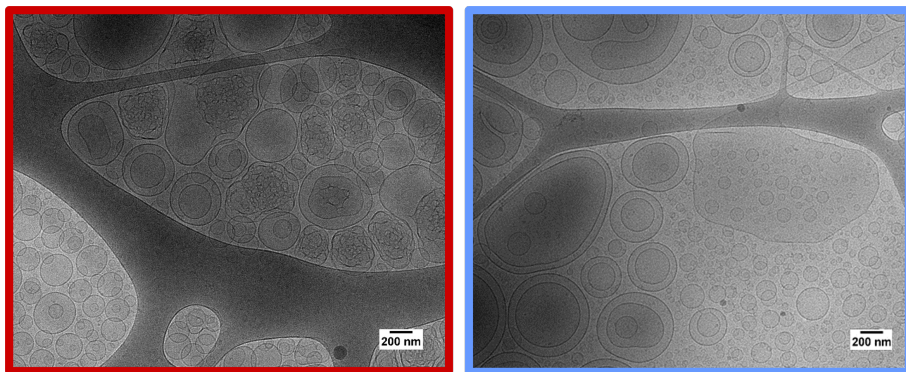


**Figure 3.7** CryoTEM images for 30 % P80 with 60 mg/mL BvPgb (left), which show the presence of vesicles in coexistence with the sponge phase particles and for 30 % P80 with 60 mg/mL Mb (right), which show a mixture of large and small vesicles.

centration of Tris-HCl buffer in the system will decrease and the buffering effect of the Tris-HCl buffer in the bulk systems is affected by the large area of lipid-aqueous interface. Due to the lower buffering capacity and that the “local pH” close to the lipid interfaces in the particles can be different to the “bulk pH”, the apparent pH experienced by the encapsulated Mb and BvPgb could be close to or below their isoelectric points, pI, which could contribute to their aggregation.

In order to test this effect, an additional Mb dispersion series with 25 % P80 was prepared. The bulk phases were prepared with a series of Mb concentrations in 50 mM Tris-HCl buffer pH 8.5 as before, but the dispersions were prepared using the same buffer (instead of Milli Q) as the dispersing solvent. The low  $q$  [Mb] independent upturn, indicating possible aggregation, was no longer observed in the SAXS data for the dispersions in Tris-HCl. In the DLS correlation curves for these dispersions, however, the growth of a shoulder at longer relaxation time and decrease in  $y$  intercept with increasing [Mb], indicates an increasing contribution from larger objects, that were likely sedimenting. This indicates that dispersion in Tris-HCl buffer instead increases the rate or extent of aggregation with Mb. One proposed biological function of Mb is in fatty acid transport and it has previously been shown that Mb can bind specifically and non-specifically to fatty acid, including strong binding to oleic acid, which is the fatty acid chain of all lipids used in this system<sup>92,93</sup>. The higher pH of the dispersing solvent could, therefore, improve the stability of the protein and thereby allow increased binding and aggregation.

Although there is a clear case for the potential effect of the buffer and

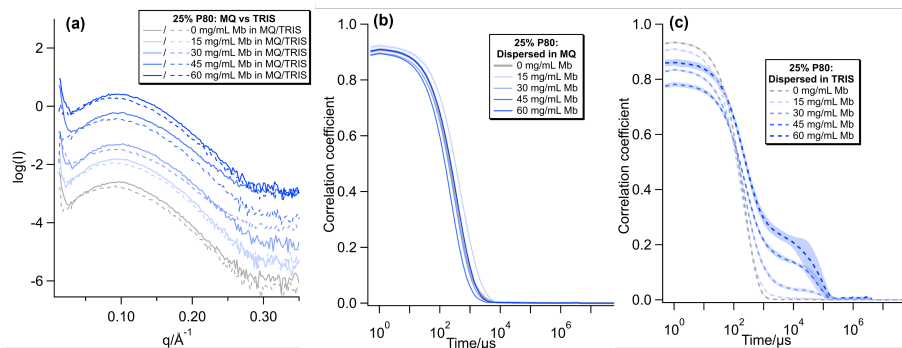


**Figure 3.8** (a) SAXS of dispersions in MQ with varying concentrations (0–60 mg/mL) of Mb dispersed in MQ (solid line) and Tris-HCl buffer (dashed line). The data are offset for clarity. DLS correlograms comparing lipid particles with 25 % P80 in MQ (b) and Tris-HCl buffer (c) for different concentrations of Mb (0–60 mg/mL).

pH on the protein, it seems that it also has an effect on the lipids. A high polydispersity of  $> 0.4$  was observed for the dispersion of bulk phase with no protein using Milli Q as the dispersing solvent, with a large vesicle population in cryoTEM images of the same sample. This was therefore investigated in more depth in the following project.

### 3.1.3 Buffer effects

Given the destabilising effect observed with the Tris buffer and higher pH when dispersing the bulk phase, the effect of buffers used in previous work with proteins encapsulated in the  $L_3$  phase was investigated over a wide pH range:

- (i) For the low pH range (pH 5–5.5), acetate buffer, which was used in the activity test for encapsulated aspartic protease<sup>24</sup>.
- (ii) For the intermediate pH range (pH 6–8), phosphate buffer, which was used in the encapsulation of and activity test for  $\beta$ -galactosidase (Paper I, II).
- (iii) For the higher pH (pH 8–9), Tris-HCl buffer, which was used in the encapsulation of myoglobin and BvPgb (Paper III).

This work is an ongoing project in collaboration with the group of Prof. Joshua Jackman (SKKU, South Korea), but preliminary results measured together with Hyeonjin Park are presented below.

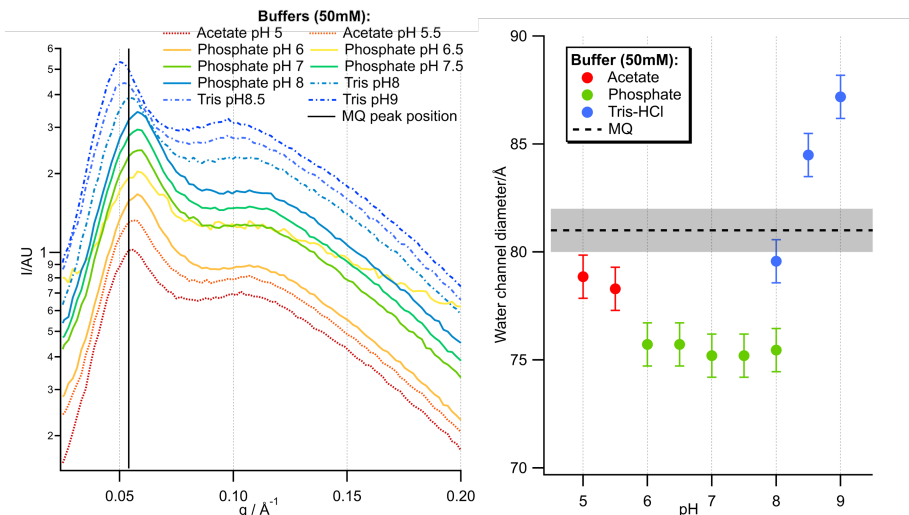


**Figure 3.9** SAXS data for bulk  $L_3$  samples prepared with different buffers over the pH range 5-9 (left), which was used to estimate the water channel diameter change with pH (right). The peak position and water channel size for the  $L_3$  bulk phase prepared with Milli Q is included for reference. The SAXS data were offset for clarity.

Bulk phase samples were prepared as previously with the different buffers range and measured using SAXS (Figure 3.9: Left). It is clear from the SAXS data that the  $L_3$  phase was formed for all the buffer conditions, however the position of the two characteristic peaks varied. To more easily visualise the effect of the buffers and pH on the position of the low  $q$  peak, corresponding to the cell-cell correlation distance, the water channel diameter estimated from the  $q$  value of this peak was plotted against pH in Figure 3.9 along with the water channel size observed with MQ as a reference point.

From this data, it is clear that both the buffer and the pH affect the  $L_3$  structure. With respect to pH; for both the acetate and phosphate buffered samples, the water channel size did not change with pH, whereas for Tris-HCl buffer samples, the water channel increased in size with increasing pH. With respect to buffer; the water channel sizes for samples prepared with pH 8 phosphate and Tris-HCl differ by  $\approx 5$  Å, demonstrating a clear specific buffer effect.

The main difference with pH occurs near the expected pKa value for long chain fatty acids near an interface (pH 8-8.5), which are expected to be present to a small degree in the sample, as trace amounts in the components and possibly as a result of glyceride hydrolysis<sup>94</sup>. With increasing pH and

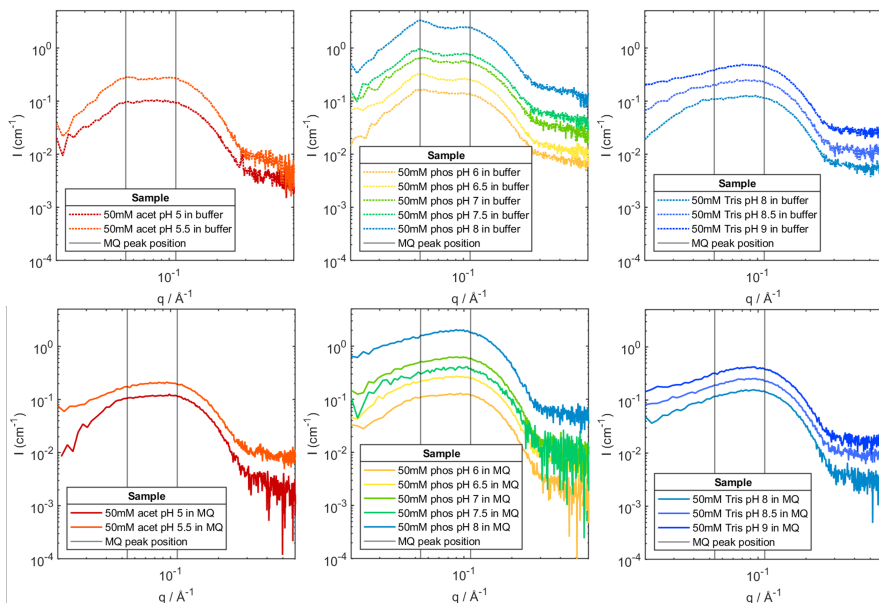


**Figure 3.10** SAXS data for bulk phases prepared with different buffers dispersed in the same buffer (top row) or Milli Q (bottom row). The black lines correspond to the peak positions for the bulk phase prepared with Milli Q and the data were offset for clarity.

decreasing protonation, oleic acid has been shown to adopt structures with lower curvature, which is in line with the increase in water channel diameter with pH observed here<sup>95,96</sup>. When considering the structure of the ions in the buffers compared to the lipid head groups, the similarity decreases as Tris>acetate>phosphate, therefore the expected interaction strength with the lipid head groups decreases in the same order.

The bulk phases were then dispersed by shaking into either Milli Q or the same buffer with which they were prepared (i.e. the bulk phase prepared with 50 mM Tris-HCL and dispersed into 50 mM Tris-HCL). The structure, size and zeta potential of the corresponding dispersions were then measured using SAXS and DLS.

In the SAXS data (Figure 3.10), the bilayer form factor was clearly present in all of the samples. The cell-cell correlation peak at  $\approx 0.05 \text{ \AA}^{-1}$ , however, was much more visible in the samples dispersed in buffer and is most clearly visible in the phosphate buffered samples for all pHs. In the dispersions in Tris buffer, there appears to be a trend in the intensity of the correlation peak with pH; it is somewhat visible as a shoulder at pH 8, but becomes less so as the pH increases to 9.

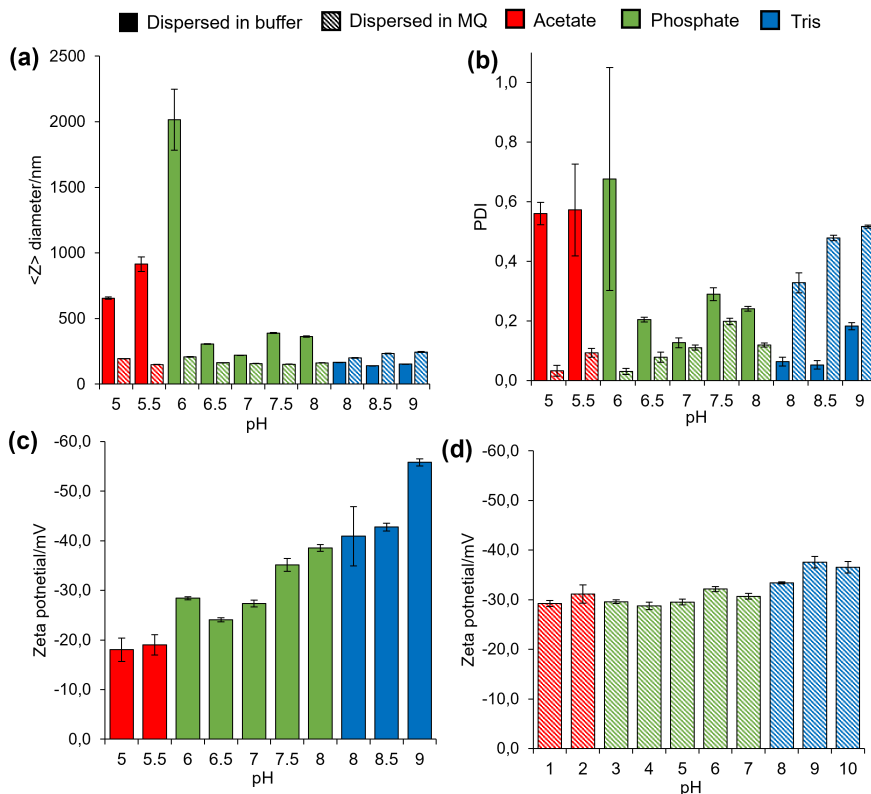


**Figure 3.11** Results from DLS measurements of dispersions of bulk phase in Milli Q and different buffers, including the  $\langle Z \rangle$  diameter (a) and PDI (b). The zeta potential measured in buffer and in Milli Q are shown in (c) and (d) respectively.

The  $\langle Z \rangle$  diameter and PDI determined from DLS measurements were plotted in Figure 3.11(a,b). Due to the high polydispersity observed for some of these samples, it is more informative to consider the PDI values for the dispersions. Generally, the phosphate buffered samples, with the exception of pH 6, seem to have similar PDI values for both dispersions in Milli Q and in buffer. For the acetate buffered samples, a much higher PDI is observed for the dispersions in buffer than Milli Q, whereas the opposite trend was observed for the Tris buffered samples.

As expected, the zeta potential of the dispersions in buffer became more negative as the pH increased (Figure 3.11(c)), whereas the zeta potential was similar for all of the dispersions in Milli Q at  $\approx -30$  mV (Figure 3.11(d)).



## 3.2 System 2: Lipid nanoparticles for nucleic acid delivery

LNP formulations containing cationic ionisable lipids (CILs) for RNA delivery have been shown to be widely successful and have had a large societal impact<sup>97</sup>. As a result, this has become a rapidly expanding field, with a large push for the optimisation of lipid formulation composition and development of new lipids and lipidoids to optimise function *in vitro/vivo* (<sup>30</sup> and refs within,<sup>31</sup> and refs within). Despite this, there remains a lack of understanding of the mechanism of action of these LNPs, their structure-function-efficacy relationship and the behaviour and interactions of the newly developed CILs.

In this section of the thesis, the aim was to understand how the NA cargo and its structure affected its interaction with the CIL MC3 in both a model system and with a benchmark LNP lipid composition. In Paper IV, we investigated a model system of a supported lipid layer composed of varying ratios of the CIL MC3 and DOPC and its interaction with different RNAs (human erythropoietin (EPO) mRNA, polyA and polyU) in a pH range covering the apparent pKa of MC3. In Papers V and VI, we have characterised the effect of type and concentration of NA (polyA, polyU, dsDNA and ssDNA) on the LNP structure, including the lipid composition of the core and shell, colloidal stability of the LNP and its internal structure. Additionally in Paper V, we have followed the structural evolution of the LNP during the initial formulation steps of microfluidic mixing and dialysis.

### 3.2.1 Model system

The model lipid layer was investigated with a range of mol% MC3 ranging from 0 - 15 %, in order to have a stable layer over the time period required for NR experiments, and over a pH range of 6-8, which includes the apparent pKa of MC3 6.44<sup>34</sup>. From QCM-D measurements of the lipid layer alone, the adsorbed mass of the layer was the same within error for all compositions and pHs studied (Figure 3.12(a)). The dissipation, however, was higher for all the MC3 containing layers than the pure DOPC layer, indicating a more viscoelastic layer, possibly due to increasing water uptake and/or disorder in the layer (Figure 3.12(b)). The highest value of dissipation was measured for 5 % MC3 and decreased with increasing proportion of MC3.

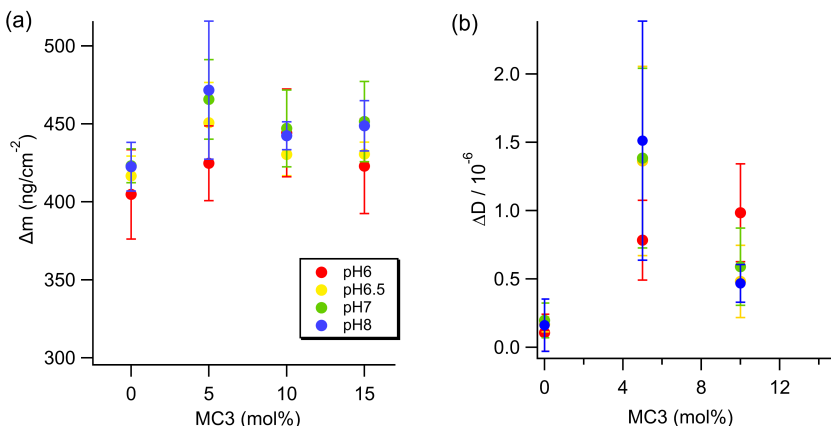


**Figure 3.12** Change in (a) adsorbed mass and (b) dissipation from QCM-D measurements for lipid layers with different MC3 content at different pHs before incubation with nucleic acid. For comparison, the adsorbed mass of a full coverage DOPC bilayer is  $\approx 420 \text{ ng/cm}^{-2}$  <sup>98</sup>.

NR data for the different lipid layers were recorded for pH 6 and 7 buffers, i.e. below and above the apparent pKa of MC3. For all lipid layers measured in acidic conditions (5, 10, and 15% MC3), the data were well-described by a bilayer model, which is consistent with simulation results for this system<sup>99,100</sup> and only very minor differences at high  $q$  are visible. For the lipid layers measured in neutral conditions (5, and 15% MC3), the fitting is more complicated, as simulation results indicate clustering of the MC3 in its neutral form in the centre of the layer at higher pH but the extent of clustering varies depending on force field used<sup>99,100</sup>. Due to the small amount of %MC3 and the similar SLDs of DOPC and MC3, it was not possible to unambiguously locate the MC3 in the layer. Multiple models were therefore compared in the data fitting for the lipid layers measured in pH 7 buffers, including the bilayer model used for the pH 6 data, a bilayer + water interlayer model, a generic 3 slab model and a generic 4 slab model. The data for the 5% MC3 layer in pH 7 was reasonably well-described by a bilayer model with similar structural parameters as in pH 6 with the exception of a higher number of water molecules per lipid head group. The data for the 15% MC3 layer in pH 7, however, was more complex. All of the models tested describe the data reasonably well with the same trends in hydration and roughness of the layer, with a small increase in hydration and a large increase in roughness. There is, however, some disagreement in all cases between the data and fits for  $0.07 \text{ \AA}^{-1} > q > 0.11 \text{ \AA}^{-1}$  in the CMSi contrast, indicating that the models do not fully describe the system.

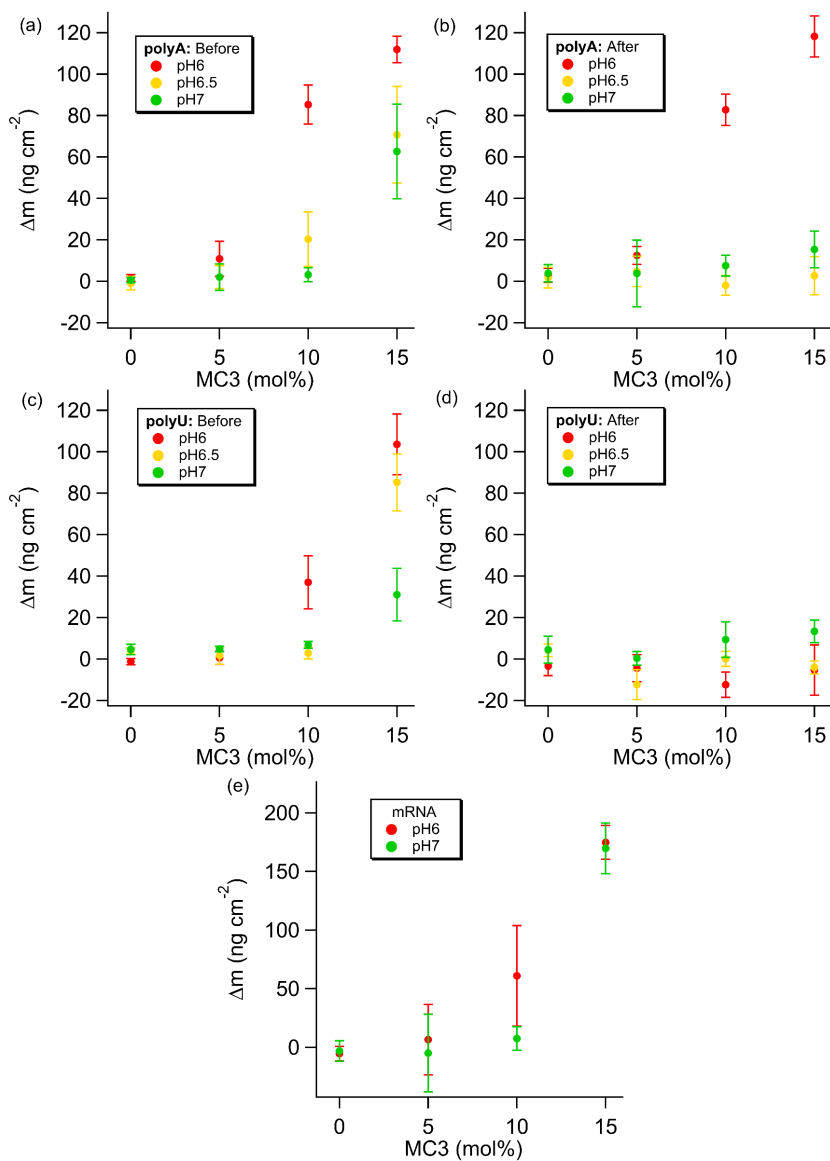





**Figure 3.13** The change in adsorbed mass before and after equilibration is shown for polyA (a, b) and polyU (c, d). For mRNA in all conditions, the adsorbed mass remained the same after equilibration (e). Change in adsorbed mass before equilibration was calculated using the difference in frequency between the lipid layer and the initial minimum after addition of the NA.

The interaction between the different NAs and the lipid layer was characterised using QCM-D measurements of the lipid layer with a range of mol%

polyA	pH				polyU	pH			EPO mRNA	pH	
	6	6.5	7	8		6	6.5	7		6	7
0% MC3					0% MC3				0% MC3		
5% MC3					5% MC3				5% MC3		
10% MC3					10% MC3				10% MC3		
15% MC3					15% MC3				15% MC3		

	Case (i)		Case (ii)		Case (iii)
---	----------	---	-----------	---	------------

**Figure 3.14** Table of QCM-D case with pH and %MC3 for polyA (red), polyU (green) and EPO mRNA (orange).

MC3 ranging from 0 - 15 % and over a pH range of pH 6 - 7 for the three types of RNA; polyA, polyU and EPO mRNA (Figure 3.13). Different adsorption behaviour with lipid composition and pH was observed for each type of RNA (Figure 3.14). Three cases were observed for the QCM-D results after addition of RNA to the equilibrated lipid layer: case (i) with no significant difference between  $\Delta f$  or  $D$  before addition of NA and after equilibration and rinsing; case (ii) where a decrease in  $\Delta f$  to a minimum and increase in  $\Delta D$  to a maximum upon addition of NA was observed, which recovered to the pre-nucleic acid values after equilibration and rinsing; and case (iii) where a decrease in  $\Delta f$  to a minimum and increase in  $\Delta D$  to a maximum upon addition of NA was observed which remained after equilibration and rinsing.

For selected lipid compositions, pHs and RNAs, NR measurements were performed after incubation of the lipid layer with RNA and rinsing, in order to provide insight into the structural changes driving the differences in adsorbed mass and rigidity observed with QCM-D (Figure 3.15). For the 5% MC3 layers in pH 6 and 7 after incubation with EPO mRNA, as expected from the QCM-D data (Figure 3.14), only minor changes were observed in the data, which could be described using a bilayer model (Figure 3.15 (a,b)). For the 10 % (pH 6) and 15 % lipid layers (pH 6 and 7) after incubation with EPO mRNA, the broad peak at  $\approx 0.082 \text{ \AA}^{-1}$  indicated the formation of a multilayer with a repeat distance of  $\approx 77 \text{ \AA}$ . This data was fitted with a mixed area model of a bilayer (with the parameters fixed from the lipid layer fit) and a repeating stack of 2 slabs. For these samples, the parameters describing the 2 slabs were similar with one less hydrated, lipid rich layer and one more hydrated, mRNA rich layer. A similar broad peak at  $\approx 0.09 \text{ \AA}^{-1}$  is visible in the data for the 15% MC3 lipid layer after incubation with polyU, which was described using the same mixed area

model with similar fit values for the slabs. The main differences were a lower slab roughness and the smaller thickness for the mRNA rich slab for polyU data, which was expected due to the higher  $q$  position of the peak (Figure 3.15).

There is some disagreement between the model and data for these samples, which is more visible in the  $H_2O$  contrast and most likely stems from fixing the bilayer fitting parameters in this model. Given the lack of interaction with NA observed for the pure DOPC layer, it is likely that the MC3 preferentially interacts with the RNA and would be enriched in or close to the multilayer domains. This would result in differences in composition, therefore most likely also structure, in the remaining bilayer regions. Due to the lack of contrast between DOPC and MC3, however, it was not possible to distinguish between the contributions from the different lipids. It should be noted that fitting with varying bilayer parameters was attempted but was not possible due to the number of highly correlated parameters.

The fitting of the 15 % MC3 (pH 6) data after incubation with polyA did not have a similar broad peak and was therefore instead fitted with a bilayer (with varying parameters) with a single slab on top. As the largest difference is in the  $H_2O$  contrast, this implies that the change is in the head group region of the layer. This can further be seen in the high roughness of the slab for this model, as the roughness is higher than the thickness of the slab. This indicates that the interface between the layers is very poorly defined and there is likely a wide distribution of polyA chain lengths and penetration depths in this 'layer'.

Comparing the cases observed in the QCM-D data in combination with NR data measured for select compositions and pHs after addition of NA (Figure 3.15), these could be interpreted as: case (i) no significant interaction between the lipid and NA; for case (ii) the RNA penetrates into the lipid layer, displacing water associated with the layer and possibly removing lipid from the layer; and for case (iii) the NA adsorbs to the surface of lipid layer possibly with some extent of penetration into it. A general trend was observed for all the RNAs, that with increasing %MC3 and decreasing pH, the behaviour changed from case (i) through case (ii) (for polyA and polyU) to case (iii) (see Figure 3.14).

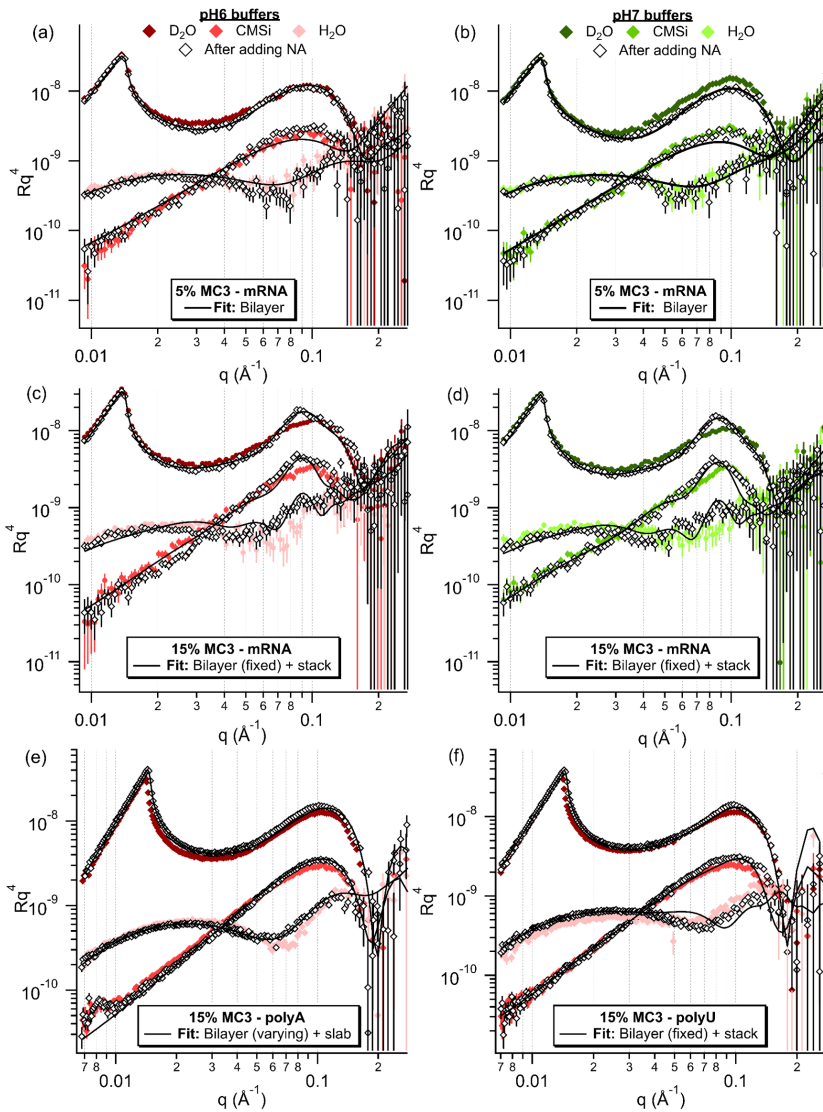


**Figure 3.15** Neutron reflectometry data for the different %MC3 containing lipid layers after incubation with different NAs. For the 5% MC3 layers in both pHs (a,b), only minor changes are observed after incubation with mRNA. For the 15% MC3 layers in both pHs (c,d) after incubation with mRNA, the formation of a broad peak can be observed at  $\approx 0.09 \text{ \AA}^{-1}$ , indicating the presence of a multilayer. For the 15% MC3 layer in pH 6 buffer after incubation with polyA (e), minor changes were observed, mostly in the H<sub>2</sub>O contrast, whereas after incubation with polyU (f), a subtle broad peak can be observed, mostly in the D<sub>2</sub>O contrast, similar to the ones in (c,d).

These changes can be discussed in terms of the (changes in) structure of

each RNA and the lipid layer. Case (i) is observed for the pure DOPC and 5% MC3 layers for all RNAs at all pHs, indicating that there is a threshold amount of MC3 required in the layer for significant adsorption of NA. This concept can be further extended to a required charge density in the layer, as there is a clear MC3 content and pH dependent trend in the adsorbed amount for the higher %MC3 layers (see Figure 3.13). As the pH range of these measurements covers the pKa of MC3, which is  $\approx 6.44$ , >50% of the MC3 is expected to be positively charged at the lowest pH studied here and the proportion of charged MC3 will decrease with increasing pH. The cited pKa is, however, the apparent pKa and the environment surrounding the protonation site can have a large effect on the pKa of the ionisable group<sup>35</sup>.

Case (ii) and (iii) appear to be linked instead to the structure of the RNA. As described in Section 1.3, polyA undergoes a structural transition from double to single stranded with increasing pH, which appears to correlate with the observed change from case (iii) to case (ii) in the QCM-D data. For polyU, on the other hand, only case (ii) is observed in the QCM-D data and it exists only in a single stranded form in the range of experimental conditions explored here. In the case of EPO mRNA, however, the structure is not clear, due to the higher sequence complexity and potential to form different secondary structures. It is likely, however, that there are parts of the strand with extensive base pairing and parts which are single stranded.

Case (iii) was observed for polyA in pH 6, where the double stranded structures start to dominate, and for mRNA in both pH 6 and 7. If the NA has a sufficiently ordered or bulky structure or if substantial base pairing occurs, the linear charge density of the strand would be higher. The main interaction would then be via the charged sugar phosphate backbone, meaning that the strand would likely sit at the outer surface of the lipid layer or penetrate into the head groups.

Case (ii) was observed in conditions where the RNAs are present in a single stranded form. This seems to indicate that the single strand allows this penetration into the lipid layer, possibly due its less bulky nature and/or by allowing accessing to the more hydrophobic bases thereby promoting hydrophobic interactions with the lipid acyl chains. This could cause the multilayer formation observed in the NR data for polyU. As the EPO mRNA most likely has both single stranded and base paired regions in its structure, a combination of these effects are probably present, with single stranded parts of the RNA penetrating into the lipid layer, causing rearrangement into a multilayer, and double stranded parts interacting mainly with the lipid head groups at the surface.

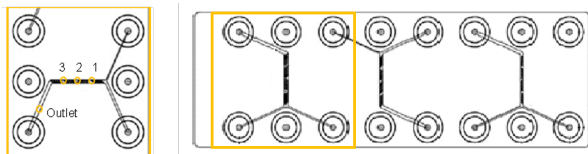


**Figure 3.16** A schematic illustration of the ChipShop (CS) Fluidic 187 Herringbone Mixer chip used for the microfluidic mixing (right), with the positions used for the SAXS measurements labelled (left).

### 3.2.2 Lipid nanoparticles

The formulation process for LNPs for nucleic acid delivery contains multiple steps, in which the LNP structure and composition evolves:

1. Microfluidic mixing of the lipid mixture in ethanol and the NA cargo in a low pH buffer
2. Removal of the remaining ethanol and change of the aqueous solution to phosphate buffered saline (PBS) with a physiological salt concentration. In an research setting, this has typically been achieved with dialysis, whereas in an industrial setting, alternative processes like tangential flow filtration have been employed.
3. Concentration of the dialysed formulation via centrifugation

As the LNP structure is strongly dependent on the lipid composition, a benchmark lipid composition containing MC3:cholesterol:DSPC:DMPE-PEG2000 in the molar ratio 50:38.5:10:1.5 was used for all LNP formulation. Two different cargo concentrations, which are conventionally described using the MC3 nitrogen to nucleotide phosphate ratio (N:P), of N:P 3 and 6 were characterised, where N:P 3 is a higher NA loading than N:P 6.

#### Microfluidics and dialysis

The structural evolution during microfluidic mixing for two formulations containing polyA N:P 3 and DNA N:P 3 was followed using *in situ* SAXS. SAXS data were collected at four different points of the microfluidic channel on the chip; three along the staggered herringbone structure in the main channel and one near the outlet, as shown in Figure 3.16.



For both DNA and polyA, the growth of a shoulder at lower  $q$ , which increases in intensity moving along the channel, most likely corresponds to the 'proto-LNPs' observed immediately after microfluidic mixing. These are a combination of NA-MC3 complexes and proto-LNPs composed of the helper lipids DSPC, DMPE-PEG2000 and cholesterol (with/without NA) according to work by Li et al.<sup>101</sup>, which appear as 'vesicle-like' structures with electron dense parts<sup>88</sup>.

For DNA, a peak at  $\approx 0.11 \text{ \AA}^{-1}$  at the outlet were observed (Figure 3.17(a,b)). As this peak appears at approximately the same position as the peak corresponding to the internal structure in SAXS data of the final formulation, it is likely closely related to the final core structure.

Further SAXS data were collected during the dialysis of LNP formulations with DNA, polyA and polyU N:P 3 in order to study the LNP structure during dialysis. For all of the SAXS data measured during dialysis, a peak at  $\approx 0.1 \text{ \AA}^{-1}$  is visible, which initially shifts to higher  $q$  during the first half of the dialysis period and then later to lower  $q$  (Figure 3.17(d,e,f)). Although the position of the peaks for DNA and polyA change during the dialysis, the peak shape remains consistent. For polyU, however, the peak changes from a sharp peak early in the dialysis, similar to the sharp peak in the polyA data, to a broad, low intensity peak at a later stage of dialysis.

As the trend in peak position during dialysis is mostly the same independent of cargo, it can be concluded that this is due to general changes occurring in the LNP structure. These are expected to include fusion of proto-LNPs with and without NA and NA-MC3 complexes and change in buffer conditions, resulting in changes in lipid composition and distribution throughout the LNP structure.

## Final formulation

For the final formulation step, we have investigated the structure of LNP formulations containing dsDNA, ssDNA, polyA and polyU with N:P 3 and 6. The structure of the final LNP formulation was characterised with a combination of scattering techniques (SANS, SAXS and DLS) and cryoTEM. It should be noted that two different herringbone microfluidic set ups were used to prepare the LNPs: the self-contained NanoAssemblr (Precision Nanosystems Inc., denoted 'NA') or an inhouse set up using a Fluidic 187 Herringbone Mixer chip (ChipShop, denoted 'CS') and dual syringe pump.

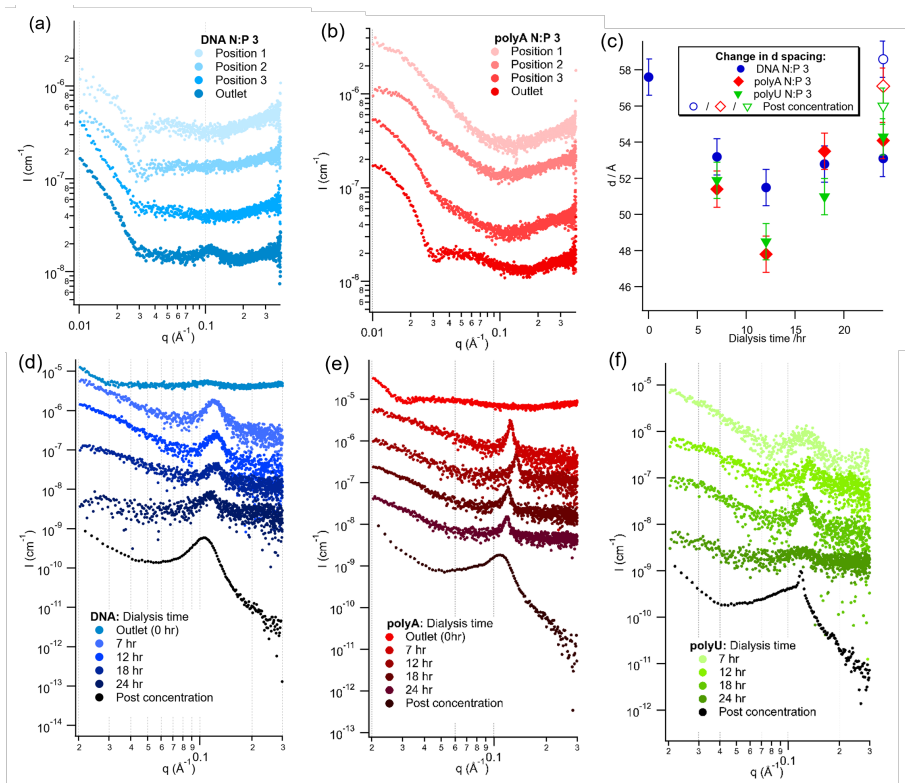


**Figure 3.17** SAXS measurements during the LNP formulation process demonstrate the evolution of the structure. SAXS data were measured during microfluidic mixing at 4 points along the microfluidic channel for LNPs containing DNA N:P 3 (a) and polyA N:P 3 (b). The evolution of the repeat distance during dialysis (c) was calculated from the peak positions in SAXS data for LNP formulations containing DNA (d), polyA (e) and polyU (f) N:P 3.

SANS measurements with contrast variation were utilised in order to investigate if the lipid composition of the shell and core changes with cargo and cargo concentration. Samples containing dsDNA and ssDNA with N:P 3 and 6 were prepared using deuteration scheme 0 (D0, see Table 3.3) and measured at a particle concentration of 1.75mg/mL, in order to minimise the influence of interparticle interactions on the scattering. In order to increase the contrast in the core, samples containing polyA and polyU N:P 3 and 6 and dsDNA and ssDNA N:P 3 were prepared using D1 (see Table 3.3) and measured at a higher LNP concentration of 4 mg/mL. To provide additional confirmation of the distribution of cholesterol and DSPC between the shell and core of the structure, two further deuteration schemes (D2 and D3, see Table 3.3) varying DSPC and cholesterol deuteration were prepared for dsDNA and ssDNA N:P 3 and measured at an

**Table 3.3** Lipid deuteration scheme used in SANS contrast variation study.

Deuteration scheme	MC3	Chol	DSPC	DMPE-PEG <sub>2000</sub>
<b>D0</b>	h	d7	d83	h
<b>D1</b>	h	d45	h	h
<b>D2</b>	h	d45	d83	h
<b>D3</b>	h	h	d83	h

LNP concentration of 4 mg/mL.

**Colloidal stability.** The size of the different LNP formulations was initially characterised by DLS. There were no clear trends in the initial size of the LNPs (Figure 3.18: Day 1) with cargo, however the LNPs with a higher N:P (i.e. lower amount of NA) were consistently smaller, which has been previously reported for mRNA LNPs with the same lipid composition<sup>88,101</sup>.

From DLS, the colloidal stability of the different formulations can also be discussed by considering the change in size of the LNPs over time. For the LNPs containing polyA, there was no size change within error over the measurement period, indicating that they were colloiddally stable (Figure 3.18). The LNPs with polyU aggregated almost immediately upon formulation (by day 3); multiple peaks were observed in the intensity distribution and a high polydispersity, therefore the size for these samples were not included in Figure 3.18.

For the dsDNA samples, both in Figure 3.18 and 3.19, no or a minor change in size was observed, showing that these particles were stable. For the ssDNA samples, however, the case is more complex. In Figure 3.18, there is no appreciable change in size at Day 16, however in Figure 3.19, the ssDNA samples show a significant increase in radius at Day 19, indicating particle aggregation. The samples prepared with deuteration scheme 0 were stored throughout the measurement period at 4 °C, whereas the samples prepared with deuteration schemes 1,2,3 were measured during a remote beamtime at ANSTO (Lucas Heights, Australia) and it is likely that the samples experienced temperature fluctuations during transit. As these LNPs are widely regarded to be only kinetically stable, their aggregation is kinetically controlled, therefore a higher temperature would increase both the rate and likelihood of aggregation. We attribute the discrepancy between the observed colloidal stabilities for the ssDNA samples to these temperature fluctuations and believe this underlines the stability of the dsDNA samples.

As the stability of the LNP formulations appeared to be linked to the base pairing of the NA, the extent of base pairing in the final LNP formulation

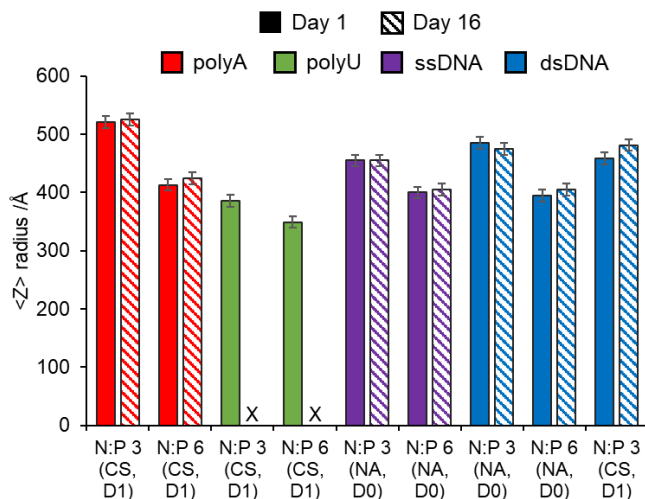


**Figure 3.18**  $\langle Z \rangle$  radius measured by DLS for LNP samples with different cargo and N:P.

was determined for the dsDNA and ssDNA N:P 3 samples (D1,2,3) immediately after formulation. The encapsulation efficiency of samples was measured using fluorescence based assays using two different dyes; Ribogreen, which binds to polymeric NAs, and Picogreen, which specifically binds to dsDNA. By comparing the encapsulation efficiencies determined for each dye, the extent of base pairing can be determined. For the dsDNA samples, the Ribogreen and Picogreen dyes gave almost identical results, indicating that the dsDNA remains fully base paired ( $96.2 \pm 0.6\%$ ) after the formulation process. For the ssDNA samples, however, the encapsulation efficiency measured with Picogreen was approximately half of the Ribogreen value, showing that the  $52 \pm 2\%$  of the ssDNA strands were base paired.

From these results, there appears to be a link between the colloidal stability of the LNPs and the extent of base pairing of the NA. Both LNPs containing polyA, which is expected to be double stranded at the initial formulation pH, and dsDNA, which was shown to be fully base paired in the final formulation, were the most colloiddally stable from the DLS results. LNPs formulated with ssDNA were observed to aggregate in the ssDNA N:P 3 D1,2,3 samples, however the aggregation was much less extensive than LNPs containing polyU, which underwent massive aggregation almost immediately after formulation. PolyU would be the extreme case here, as it is expected to be single stranded in all of the solution conditions used here, whereas ssDNA was observed to have  $\approx 50\%$  base paired strands after formulation.

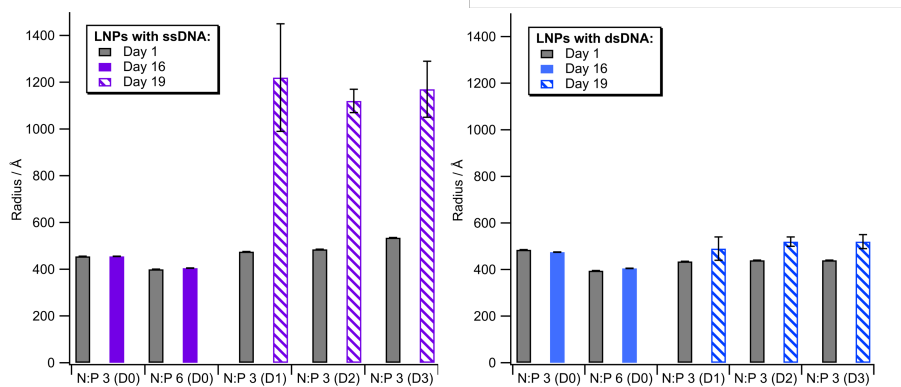


**Figure 3.19** Comparison between the radii for LNPs formulated with DNA and different deuteration schemes.

**Lipid composition.** In previous work describing SANS data for RNA LNPs with this lipid composition, the data was fit using a core shell sphere model, where the lipid composition of the shell and core is different, plus a broad peak at  $\approx 0.1 \text{ \AA}^{-1}$  corresponding to the internal structure of the LNP. As this core-shell structure was compatible with the cryoTEM images for these samples, the SANS data were fit with either a core shell sphere (CSS) model or a core shell sphere plus a generic broad peak (CSS+BP) model.

For the dsDNA and ssDNA N:P 3 and 6 samples with deuteration scheme D0 measured at  $[\text{LNP}] = 1.75 \text{ mg/mL}$ , the broad peak was not visible in SANS. This was most likely due to the lower particle concentration and lower deuteration in the core (i.e. using d7 cholesterol). These data were therefore fit with the CSS sphere model (Figure 3.20).

The remaining samples were measured at a higher  $[\text{LNP}]$  of  $4 \text{ mg/mL}$  and a broad peak was visible at  $\approx 0.1 \text{ \AA}^{-1}$ , therefore these data were fit with the combined CSS+BP model (Figure 3.21). These samples were initially fit using a CSS model over a limited  $q$  range. In a second step, the data were then fit with a combined CSS+BP model in which the structural parameters (core radius and shell thickness) were fixed from the CSS fit and the SLD of the core and shell were allowed to vary. Further details on the fitting process can be found in Papers V and VI.

Excluding the low  $q$  upturn observed in the aggregated ssDNA N:P 3 samples, the data were described well by their respective models, indicating that the core shell sphere structure was also relevant for LNPs with these

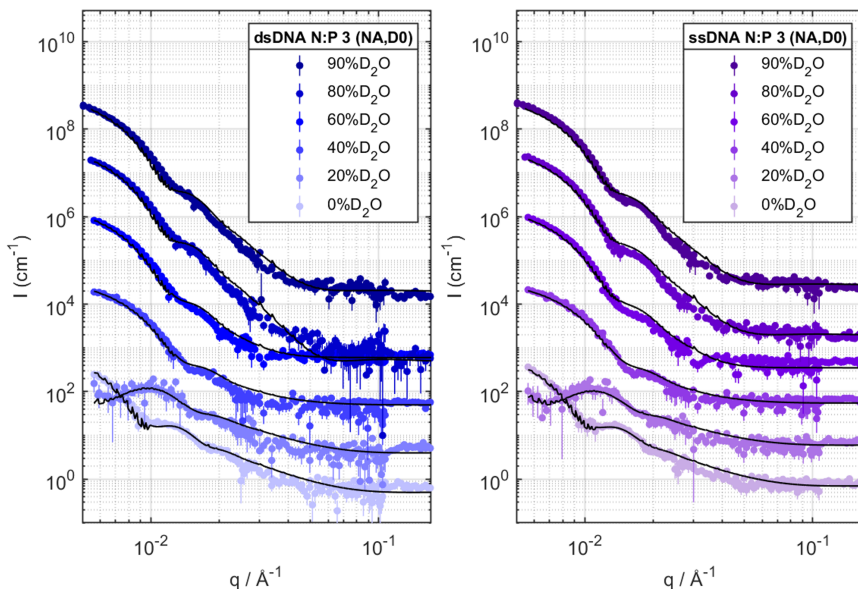


**Figure 3.20** Representative SANS data for dsDNA N:P 3 (left) and ssDNA N:P 3 (right) with deuteration scheme 0, measured at  $[LNP] = 1.75$  mg/mL and fit with a core shell sphere model (black line). The samples were measured in six different solvent contrasts: 0, 20, 40, 60, 80, 90%  $D_2O$  (plotted from bottom to top with 0% in the lightest colour and 90% in the darkest). The curves are offset for clarity.

cargoes. In general, the shell thickness of  $\approx 50$  Å agreed well with cryoTEM images (insets of Figure 3.22 and 3.23) and the total particle radius from the fit was systematically smaller than the measured hydrodynamic radius from DLS for the non-aggregated samples.

From qualitative evaluation of the fitted SLD values for the core and shell for the dsDNA and ssDNA N:P 3 samples with deuteration schemes 1,2 and 3, it was possible to confirm the conclusions from previous work that DSPC is fully present in the LNP shell and the cholesterol is split between the shell and core.

For all of the samples, it was possible to estimate the lipid composition of the core and the shell. For this calculation, it was assumed that 100% of the DSPC and the DMPE portion of DMPE-PEG2000 was present in the shell and 100% of the NA cargo was present in the core. The results across the different samples measured at the same  $[LNP]$  are remarkably consistent, especially considering the difference in solvent volume fraction between the DNA containing LNPs and the polyA and polyU containing

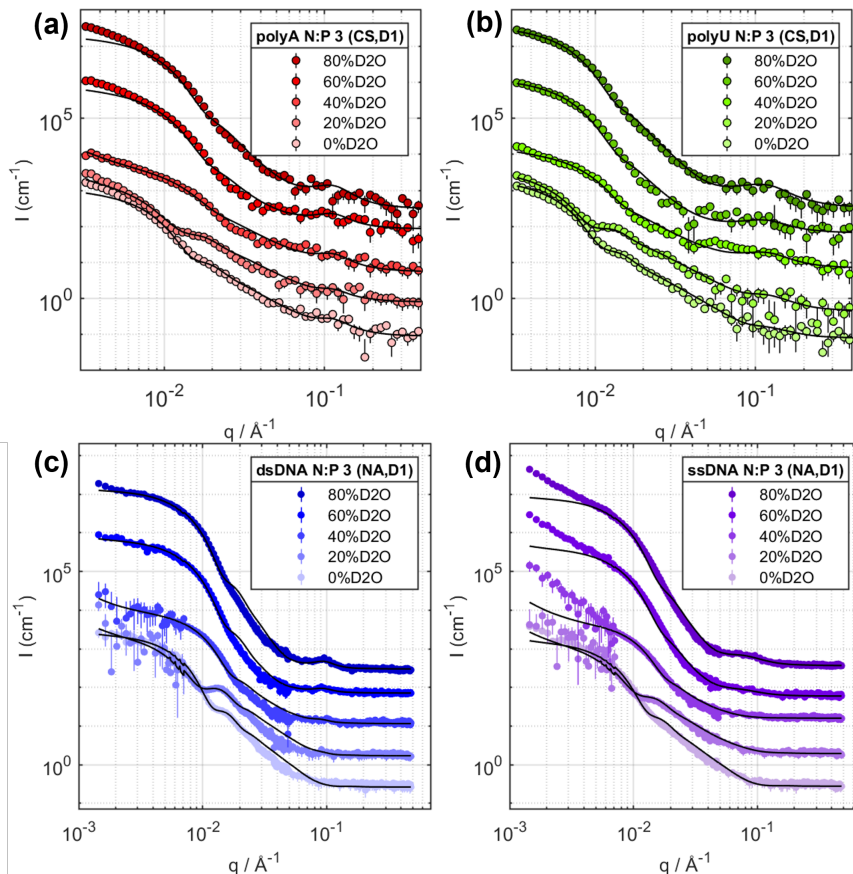


**Figure 3.21** Representative SANS data for (a) polyA, (b) polyU, (c) dsDNA and (d) ssDNA N:P 3 with deuteration scheme 1, measured at  $[LNP] = 4 \text{ mg/mL}$  and fit with a core shell sphere plus broad peak model (black line). The samples were measured in five different solvent contrasts: 0, 20, 40, 60, 80%  $D_2O$  (plotted from bottom to top with 0% in the lightest colour and 80% in the darkest). The curves are offset for clarity.

LNPs and that extensive aggregation had occurred in the polyU samples. For LNPs with dsDNA and ssDNA, there was no solvent present in the shell, as has been assumed in previous work with mRNA LNPs<sup>88,102</sup>. For polyA and polyU, however, the solvent fraction in the shell was  $\approx 0.4$ .

In general, for all LNPs the majority of the shell dry volume fraction was composed of cholesterol and DSPC, whereas the dry volume fraction of the core was dominated by MC3.

A general trend observed with N:P observed for all cargos, was that the shell compositions are very consistent for different cargos and N:P among

**Table 3.4** Table summarising the lipid molar fractions for the shell and core of the LNP samples measured at a lower [LNP] of 1.75 mg/mL, which were fit with the core-shell sphere model. DMPE refers to the part of the pegylated lipid, DMPE-PEG2000. \*The position of these components was fixed so that the DSPC and DMPE portion of the PEG lipid were present in the shell and the NA cargo was present in the core.

Model: CSS only	%mol in shell				%mol in core		
Sample	MC3	Chol	DSPC*	DMPE*	MC3	Chol	NA (nt)*
dsDNA N:P 3 (NA)	4±3	71±6	21.2	3.2	70±2	7±4	22.9
dsDNA N:P 6 (NA)	4±7	73±15	19.8	3.0	84±6	3±13	13.1
ssDNA N:P 3 (NA)	4±4	73±9	19.9	3.0	74±3	3±7	23.8
ssDNA N:P 6 (NA)	4±6	71±12	22.0	3.3	78±4	10±9	12.0

data fit with same model, whereas in the core, the molar ratio of MC3 increases with increasing N:P.

Among the higher [LNP] contrast variation series for dsDNA and ssDNA N:P 3, the composition was very consistent across the different deuteration schemes, indicating that small changes in total particle size do not largely affect the shell or core composition.

It should be noted that, although the trends remain the same for the LNPs with dsDNA and ssDNA measured at different [LNP], the calculated values of the lipid composition are different. This can be attributed to the the different models used to fit the SANS data. In the CSS+BP model used to fit the higher [LNP] data, there is a Porod scaling law term, which has a larger contribution at lower  $q$ . This contribution would result in a lower fitted SLD difference between the particle and solvent, therefore a higher volume fraction of solvent in the core, lower dry shell SLD and higher dry core SLD. This is demonstrated in Paper VI, where the fitted SLD and solvent fraction values from the CSS and CSS+BP models for the dsDNA and ssDNA N:P 3 samples measured at higher [LNP] are compared.

**Internal structure.** The internal structure and core morphology of the final formulation of the LNPs could be investigated in more detail using a combination of SAXS and cryoTEM. Typically when discussing the internal structure of LNPs, it is assumed that the LNP population is homogeneous. It has been shown by single particle fluorescence studies, however, that there is a significant proportion of empty LNPs in a typical formulation for RNA LNPs<sup>101,103</sup>. The average internal structure of empty LNPs (i.e. with no RNA in the formulation) and a formulation containing RNA was also shown to be different using SAXS, in which the peak observed in the empty LNP SAXS was both broader and shifted to lower  $q$ <sup>88</sup>.



**Table 3.5** Table summarising the lipid molar fractions for the shell and core of the LNP samples measured at a higher [LNP] of 4 mg/mL, which were fit with the core-shell sphere plus broad peak model. DMPE refers to the part of the pegylated lipid, DMPE-PEG2000. \*The position of these components was fixed so that the DSPC and DMPE portion of the PEG lipid were present in the shell and the NA cargo was present in the core. For the dsDNA and ssDNA N:P 3 (NA), the values presented here are the mean  $\pm$  standard deviation for the lipid molar fractions determined from the different deuteration schemes.

Model: CSS+BP	%mol in shell				%mol in core		
Sample	MC3	Chol	DSPC*	DMPE*	MC3	Chol	NA (nt)*
polyA N:P 3 (CS)	18 $\pm$ 2	60 $\pm$ 5	19.7	3.0	65 $\pm$ 2	13 $\pm$ 4	22.3
polyA N:P 6 (CS)	10 $\pm$ 4	67 $\pm$ 7	19.9	3.0	78 $\pm$ 4	8 $\pm$ 6	13.9
polyU N:P 3 (CS)	15 $\pm$ 3	63 $\pm$ 5	19.9	3.0	68 $\pm$ 2	11 $\pm$ 4	21.1
polyU N:P 6 (CS)	13 $\pm$ 5	64 $\pm$ 9	20.4	3.1	76 $\pm$ 4	13 $\pm$ 7	11.3
dsDNA N:P 3 (CS)	19 $\pm$ 3	59 $\pm$ 7	19.1	2.9	64 $\pm$ 3	12 $\pm$ 6	23.7
dsDNA N:P 3 (NA)	16 $\pm$ 3	63 $\pm$ 3	18.7 $\pm$ 0.4	2.8 $\pm$ 0.1	66 $\pm$ 3	7 $\pm$ 4	25.7 $\pm$ 0.6
ssDNA N:P 3 (NA)	21 $\pm$ 2	59 $\pm$ 1	16.8 $\pm$ 0.4	2.5 $\pm$ 0.1	67 $\pm$ 2	6 $\pm$ 2	27 $\pm$ 1

The internal structure peak observed in SAXS for the different LNP formulations is plotted in Figures 3.22 and 3.23. SAXS data for empty LNPs (kindly provided by Yanez Arteta et al. from ref.<sup>88</sup>) was fit with a broad peak model. The SAXS data for the NA LNPs presented here was therefore fit with a linear combination of the broad peak model describing the empty LNPs (with the structural parameters fixed from the original fit) and either 1 or 2 peaks corresponding to the internal structure of NA containing LNPs, shown in Figures 3.22 and 3.23.

For all the samples, the relative contribution to the scattering from the empty LNPs was observed to increase slightly with N:P, which is consistent with previous work<sup>101,103</sup>.

Both polyA samples and polyU N:P 6 samples could be described by the empty LNP broad peak plus a single Gaussian peak, whereas an additional Gaussian peak was required to describe the sharp Bragg peak at  $\approx 0.12 \text{ \AA}^{-1}$  in the polyU N:P 3 data (Figure 3.22). As this sharp Bragg peak is most likely associated with the second population of highly aggregated species in the polyU samples, it was disregarded for the discussion of the NA LNP internal structure. For both polyA and polyU, the main Gaussian peak has the same position and width for both N:P and only the scale of the single peak relative to the empty LNP contribution decreased with increasing N:P.

For the DNA samples, two Gaussian peaks were required in addition to the empty LNP peak contribution, in order to better describe the shoulder on the high  $q$  side of the peak (Figure 3.23). For all of the DNA samples, the data was well-described by a combination of a peak at the maximum

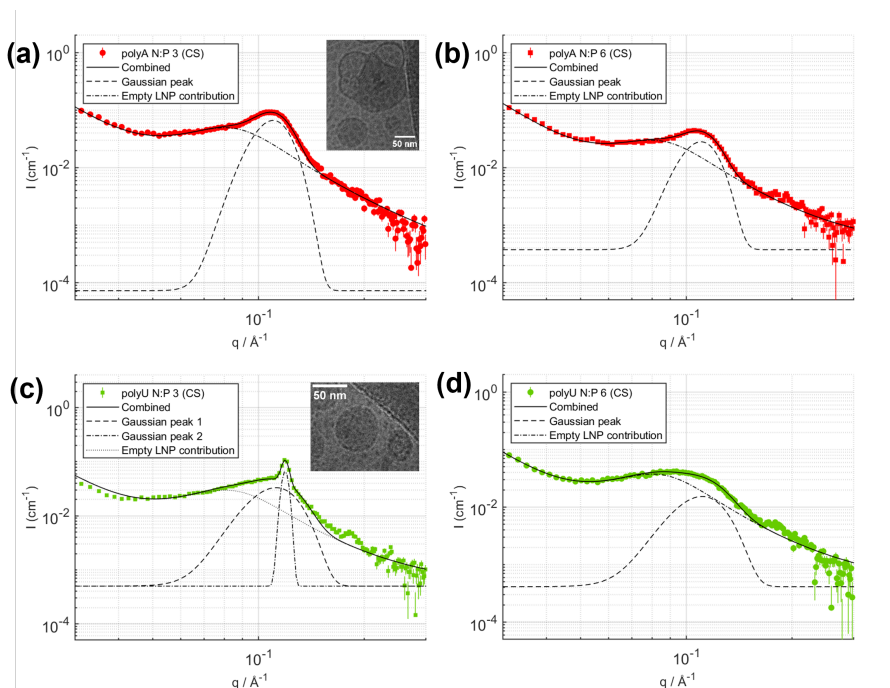


**Figure 3.22** Static SAXS data was fit for LNPs containing polyA N:P 3 (a) and 6 (b) and polyU N:P 3 (c) and 6 (d) using a broad peak model with either one or two Gaussian peaks.

intensity value and a second, broader peak at a similar or slightly higher  $q$  value. For the N:P 3 samples, the this second peak is  $\approx 0.004 \text{ \AA}^{-1}$ , whereas for the N:P 6 samples, the second peak was more than double the width.

This fitting of the DNA samples indicates that there are multiple populations of LNPs with different internal structures in the sample, including the empty LNPs and NA LNPs with different internal structures. As the difference between the DNA samples is observed with N:P, rather than cargo, it is possible that this is related to the number of DNA molecules present inside the LNP, as this has been shown to vary with N:P for RNA LNPs<sup>101,103</sup>.

For the polyA and polyU samples, however, only a single peak was required to describe the NA LNP population, indicating that the NA LNP population in these samples is more homogeneous. This could be due to the higher polydispersity of the polyA and polyU than DNA. It has previously been shown that LNPs have a maximum 'mass limit' rather than a maximum number of NA molecules that they can encapsulate. For the LNPs with DNA, which has a more well defined length, this would result in more dis-

tinct populations (e.g. with 1, 2, 3, etc DNA molecules per LNP) whereas the polyA and polyU samples could have a wider range of possible number of NA molecules with different masses.

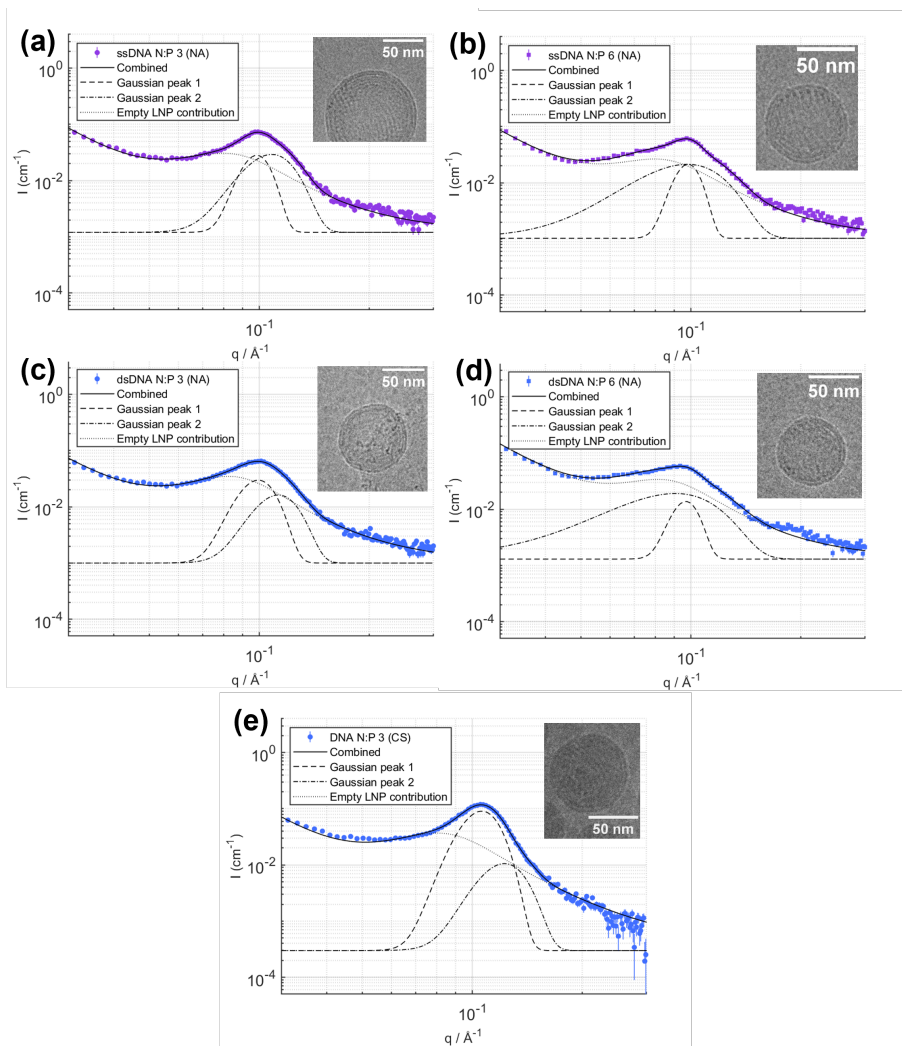


**Figure 3.23** Static SAXS data was fit for LNPs containing ssDNA N:P 3 (a) and 6 (b) and dsDNA N:P 3 (c) and 6 (d) prepared using the NanoAssemblr system and dsDNA N:P 3 (e) prepared using the ChipShop system using a broad peak model with two Gaussian peaks.



# 4

# Conclusions

In this thesis, the encapsulation of large biomolecules in two different lipid system was investigated.

The first part of this work focussed on the encapsulation of proteins with applications in the food industry in a lipid sponge phase composed of food safe ingredients.

It was shown that the enzyme  $\beta$ -galactosidase was successfully encapsulated in the sponge phase by SAXS and the diffusion limitations observed in activity tests. The thermal stability of  $\beta$ -galactosidase improved with encapsulation compared to free  $\beta$ -galactosidase stored at the same temperature and retained good activity and substrate affinity after encapsulation. Upon dispersion, L<sub>3</sub>NPs with high encapsulation efficiency and a well-defined size were obtained. The effect of encapsulation of  $\beta$ -galactosidase and aspartic protease on the membrane dynamics of L<sub>3</sub>NPs were investigated by NSE spectroscopy. It was shown that encapsulation of both enzymes reduced the dynamics over the full  $q$  range measured. A larger decrease was observed with increasing protein concentration and with  $\beta$ -galactosidase compared to aspartic protease.

In comparison, the encapsulation of myoglobin and BvPgb proved to be more complex. BvPgb did not strongly interact with the membrane and tended to aggregate when the bulk phase was dispersed, whereas myoglobin caused significant disruption to the sponge phase structure upon dispersion. This study also highlighted the importance of considering the effect of the buffer used to prepare the bulk phase and dispersing medium.

Systematic investigation of the effect of buffer and pH on the sponge phase structure in bulk and dispersions indicated the presence of specific buffer effects over the full pH range and a trend of increasing water channel size with increasing pH above pH 8.

The second part of this work studied the interactions of nucleic acids with a model system containing the cationic ionisable lipid MC3 and the effect of different nucleic acids on the structure of LNPs formulated with a benchmark lipid composition.

In the model system of a supported lipid layer containing MC3 and DOPC, the adsorbed amount of nucleic acid increased with increasing proportion of MC3 and decreasing pH (i.e. increasing positive charge density in the layer). The different adsorption behaviours and effect on the lipid layer structure observed in NR for EPO mRNA, polyA and polyU could be related to the structural changes expected for the different NAs with pH.

The structure of LNPs containing different nucleic acids and cargo loading was studied throughout the formulation process. SAXS measurements showed that the LNP structure continues to evolve during microfluidic mixing and the subsequent dialysis. The colloidal stability of the final LNP formulation appeared to be related to the expected extent of base pairing of the encapsulated NA following  $\text{dsDNA} \approx \text{polyA} > \text{ssDNA} \gg \text{polyU}$ . SANS data for all the formulations confirmed a core shell sphere structure for the LNPs with a remarkably similar lipid composition of the shell and core for the LNPs with different cargo at the same N:P. In general, the shell composition was dominated by DSPC and cholesterol and was similar for all samples, whereas the core was dominated by MC3. Fitting of the broad peak in the SAXS data corresponding to the internal structure, showed that multiple populations of LNPs with different internal structures coexist within the final formulation, including empty LNPs and NA containing LNPs.

This thesis has highlighted the importance of considering the full complexity present in self-assembled systems. When optimising the encapsulation of a biomolecule in a self-assembled lipid structure, it is vital to examine more subtle effects in the system including higher order biomolecule structure, specific interactions between the biomolecule and the lipids, and solutions conditions (i.e. specific buffer effects and pH).







# References

- [1] Christie, W. W. *High-Performance Liquid Chromatography and Lipids: A Practical Guide*; Pergamon Press, 1987.
- [2] Israelachvili, J. N.; Mitchell, D. J.; Ninham, B. W. Theory of self-assembly of hydrocarbon amphiphiles into micelles and bilayers. *J. Chem. Soc., Faraday Trans. 2* **1976**, *72*, 1525–1568.
- [3] Mitchell, D. J.; Ninham, B. W. Micelles, vesicles and microemulsions. *J. Chem. Soc., Faraday Trans. 2* **1981**, *77*, 601–629.
- [4] Israelachvili, J. N. In *Intermolecular and Surface Forces (Third Edition)*, third edition ed.; Israelachvili, J. N., Ed.; Academic Press: San Diego, 2011; pp 535–576.
- [5] Seddon, J. M.; Templer, R. H. *Polymorphism of lipid-water systems*; 1995; Vol. 1; pp 97–160.
- [6] Evans, D. F.; Wennerström, H. *The Colloidal Domain: Where Physics, Chemistry, Biology, and Technology Meet*, 2nd ed.; Wiley-VCH, 1999; pp 375–376.
- [7] Shah, J. C.; Sadhale, Y.; Chilukuri, D. M. Cubic phase gels as drug delivery systems. *Advanced Drug Delivery Reviews* **2001**, *47*, 229–250.
- [8] Hyde, S. T.; Schröder, G. E. Novel surfactant mesostructural topologies: between lamellae and columnar (hexagonal) forms. *Current Opinion in Colloid & Interface Science* **2003**, *8*, 5–14.
- [9] Valdeperas, M.; Wiśniewska, M.; Ram-On, M.; Kesselman, E.; Danino, D.; Nylander, T.; Barauskas, J. Sponge Phases and Nanoparticle Dispersions in Aqueous Mixtures of Mono- and Diglycerides. *Langmuir* **2016**, *32*, 8650–8659, doi: 10.1021/acs.langmuir.6b01356.
- [10] Fornasier, M.; Murgia, S. Non-lamellar lipid liquid crystalline nanoparticles: A smart platform for nanomedicine applications. *Frontiers in Soft Matter* **2023**, *3*.
- [11] Bouvraï, H. In *Chapter one - Bending Rigidities of Lipid Bilayers: Their Determination and Main Inputs in Biophysical Studies*; Iglič, A. B. T., Ed.; Academic Press, 2012; Vol. 15; pp 1–75.

- [12] Brannigan, G.; Brown, F. L. H. A consistent model for thermal fluctuations and protein-induced deformations in lipid bilayers. *Biophysical journal* **2006**, *90*, 1501–1520.
- [13] Kučerka, N.; Nieh, M.-P.; Katsaras, J. Fluid phase lipid areas and bilayer thicknesses of commonly used phosphatidylcholines as a function of temperature. *Biochimica et Biophysica Acta (BBA) - Biomembranes* **2011**, *1808*, 2761–2771.
- [14] Pasenkiewicz-Gierula, M.; Takaoka, Y.; Miyagawa, H.; Kitamura, K.; Kusumi, A. Hydrogen Bonding of Water to Phosphatidylcholine in the Membrane As Studied by a Molecular Dynamics Simulation: Location, Geometry, and Lipid-Lipid Bridging via Hydrogen-Bonded Water. *The Journal of Physical Chemistry A* **1997**, *101*, 3677–3691, doi: 10.1021/jp962099v.
- [15] Yamamoto, E.; Akimoto, T.; Yasui, M.; Yasuoka, K. Origin of subdiffusion of water molecules on cell membrane surfaces. *Scientific Reports* **2014**, *4*, 4720.
- [16] Kulkarni, C. V.; Wachter, W.; Iglesias-Salto, G.; Engelskirchen, S.; Ahualli, S. Monoolein: a magic lipid? *Physical Chemistry Chemical Physics* **2011**, *13*, 3004–3021.
- [17] Hyde, S.; Andersson, S.; Ericsson, B.; Larsson, K. A cubic structure consisting of a lipid bilayer forming an infinite periodic minimum surface of the gyroid type in the glycerolmonooleat-water system. *Zeitschrift für Kristallographie - New Crystal Structures* **1984**, *168*, 213 – 219, Cited by: 453.
- [18] Jason Briggs;; Hesson Chung;; Martin Caffrey, The Temperature-Composition Phase Diagram and Mesophase Structure Characterization of the Monoolein/Water System. *J. Phys. II France* **1996**, *6*, 723–751.
- [19] Qiu, H.; Caffrey, M. The phase diagram of the monoolein/water system: metastability and equilibrium aspects. *Biomaterials* **2000**, *21*, 223–234.
- [20] Pitzalis, P.; Monduzzi, M.; Krog, N.; Larsson, H.; Ljusberg-Wahren, H.; Nylander, T. Characterization of the Liquid-Crystalline Phases in the Glycerol Monooleate/Diglycerol Monooleate/Water System. *Langmuir* **2000**, *16*, 6358–6365.
- [21] Barauskas, J.; Misiunas, A.; Gunnarsson, T.; Tiberg, F.; Johnsson, M. “Sponge” Nanoparticle Dispersions in Aqueous Mixtures of Diglycerol Monooleate, Glycerol Dioleate, and Polysorbate 80. *Langmuir* **2006**, *22*, 6328–6334, doi: 10.1021/la060295f.
- [22] Valldeperas, M.; Dabkowska, A. P.; Pálsson, G. K.; Rogers, S.; Mahmoudi, N.; Carnerup, A.; Barauskas, J.; Nylander, T. Interfacial properties of lipid sponge-like nanoparticles and the role of stabilizer on particle structure and surface interactions. *Soft Matter* **2019**, *15*, 2178–2189.
- [23] Badell, M. V. Lipid sponge phase nanostructures as carriers for enzymes. 2019.
- [24] Valldeperas, M.; Talaikis, M.; Dhayal, S. K.; Velička, M.; Barauskas, J.; Nisaura, G.; Nylander, T. Encapsulation of Aspartic Protease in Nonlamellar Lipid Liquid Crystalline Phases. *Biophysical Journal* **2019**, *117*, 829–843, doi: 10.1016/j.bpj.2019.07.031.

- [25] Gilbert, J.; Valldeperas, M.; Dhayal, S. K.; Barauskas, J.; Dicko, C.; Nylander, T. Immobilisation of  $\beta$ -galactosidase within a lipid sponge phase: structure, stability and kinetics characterisation. *Nanoscale* **2019**, *11*, 21291–21301.
- [26] Baden, L. R. et al. Efficacy and Safety of the mRNA-1273 SARS-CoV-2 Vaccine. *New England Journal of Medicine* **2021**, *384*, 403–416, PMID: 33378609.
- [27] Polack, F. P. et al. Safety and Efficacy of the BNT162b2 mRNA Covid-19 Vaccine. *New England Journal of Medicine* **2020**, *383*, 2603–2615, PMID: 33301246.
- [28] Semple, S. C.; Klimuk, S. K.; Harasym, T. O.; Dos Santos, N.; Ansell, S. M.; Wong, K. F.; Maurer, N.; Stark, H.; Cullis, P. R.; Hope, M. J.; Scherrer, P. Efficient encapsulation of antisense oligonucleotides in lipid vesicles using ionizable aminolipids: formation of novel small multilamellar vesicle structures. *Biochimica et Biophysica Acta (BBA) - Biomembranes* **2001**, *1510*, 152–166.
- [29] Aldosari, B. N.; Alfagih, I. M.; Almurshedi, A. S. Lipid Nanoparticles as Delivery Systems for RNA-Based Vaccines. *Pharmaceutics* **2021**, *13*, 206.
- [30] Samaridou, E.; Heyes, J.; Lutwyche, P. Lipid nanoparticles for nucleic acid delivery: Current perspectives. *Advanced Drug Delivery Reviews* **2020**, *154–155*, 37–63.
- [31] Hou, X.; Zaks, T.; Langer, R.; Dong, Y. Lipid nanoparticles for mRNA delivery. *Nature Reviews Materials* **2021**, *6*, 1078–1094.
- [32] Hajj, K. A.; Whitehead, K. A. Tools for translation: non-viral materials for therapeutic mRNA delivery. *Nature Reviews Materials* **2017**, *2*, 17056.
- [33] Semple, S. C. et al. Rational design of cationic lipids for siRNA delivery. *Nature Biotechnology* **2010**, *28*, 172–176.
- [34] Jayaraman, M. et al. Maximizing the potency of siRNA lipid nanoparticles for hepatic gene silencing in vivo. *Angewandte Chemie (International ed. in English)* **2012**, *51*, 8529–8533.
- [35] Carrasco, M. J.; Alishetty, S.; Alameh, M.-G.; Said, H.; Wright, L.; Paige, M.; Soliman, O.; Weissman, D.; Cleveland, T. E.; Grishaev, A.; Buschmann, M. D. Ionization and structural properties of mRNA lipid nanoparticles influence expression in intramuscular and intravascular administration. *Communications Biology* **2021**, *4*, 956.
- [36] Heyes, J.; Palmer, L.; Bremner, K.; MacLachlan, I. Cationic lipid saturation influences intracellular delivery of encapsulated nucleic acids. *Journal of Controlled Release* **2005**, *107*, 276–287.
- [37] Yu, H.; Angelova, A.; Angelov, B.; Dyett, B.; Matthews, L.; Zhang, Y.; Mohamad, M. E.; Cai, X.; Valimehr, S.; Drummond, C. J.; Zhai, J. Real-Time pH-Dependent Self-Assembly of Ionisable Lipids from COVID-19 Vaccines and In Situ Nucleic Acid Complexation. *Angewandte Chemie International Edition* **2023**,
- [38] Petkov, G. V. In *Pharmacology*; Hacker, M., Messer, W., Bachmann, K., Eds.; Academic Press: San Diego, 2009; pp 387–427.

- [39] Suki, B. In *Structure and Function of the Extracellular Matrix*; Suki, B., Ed.; Academic Press, 2022; pp 29–54.
- [40] Salah, R. B.; Mosbah, H.; Fendri, A.; Gargouri, A.; Gargouri, Y.; Mejdoub, H. Biochemical and molecular characterization of a lipase produced by *Rhizopus oryzae*. *FEMS Microbiology Letters* **2006**, *260*, 241–248.
- [41] Berg, J. M. J. M.; Tymoczko, J. L.; Gatto, G. J.; Stryer, L. *Biochemistry*, 8th ed.; W. H. Freeman and Company, 2015.
- [42] Sehnal, D.; Bittrich, S.; Deshpande, M.; Svobodová, R.; Berka, K.; Bazgier, V.; Velankar, S.; Burley, S. K.; Koča, J.; Rose, A. S. Mol\* Viewer: modern web app for 3D visualization and analysis of large biomolecular structures. *Nucleic Acids Research* **2021**, *49*, W431–W437.
- [43] Ángel Pereira-Rodríguez,; Fernández-Leiro, R.; González-Siso, M. I.; Cerdán, M. E.; Becerra, M.; Sanz-Aparicio, J. Structural basis of specificity in tetrameric *Kluyveromyces lactis*  $\beta$ -galactosidase. *Journal of Structural Biology* **2012**, *177*, 392–401.
- [44] Oliveira, C.; Guimarães, P. M. R.; Domingues, L. Recombinant microbial systems for improved  $\beta$ -galactosidase production and biotechnological applications. *Biotechnology Advances* **2011**, *29*, 600–609.
- [45] Becerra, M.; Cerdán, E.; Siso, M. I. G. Dealing with different methods for *Kluyveromyces lactis*  $\beta$ -galactosidase purification. *Biological Procedures Online* **1998**, *1*, 48–58.
- [46] A/S, C. H. H. HA-LACTASE™. <https://www.chr-hansen.com/en/food-cultures-and-enzymes/fresh-dairy/cards/product-cards/ha-lactase> [Accessed: 14th August 2023].
- [47] Russo, S. F.; Moothart, L. Kinetic study of the enzyme lactase. *Journal of Chemical Education* **1986**, *63*, 242.
- [48] Fox, P. *Cheese: Chemistry, Physics and Microbiology: Volume 1 General Aspects*; Springer US, 2012.
- [49] Poldermans, B. *Industrial Enzymology*, 2nd edn, Tony Godfrey, Stuart West (Eds.). Macmillan (1996), xiv + 609, ISBN: 0 333 59464 9. *Trends in Food Science and Technology* **1997**, *8*.
- [50] Erskine, P. T.; Coates, L.; Mall, S.; Gill, R. S.; Wood, S. P.; Myles, D. A. A.; Cooper, J. B. Atomic resolution analysis of the catalytic site of an aspartic proteinase and an unexpected mode of binding by short peptides. *Protein Science* **2003**, *12*, 1741–1749, doi: 10.1110/ps.0305203.
- [51] A/S, C. H. H. THERMOLASE®. <https://www.chr-hansen.com/en/food-cultures-and-enzymes/cheese/cards/product-cards/thermolase> [Accessed: 14th August 2023].
- [52] Hoy, J. A.; Hargrove, M. S. The structure and function of plant hemoglobins. *Plant Physiology and Biochemistry* **2008**, *46*, 371–379.

- [53] Höök, F.; Kasemo, B. The QCM-D Technique for Probing Biomacromolecular Recognition Reactions. 2007; [https://doi.org/10.1007/978-3-540-36568-6\\_12](https://doi.org/10.1007/978-3-540-36568-6_12).
- [54] Riquelme, A.; Hinrichsen, P. Non-symbiotic hemoglobin and its relation with hypoxic stress. *Chilean journal of agricultural research* **2015**, *75*, 80 – 89.
- [55] Christensen, S.; Groth, L.; Leiva-Eriksson, N.; Nyblom, M.; Bülow, L. Oxidative Implications of Substituting a Conserved Cysteine Residue in Sugar Beet Phyto-globin BvPgb 1.2. *Antioxidants* **2022**, *11*.
- [56] Scott, T.; Eagleson, M. *Concise Encyclopedia Biochemistry*; Walter de Gruyter, 1988.
- [57] Darbre, P. D.; Romero-Herrera, A.; Lehmann, H. Comparison of the myoglobin of the zebra (*Equus burchelli*) with that of the horse (*Equus caballus*). *Biochimica et Biophysica Acta (BBA) - Protein Structure* **1975**, *393*, 201–204.
- [58] Gilbert, J.; Christensen, S.; Nylander, T.; Bülow, L. Encapsulation of sugar beet phyto-globin BvPgb 1.2 and myoglobin in a lipid sponge phase system. *Frontiers in Soft Matter* **2023**, *3*.
- [59] Radola, B. J. Isoelectric focusing in layers of granulated gels: I. Thin-layer isoelectric focusing of proteins. *Biochimica et Biophysica Acta (BBA) - Protein Structure* **1973**, *295*, 412–428.
- [60] Egli, M.; Flavell, A.; Pyle, A. M.; Wilson, W. D.; Haq, S. I.; Luisi, B.; Fisher, J.; Laughton, C.; Allen, S.; Engels, J.; Blackburn, G. M.; Gait, M. J.; Loakes, D.; Williams, D. M. *Nucleic Acids in Chemistry and Biology*; The Royal Society of Chemistry, 2006; pp i–470.
- [61] Bevilacqua, P. C.; Ritchey, L. E.; Su, Z.; Assmann, S. M. Genome-Wide Analysis of RNA Secondary Structure. *Annual Review of Genetics* **2016**, *50*, 235–266, doi: 10.1146/annurev-genet-120215-035034.
- [62] Wang, T.; Sha, R.; Birktoft, J.; Zheng, J.; Mao, C.; Seeman, N. C. A DNA Crystal Designed to Contain Two Molecules per Asymmetric Unit. *Journal of the American Chemical Society* **2010**, *132*, 15471–15473, doi: 10.1021/ja104833t.
- [63] Karikó, K.; Muramatsu, H.; Keller, J. M.; Weissman, D. Increased Erythropoiesis in Mice Injected With Submicrogram Quantities of Pseudouridine-containing mRNA Encoding Erythropoietin. *Molecular Therapy* **2012**, *20*, 948–953.
- [64] TriLink Biotechnologies, *Product Insert: CleanCap™ Erythropoietin mRNA*, [Online], [https://www.trilinkbiotech.com/media/folio3/productattachments/product\\_insert/L7209\\_Insert.pdf](https://www.trilinkbiotech.com/media/folio3/productattachments/product_insert/L7209_Insert.pdf).
- [65] Cui, L.; Pereira, S.; Sonzini, S.; van Pelt, S.; Romanelli, S. M.; Liang, L.; Ulkoski, D.; Krishnamurthy, V. R.; Brannigan, E.; Brankin, C.; Desai, A. S. Development of a high-throughput platform for screening lipid nanoparticles for mRNA delivery. *Nanoscale* **2022**, *14*, 1480–1491.
- [66] Wang, W.; Feng, S.; Ye, Z.; Gao, H.; Lin, J.; Ouyang, D. Prediction of lipid nanoparticles for mRNA vaccines by the machine learning algorithm. *Acta Pharmaceutica Sinica B* **2022**, *12*, 2950–2962.

- [67] Zarudnaya, M. I.; Kolomiets, I. M.; Potyahaylo, A. L.; Hovorun, D. M. Structural transitions in poly(A), poly(C), poly(U), and poly(G) and their possible biological roles. *Journal of Biomolecular Structure and Dynamics* **2019**, *37*, 2837–2866, doi: 10.1080/07391102.2018.1503972.
- [68] Zarudnaya, M. Study of conformational transitions in poly (A) by the buffer capacity technique. *Molecular Biology* **1998**, *32*, 417–422.
- [69] Zarudnaya, M.; Zheltovskii, N. Electrophoretic analysis of conformational transitions in poly (A) at acidic pH. *Molecular Biology* **1995**, *29*, 611–615.
- [70] Thrierr, J.; Dourlent, M.; Leng, M. A study of polyuridylic acid. *Journal of Molecular Biology* **1971**, *58*, 815–830.
- [71] Sigma Aldrich, *Product Infomation: Polyuridylic acid potassium salt*, [Online], <https://www.sigmaaldrich.com/deepweb/assets/sigmaaldrich/product/documents/181/457/p9528pis.pdf>.
- [72] Lindner, P.; Zemb, T. *Neutrons, X-rays and light : scattering methods applied to soft condensed matter*; 2002.
- [73] Luzzati, V.; Vargas, R.; Mariani, P.; Gulik, A.; Delacroix, H. Cubic Phases of Lipid-containing Systems: Elements of a Theory and Biological Connotations. *Journal of Molecular Biology* **1993**, *229*, 540–551.
- [74] Kumarage, T.; Nguyen, J.; Ashkar, R. Neutron Spin Echo Spectroscopy as a Unique Probe for Lipid Membrane Dynamics and Membrane-Protein Interactions. *JoVE* **2021**, e62396.
- [75] Stetefeld, J.; McKenna, S. A.; Patel, T. R. Dynamic light scattering: a practical guide and applications in biomedical sciences. *Biophysical Reviews* **2016**, *8*, 409–427.
- [76] Koppel, D. E. Analysis of Macromolecular Polydispersity in Intensity Correlation Spectroscopy: The Method of Cumulants. *The Journal of Chemical Physics* **2003**, *57*, 4814–4820.
- [77] Provencher, S. W. CONTIN: A general purpose constrained regularization program for inverting noisy linear algebraic and integral equations. *Computer Physics Communications* **1982**, *27*, 229–242.
- [78] Provencher, S. W.; Štěpánek, P. Global Analysis of Dynamic Light Scattering Autocorrelation Functions. *Particle & Particle Systems Characterization* **1996**, *13*, 291–294.
- [79] Nylander, T.; Campbell, R. A.; Vandoolaeghe, P.; Cárdenas, M.; Linse, P.; Rennie, A. R. Neutron reflectometry to investigate the delivery of lipids and DNA to interfaces (Review). *Biointerphases* **2008**, *3*, FB64–FB82.
- [80] Fragneto, G.; Lu, J. R.; McDermott, D. C.; Thomas, R. K.; Rennie, A. R.; Gallagher, P. D.; Satija, S. K. Structure of Monolayers of Tetraethylene Glycol Monododecyl Ether Adsorbed on Self-Assembled Monolayers on Silicon: A Neutron Reflectivity Study. *Langmuir* **1996**, *12*, 477–486, doi: 10.1021/la950289b.

- [81] Krueger, S.; Ankner, J. F.; Satija, S. K.; Majkrzak, C. F.; Gurley, D.; Colombini, M. Extending the Angular Range of Neutron Reflectivity Measurements from Planar Lipid Bilayers: Application to a Model Biological Membrane. *Langmuir* **1995**, *11*, 3218–3222, doi: 10.1021/la00008a055.
- [82] Abelès, F. Recherches sur la propagation des ondes électromagnétiques sinusoïdales dans les milieux stratifiés. *Ann. Phys.* **1950**, *12*, 596–640.
- [83] Sauerbrey, G. Verwendung von Schwingquarzen zur Wägung dünner Schichten und zur Mikrowägung. *Zeitschrift für Physik* **1959**, *155*, 206–222.
- [84] Danino, D. Cryo-TEM of soft molecular assemblies. *Current Opinion in Colloid & Interface Science* **2012**, *17*, 316–329.
- [85] Milne, J. L. S.; Borgnia, M. J.; Bartesaghi, A.; Tran, E. E. H.; Earl, L. A.; Schauder, D. M.; Lengyel, J.; Pierson, J.; Patwardhan, A.; Subramaniam, S. Cryo-electron microscopy – a primer for the non-microscopist. *The FEBS Journal* **2013**, *280*, 28–45.
- [86] Saibil, H. R. Macromolecular structure determination by cryo-electron microscopy. *Acta Crystallographica Section D* **2000**, *56*, 1215–1222.
- [87] Mayerhöfer, T. G.; Pahlow, S.; Popp, J. The Bouguer-Beer-Lambert Law: Shining Light on the Obscure. *ChemPhysChem* **2020**, *21*, 2029–2046.
- [88] Arteta, M. Y.; Kjellman, T.; Bartesaghi, S.; Wallin, S.; Wu, X.; Kvist, A. J.; Dabkowska, A.; Székely, N.; Radulescu, A.; Bergenholtz, J.; Lindfors, L. Successful reprogramming of cellular protein production through mRNA delivered by functionalized lipid nanoparticles. *Proceedings of the National Academy of Sciences* **2018**, *115*, E3351–E3360.
- [89] Jones, L. J.; Yue, S. T.; Cheung, C.-Y.; Singer, V. L. RNA Quantitation by Fluorescence-Based Solution Assay: RiboGreen Reagent Characterization. *Analytical Biochemistry* **1998**, *265*, 368–374.
- [90] Singer, V. L.; Jones, L. J.; Yue, S. T.; Haugland, R. P. Characterization of PicoGreen Reagent and Development of a Fluorescence-Based Solution Assay for Double-Stranded DNA Quantitation. *Analytical Biochemistry* **1997**, *249*, 228–238.
- [91] Johnson, K. A.; Goody, R. S. The Original Michaelis Constant: Translation of the 1913 Michaelis–Menten Paper. *Biochemistry* **2011**, *50*, 8264–8269, doi: 10.1021/bi201284u.
- [92] Shih, L.; Chung, Y.; Sriram, R.; Jue, T. Interaction of myoglobin with oleic acid. *Chemistry and Physics of Lipids* **2015**, *191*, 115–122.
- [93] Sriram, R.; Kreutzer, U.; Shih, L.; Jue, T. Interaction of fatty acid with myoglobin. *FEBS Letters* **2008**, *582*, 3643–3649.
- [94] Cistola, D. P.; Hamilton, J. A.; Jackson, D.; Small, D. M. Ionization and phase behavior of fatty acids in water: application of the Gibbs phase rule. *Biochemistry* **1988**, *27*, 1881–1888.



- [95] Mele, S.; Söderman, O.; Ljusberg-Wahrén, H.; Thuresson, K.; Monduzzi, M.; Nylander, T. Phase behavior in the biologically important oleic acid/sodium oleate/water system. *Chemistry and Physics of Lipids* **2018**, *211*, 30–36.
- [96] Salentinig, S.; Sagalowicz, L.; Glatter, O. Self-Assembled Structures and pKa Value of Oleic Acid in Systems of Biological Relevance. *Langmuir* **2010**, *26*, 11670–11679, doi: 10.1021/la101012a.
- [97] Lasting impact of lipid nanoparticles. *Nature Reviews Materials* **2021**, *6*, 1071.
- [98] Tiberg, F.; Harwigsson, I.; Malmsten, M. Formation of model lipid bilayers at the silica-water interface by co-adsorption with non-ionic dodecyl maltoside surfactant. *European Biophysics Journal* **2000**, *29*, 196–203.
- [99] Gilbert, J.; Ermilova, I.; Fornasier, M.; Skoda, M.; Fragneto, G.; Swenson, J.; Nylander, T. On the interactions between RNA and titrateable lipid layers: Implications for RNA delivery with lipid nanoparticles. *ChemRxiv* **2023**,
- [100] Ibrahim, M.; Gilbert, J.; Heinz, M.; Nylander, T.; Schwierz, N. Structural insights on ionizable Dlin-MC3-DMA lipids in DOPC layers by combining accurate atomistic force fields, molecular dynamics simulations and neutron reflectivity. *Nano-scale* **2023**, *15*, 11647–11656.
- [101] Li, S.; Hu, Y.; Li, A.; Lin, J.; Hsieh, K.; Schneiderman, Z.; Zhang, P.; Zhu, Y.; Qiu, C.; Kokkoli, E.; Wang, T.-H.; Mao, H.-Q. Payload distribution and capacity of mRNA lipid nanoparticles. *Nature Communications* **2022**, *13*, 5561.
- [102] Sebastiani, F. et al. Apolipoprotein E Binding Drives Structural and Compositional Rearrangement of mRNA-Containing Lipid Nanoparticles. *ACS Nano* **2021**, *15*, 6709–6722, doi: 10.1021/acsnano.0c10064.
- [103] Sych, T.; Schlegel, J.; Barriga, H. M. G.; Ojansivu, M.; Hanke, L.; Weber, F.; Bostancioglu, R. B.; Ezzat, K.; Stangl, H.; Plochberger, B.; Laurencikienė, J.; Andaloussi, S. E.; Fürth, D.; Stevens, M. M.; Sezgin, E. High-throughput measurement of the content and properties of nano-sized bioparticles with single-particle profiler. *Nature Biotechnology* **2023**,



